Hot Gas and Magnetic Fields in Clusters of Galaxies

Peter C. Tribble

St. John's College
and
Department of Theoretical Physics
Oxford

A thesis submitted to the University of Oxford in partial fulfilment of the requirements for the degree of Doctor of Philosophy.

August 1989

Abstract

Many clusters of galaxies contain large quantities of hot diffuse gas. I have studied the properties of waves in this gas using Lagrangian perturbations. The gas is far more thermally stable than is commonly thought. For bremsstrahlung cooling, all modes that remain oscillatory are damped. Galaxy motions, especially the oscillations of a central cD galaxy, are an important way of generating large amplitude waves in cluster gas. This is especially pertinent in view of the growing realization that cD galaxies are not at rest with respect to the cluster.

I also present evidence that weak magnetic fields tangled on scales of $\sim 10\,\mathrm{kpc}$ are common in cluster gas. Electrons responsible for the flow of heat in the gas must travel along the field lines, leading to a global reduction in heat flux. The superposition of many different field lines implies that the cluster gas is a multiphase medium. Such a picture has been suggested independently by the claimed observation of mass drop-out from cooling flows. I also show some results from a more advanced study using real magnetic fields rather than random walk models.

Acknowledgments

First of all I should thank my thesis supervisor, James Binney, for suggesting the subject matter of this thesis as worthy of investigation, and for allowing me considerable (some would say unwarranted) freedom to carry on research in my own way.

I owe a debt of gratitude to my wife Melanie who supported me through my study here.

My time as a graduate student has been enriched by the friendship of members of this department and of the department of Astrophysics. Of particular note are Colin McGill, for putting up with me as an office partner, and Susan Vassar, for conversation. To everybody else—Graham, Benjamin, Prasenjit, Adrian, Francine, Miriam and Shaun—a big thankyou.

Contents

Chapter 1. Introduction

It has long been apparent that matter is not distributed uniformly in the universe. Looking up at the sky one can see that stars are concentrated toward the Milky Way. This tendency for non-uniformity holds true on larger scales also. Stars huddle together in galaxies, galaxies are grouped into clusters, and the distribution of clusters of galaxies is not uniform. But clusters do not simply contain galaxies of stars—it is clear that the intervening space contains a large amount of hot gas threaded by weak tangled magnetic fields, which supports a wide range of interesting phenomena.

An understanding of the hot gas in clusters is of considerable importance. Observations of cluster gas can determine the cosmic distance scale (Silk & White 1978). Interaction between the gas and the cluster galaxies will affect the structure and evolution of both. Theories of star formation can be tested in a totally different environment from that in our own galaxy. If we knew where the gas came from we would understand more about conditions in the early universe. The eventual fate of the gas has implications for dark matter. Progress on these problems requires a good understanding of the present state of the gas.

In this thesis I consider the physical state of the hot intracluster medium. Two main areas will be considered. One is the properties of oscillations of the hot gas (sound waves and internal gravity waves)—their structure, evolution and excitation. The second is the rôle of magnetic fields in controlling heat flow and determining the structure of the gas.

Before embarking on this programme, let us first consider the basic properties of clusters of galaxies. It is convenient to classify observations by wavelength, as different wavebands convey information on different aspects, and different constituents, of clusters.

1.1 Optical Properties of Clusters

Galaxies are gregarious creatures, and are to be found clustered on many scales, from isolated galaxies, pairs, and small groups, to clusters and superclusters. Of these, rich clusters of galaxies are the largest gravitationally bound objects in the universe at the present time. Containing several thousand galaxies within a radius of a few Mpc, they have velocity dispersions of approximately a thousand $\mathrm{km\,s^{-1}}$. The richness of a cluster describes the enhancement of the galaxy density in a cluster relative to the background density of galaxies—rich clusters have a large excess density of galaxies.

Many clusters were found and catalogued by Abell (1958), and Zwicky *et al.* (1961-1968). In addition to genuine clusters these catalogues are contaminated by chance superpositions of unrelated objects which appear to be regions of enhanced galaxy density and are therefore classified as clusters. X-ray clusters are more robust, because you then know that there is a deep potential well for the X-ray emitting gas to occupy. Contamination can cause problems when attempting to deduce the velocity dispersion and hence the gravitational potential.

Clusters come in all shapes and sizes, from regular clusters which have smooth galaxy distributions and are highly concentrated to irregular clusters which are irregularly shaped, poorly concentrated and often show substructure. Irregular clusters tend to be rich in spiral galaxies whereas regular clusters contain few spiral galaxies. It is suspected, but not proven, that this is an evolutionary sequence, with regular clusters being the more evolved. Bautz & Morgan (1970) classified clusters according to the dominant galaxy: Bautz-Morgan Type I clusters are dominated by a single, central cD galaxy (see later), Type II clusters are dominated by a giant elliptical galaxy, and Type III clusters do not have a dominant galaxy. Rood & Sastry (1972) [revised by Struble & Rood (1982, 1984)] proposed a division into six classes: cD, dominated by a cD galaxy; B, dominated by a pair of luminous

galaxies; L, containing a linear chain of galaxies; C, with a core containing four of the ten brightest galaxies; F, appearing flattened; I, irregular.

The richest clusters tend to be of Bautz-Morgan Types I and II, or Rood-Sastry classes cD, B, L, C; to be rich in elliptical galaxies and poor in spirals, to be centrally concentrated and show little substructure in either real or velocity space.

Many clusters contain substructure. The galaxy distribution contains more than one peak, and the different peaks can have different mean velocities (Geller & Beers 1982; Fitchett 1988). Clusters are not spherically symmetric relaxed objects. This calls for some comment because in this thesis I consider an idealized cluster—spherically symmetric with little substructure. This is not unreasonable because the gas fills the potential and smooths out fine structure in the matter distribution. I also consider mainly the most relaxed clusters, which have the least substructure.

Many clusters have a central dominant (cD) galaxy at their centres. The properties of cD galaxies were defined by Matthews, Morgan & Schmidt (1964); they are similar to normal elliptical galaxies, but are larger and more luminous and those in rich clusters have an extended luminous halo that is not a simple continuation of the underlying galaxy profile.

Optical line emission is often found at or near the centres of clusters, often forming irregular filamentary structures (see, for example, Lynds 1970 and Cowie *et al.* 1983). Such line emission, not always resolved, is often associated with central cluster galaxies, and also with radio galaxies. As central cluster galaxies and strong radio sources are often one and the same, it is not clear whether the dominant influence is the presence of the cluster or the radio source. The properties of these line emitting clouds have recently been studied by Heckman *et al.* (1989).

1.2 Radio Properties of Clusters

Many galaxies in clusters contain radio sources, of all types, including the classical doubles Cygnus A and 3C295, assorted tailed sources such as NGC 1265 in the Perseus cluster, very distorted objects, and point (or compact) sources. The radio emission is due to synchrotron radiation from relativistic electrons gyrating in a magnetic field. The precise effect on a radio source of it being in a cluster, and the consequences for the cluster gas, are unclear.

Gull & Northover (1973) realised that a confining agency was necessary to stop the relativistic plasma responsible for the radio emission suffering enormous adiabatic expansion losses, and that a hot gaseous halo, proposed as one model to explain the X-ray emission observed in a few clusters of galaxies, was a natural candidate. A gaseous halo also provides a working surface for the observed hot spots in radio sources.

More evidence for the presence of hot gas comes from the existence of tailed radio sources in clusters (e.g., NGC1265 in Perseus; O'Dea & Owen 1986). This is interpreted as the radio emitting plasma being slowed down by the intracluster medium and being left behind as the radio galaxy moves on in its orbit in the cluster (just like smoke from a moving steam train).

Other cluster radio sources are very distorted, and appear to have been disturbed by 'cluster weather'. If intracluster gas is responsible for disturbing these radio sources this indicates that the gas is not simply smooth and static.

In addition to discrete sources, some clusters such as Coma, A2255 and A2319 contain radio halos (Hanisch 1987)—diffuse radio emission associated with the cluster as a whole rather than with individual galaxies. Radio halos are not common, for only a few have been found after extensive searches. (The detection of a low surface brightness radio halo is difficult, so a faint halo could be present in many clusters

and remain undetected.) Initially it was thought that halos were the result of many unresolved sources being superimposed. Higher resolution observations have not supported this model, although radio halos might be the result of a superposition of old (relic) radio galaxies for which the galactic activity ceased some 100 million years ago and the individual radio galaxies can no longer be identified.

Alternatively, radio halos might be the result of relativistic electrons being generally present in the intracluster gas. This might be due to leakage of relativistic electrons from cluster radio sources (Jaffe 1977), a secondary population of relativistic electrons caused by collisions between relativistic and ambient protons (Dennison 1980; Vestrand 1982), or relativistic electrons being produced in turbulent magnetic fields in galactic wakes (Roland 1981).

In the present context, radio halos are interesting because they involve magnetic fields in the intracluster medium, both from observational (Kim *et al.* 1987) and theoretical (Roland 1981; see also Jaffe 1980) viewpoints. The galactic wake model is also interesting from the point of view of energy input into the intracluster medium.

1.3 X-ray Properties of Clusters

A comprehensive review of X-ray emission from clusters of galaxies was given by Sarazin (1986). Forman & Jones (1982) reviewed imaging observations of clusters while Mushotzky (1984, 1985) reviewed spectroscopic observations.

The first extragalactic object to be identified as an X-ray source was M87 in the Virgo cluster (Byram, Chubb & Friedman 1966). The detection of X-ray emission associated with the Perseus and Coma clusters led Cavaliere, Gursky & Tucker (1971) to suggest that extragalactic X-ray sources were generally associated with groups or clusters of galaxies. This was confirmed by the *Uhuru* X-ray satellite (Giacconi *et al.* 1972,1974; Forman *et al.* 1978). It was established that,

(i) Clusters of galaxies are the most common bright extragalactic X-ray sources.

(ii) Clusters of galaxies are extremely luminous in X-rays, with a wide range of luminosities of order 10^{43}–$10^{45}\,\mathrm{erg\,s^{-1}}$.

(iii) The X-ray emission is extended and not time variable.

Two competing models for the origin of the X-ray emission from clusters of galaxies were that it was thermal emission from a hot ($\sim 10^8\,\mathrm{K}$) ionized plasma, or that it was due to Inverse Compton scattering of low energy photons (from the cosmic microwave background, or other stray photons) by a relativistic nonthermal plasma. The X-ray spectra from Ariel-V and OSO-8 were better fitted by thermal bremsstrahlung models than Inverse Compton ones (Mushotzky *et al.* 1978; Mitchell *et al.* 1979). The observation of line emission from highly ionized iron (Mitchell *et al.* 1976) was evidence heavily in favour of the thermal model, in which such emission arises naturally. The derived temperatures were in the range $2\times10^7\,\mathrm{K}$ to $2\times10^8\,\mathrm{K}$, with some clusters needing more than one temperature component to achieve a good fit. This shows that material at a range of temperatures is present.

The HEAO-1 satellite was much more sensitive and measured the luminosities of a large number of Abell clusters. It also provided much data on the X-ray spectra of clusters, especially at high energies.

A great step forward came with the launch of the *Einstein* X-ray observatory (Giacconi *et al.* 1979). This was a true X-ray imaging telescope. Using *Einstein* the X-ray emission from many clusters of galaxies was mapped. Low energy X-ray spectra were also obtained. These measurements, combined with those from the HEAO-1 satellite, showed conclusively that the origin of the X-ray emission was thermal bremsstrahlung from hot ($\sim 10^8\,\mathrm{K}$), tenuous ($\sim 10^{-3}\,\mathrm{cm^{-3}}$) gas in the gravitational potential well of the cluster.

The observed X-ray emission is a projection of the true three dimensional emission profile onto the plane of the sky. With some assumptions the observations can be deprojected to recover the three dimensional gas distribution. This process is not without uncertainty. Spatially resolved spectra would give details of the temperature structure and tie down the state of the intracluster medium much more precisely. Unfortunately they are not available at present, although future satellites should remedy this.

In addition to continuum emission, X-ray spectra also show line emission from atoms such as iron and oxygen. The major feature in the spectrum is a blend of lines from iron ions (Fe^{+24} and Fe^{+25}) and weaker lines from nickel, at an energy of approximately 7 keV. If the metals are distributed uniformly throughout the cluster, the gas must be at typically half solar metallicity in order to give the observed line strengths. The presence of large amounts of metals shows that a substantial proportion of the hot gas has been processed through stars, and has obvious implications for the origin of the gas. Observations of the Kβ line of Fe^{+24} in the Perseus and Centaurus clusters (Mitchell & Mushotzky 1980) not only proved that the emission was thermal in nature, but also that the gas was not isothermal.

Line emission from less highly ionized species is also seen in spectra of the hot gas. Many such lines were detected by the Solid State Spectrometer (SSS) on the *Einstein* satellite. (The *Einstein* mirror system didn't transmit above 4 keV and so the SSS couldn't observe the 7 keV iron line.) In general, these observations imply that material is present at lower temperatures than required to give the observed continuum emission. Lines from oxygen, magnesium, silicon and sulphur are seen in addition to iron. The SSS had only a small field of view and was pointed at the cluster centre, so the cool gas is present at the centre of the cluster. The cooling time of this gas is extremely short and this is evidence for cooling flows (see below, Section 1.4).

A general result of fitting models to spectra is that the gas is not isothermal—models with only a single temperature do not fit the observed spectrum well in most cases, while good fits can be achieved with more than one temperature component. In addition, the observed low energy lines require material to be present at an even wider range of temperatures.

Such a range of temperatures occurs if a temperature gradient is present. However, FPCS observations of Fe XVII line emission from the Perseus cluster (Canizares, Markert & Donahue 1988) show that material at different temperatures is mixed together: the cool gas associated with the Fe XVII line must be spread throughout the cluster out to a radius of 30 kpc in order not to violate the surface brightness constraints from imaging observations. If the cool gas is in pressure equilibrium with the surrounding hot gas it has a filling factor of only 1%. The remaining volume must be occupied by hotter gas so the intracluster medium contains coexisting phases.

The X-ray and optical morphologies of clusters are closely related. Clusters classified optically as irregular tend to have irregular X-ray emission with individual galaxies appearing as peaks in the X-ray emission. Regular clusters have smooth X-ray distributions with the X-ray emission not being peaked on individual galaxies, except possibly on a dominant central galaxy. These evolved clusters generally have high X-ray luminosities and gas temperatures.

1.4 Evolution of the intracluster medium

The hot gas is losing energy by thermal bremsstrahlung at a rate

$$\epsilon = 3.0 \times 10^{-27} T^{1/2} n_p^2 \,\mathrm{erg\,s^{-1}\,cm^{-3}}, \tag{1.1}$$

where T is the gas temperature and n_p the proton density per cubic centimetre. This formula assumes solar abundances and a temperature greater than 3×10^7 K.

At lower temperatures line cooling is important and the cooling rate is given by Raymond, Cox & Smith (1976). Cowie & McKee (1977) give the following approximation, valid in the region 10^5 to 4×10^7 K,

$$\epsilon \approx 6.2 \times 10^{-19} T^{-0.6} n_p^2 \,\mathrm{erg\,s^{-1}\,cm^{-3}}. \tag{1.2}$$

Thermal bremsstrahlung at the rate given by equation (1.1) results in cooling on a timescale

$$t_{\mathrm{cool}} \equiv \frac{dt}{d\log T} = 8.5 \times 10^{10} \left(\frac{n_p}{10^{-3}\,\mathrm{cm^{-3}}}\right)^{-1} \left(\frac{T}{10^8\,\mathrm{K}}\right)^{1/2} \mathrm{yr}, \tag{1.3}$$

which in many clusters is longer than the age of the universe, indicating that cooling is not an important process.

In some clusters, however, the central cooling time of the gas is much shorter than the age of the universe. Unless the energy of the gas is continually being replenished (either by heating processes or heat conduction) the gas at the centre must cool. It is then unable to support the gas at larger radii and is compressed. This results in a flow of gas to the centre of the system, the energy lost by cooling being balanced by gas flowing inward. Such 'cooling flows' (Fabian, Nulsen & Canizares 1984) can have mass flowing in at a rate of a few hundred solar masses per year.

The X-ray profiles are more centrally peaked than would be expected for isothermal gas at rest in the cluster gravitational potential. This excess is interpreted as being due to gas that is cooling. In addition, as noted in the previous Section, observations show that cool gas is present at the centres of some clusters.

More sophisticated analyses of cooling flows (Thomas, Fabian & Nulsen 1987) suggest that the mass flux varies with radius, approximately as $\dot{m} \propto r$. In this case material is cooling and being lost from the flow at all radii—little actually reaches the centre of the system. The fact that mass is deposited over a range of

radii implies that the gas is inhomogeneous, leading to a multiphase model of the intracluster medium (Nulsen 1986, 1988).

The experimental evidence provides conclusive proof of energy loss by intracluster gas, and of the presence of cold gas, but no evidence of an actual flow. There are also many uncertainties in deriving the flow properties from the X-ray surface brightness profile, including the uncertain temperature distribution, gravitational potential, and external pressure. In short, the cooling flow scenario suffers from an assortment of problems, some of which will be addressed in this thesis.

Why does the gas cool? Thermal conduction at the Spitzer (1962) rate can replace the energy lost at the centre of the system from outer hot gas. This is not such a problem for present day cooling flows, as the thermal conductivity is highly temperature dependent and, once a cooling flow is established and the centre of the system is cool, thermal conductivity is effectively switched off. Rather, the problem is one of creating a cooling flow from an initially hot gas distribution, as this would be prevented from cooling sufficiently to create a cooling flow in the first place. Standard cooling flow theology states that tangled magnetic fields reduce thermal conductivity to negligible levels (Stewart *et al.* 1984). Binney & Cowie (1981) argued that in order to fit the observed temperature profile around M87 thermal conductivity had to be reduced by at least two orders of magnitude. Others considered this implausible and constructed other models to explain the observations. Takahara & Takahara (1979) proposed that cold gas in M87 was being evaporated by hotter outlying material. Models in which inflow of material can be substantially reduced by conduction have been presented by Bertschinger & Meiksin (1986) and Meiksin (1988).

In addition to thermal conduction, other ways of balancing the radiative energy loss have been proposed. These include cosmic ray heating (Tucker & Rosner 1983 [in combination with thermal conductivity]), dynamical friction from galaxies

(Miller 1986), and supernova heating (Silk *et al.* 1986). Such models are often (but not necessarily) unstable; small deviations from equilibrium are enhanced by the heating process. It is also difficult to balance the heating and cooling processes exactly: either the heating process dominates and stops cooling, or is irrelevant—this is seen clearly in the conduction models of Bregman & David (1988), who found that only for a small range of values of thermal conductivity could the mass inflow rate be reduced while maintaining a temperature gradient. Bregman & David (1989) considered alternatives to the standard cooling flow scenario and found them wanting.

A cooling flow implies the accumulation of a substantial amount of material at the centre of the system. This matter may form the large cD galaxies often present, may form low mass (and therefore almost unobservable) condensations responsible for the 'dark matter' required to gravitationally bind the cluster, and may provide a fuel supply for a central radio source.

The final repository of the material deposited by a cooling flow has not yet been identified. Such a large amount of gas is not forming stars with the local initial mass function (IMF), as no evidence of such a large amount of star formation, particularly of more massive stars, is observed. In some clusters, e.g. Perseus, some star formation with massive stars is observed, but most clusters show some discrepancy. So, are the X-ray derived mass rates in error or is the IMF different from that in our own galaxy? Although there is, in principle, no reason to expect the IMF of stars from a cooling flow to be similar to that in the disk of our own galaxy (indeed, the physical conditions in the two cases are quite different and it would be very surprising if the resultant IMF were the same), there is widespread unease at the use of a different IMF.

Cooling flows are found in both rich and poor clusters, and the cooling flow phenomenon is also believed to be at work in elliptical galaxies (Forman, Jones &

Tucker 1985; Thomas *et al.* 1986). In this case the gas is supplied by mass loss from stars. Heating by supernovae is important in the energetics of the flow, but the broad features of galaxy and cluster cooling flows are similar. In both cases I believe that the major problem to be solved is the identification of the fate of the cooling gas.

1.5 Summary

With the above framework in place, let us examine the state of the hot gas in clusters of galaxies. I will start off by assuming the intracluster medium to be smooth and static and gradually introduce complications in the form of acoustic and internal gravity waves, the presence of individual galaxies, and magnetic fields.

In Chapter 2 the properties of oscillations (acoustic waves and internal gravity waves) will be analysed. Lagrangian perturbations of the hot gas will be used. I include the effects of a cooling flow and slow evolution. Formal expressions for the time evolution in the presence of thermal conduction and radiative cooling will be derived. I pay particular attention to the stability of disturbances in the hot gas.

The structure and excitation of these oscillations will be studied in Chapter 3. Wave solutions in the extreme g-wave and extreme p-wave case are derived. Excitation of sound waves by cluster galaxies, especially cD and central binary galaxies, leads to a calculation of the energy lost to sound waves at infinity. This calculation is not applicable to the excitation of g-waves. I estimate the amplitude of the waves and find it to be large.

Before moving on to consider the effects of magnetic fields on hot gas, Chapter 4 considers the evidence for magnetic fields in clusters of galaxies, using Faraday rotation as a probe. After presenting general statistical arguments, I attempt to

derive the properties of the magnetic field in the Cygnus A cluster from a resolved rotation measure image. The inferred radial variation is shown to be reasonable, and is broadly consistent with the magnetic field being frozen into the inflowing gas. An application to the depolarization of double radio sources is also presented.

In Chapter 5 I move on to consider the effect of a tangled magnetic field on the thermal state of the hot gas, by treating the tangled magnetic field as a random walk. Magnetic fields are shown to have a substantial effect on the temperature structure of the gas. They also (as was long suspected but never actually proved) reduce the flow of heat, although they do not necessarily reduce thermal conductivity.

Real (although not necessarily realistic) magnetic fields are considered in Chapter 6. Examples of magnetic field lines are shown. This gives a clearer picture of the structure of tangled magnetic fields than is common in the literature. Some of the calculations of Chapter 5 are repeated and the results compared to those of the random walk model.

A short summing up is given in Chapter 7, where I attempt to bring the various threads of argument together into a coherent description.

Chapter 2. Oscillations in Clusters of Galaxies

In this Chapter I consider the effect of perturbing the hot gas in cluster atmospheres. Much of the work in this Chapter is contained in a published paper (Tribble 1989a).

2.1 Introduction

Mathews & Bregman (1978) proposed that the optical filament systems found at the centres of some clusters of galaxies were due to thermal instability, with initially overdense regions cooling faster than their surroundings and becoming more overdense (see Field 1965 for a general discussion). This simple 'blob' picture was further elaborated by Cowie, Fabian & Nulsen (1980) and Nulsen (1986) and was accepted until Malagoli, Rosner & Bodo (1987; hereafter MRB) noted that the nature of the problem had not been correctly identified: parcels of gas oscillate around a mean position. MRB claimed to show that the gas is overstable, not simply monotonically unstable. Although the treatment of MRB appeared to give a good physical picture of the instability, it had several shortcomings that this Chapter aims to rectify. These are (i) the restriction to high wavenumber oscillations, (ii) the assumption of locality and (iii) an inability to handle the presence of a flow easily and correctly.

To analyse this problem, I consider the gas to be initially smooth and homogeneous, although stratified. Perturbations around such a distribution are considered. First, an Eulerian analysis is given and its limitations discussed. The problem is then reformulated in terms of Lagrangian perturbations and an expression for the stability coefficient given. The effect of a flow, such as occurs in cooling flow clusters, is then included. The stability coefficient is independent of whether or not a flow is present. Mass dropping out of or joining the flow can affect stability. In a

time dependent flow the modes evolve adiabatically if the period of oscillation is much shorter than the timescale of evolution of the background. No assumptions of isobaricity, locality or high wavenumber perturbations are made.

It then becomes apparent that the results of the Eulerian and Lagrangian calculations are contradictory. I show that this is because the two approaches are addressing two different questions and that the Lagrangian viewpoint is the more relevant. This then implies that the intracluster medium is thermally stable or only mildly unstable. Consequences of this for optical filament systems are discussed.

The analysis of oscillations in clusters of galaxies closely parallels that in stars (Cox 1980). In clusters of galaxies there are no complications in the background state due to nuclear energy generation, changing chemical composition and ionization. In contrast, clusters of galaxies often contain large scale cooling flows with their associated velocity fields and extend to very large (effectively infinite) radii. Real cooling flows are not spherically symmetric, but spherical symmetry should be a reasonable approximation at small radii. Turbulence and rotation will also be neglected. Although the underlying problem is the same for both stars and clusters of galaxies, the emphasis on which features are important is quite different.

2.2 The Eulerian Approach

The equations of hydrodynamics to be used are:

$$P = \frac{\rho k_B T}{\mu m_p} \tag{2.1}$$

$$\frac{\partial \rho}{\partial \mathrm{t}} + \nabla.(\rho \mathbf{v}) = \dot{m} \tag{2.2}$$

$$\frac{\partial \mathbf{v}}{\partial \mathrm{t}} + \mathbf{v}.\nabla\mathbf{v} + \frac{\nabla P}{\rho} + \nabla\Phi = 0, \tag{2.3}$$

together with the energy equation

$$\frac{P}{\gamma - 1}\left(\frac{\partial}{\partial \mathrm{t}} + \mathbf{v}.\nabla\right)\ln\left(\frac{P}{\rho^\gamma}\right) + \left(\frac{\rho}{\mu m_p}\right)^2 \Lambda - \nabla.(\kappa\nabla T) = 0. \tag{2.4}$$

The unperturbed state is assumed to be spherically symmetric, nonrotating, and essentially infinite in extent. The presence of individual galaxies is ignored, although these galaxies will be responsible for perturbing the intracluster medium and generating the waves we are considering (see Chapter 3). The emissivity $\Lambda \propto T^{\alpha}$ and the thermal conductivity $\kappa = f\kappa_{\rm Sp}T^{5/2}$ where $\kappa_{\rm Sp}$ is the Spitzer (1962) value of thermal conductivity. The factor f is a reduction factor which is believed to be much less than unity. It has been argued that mass is dropping out of cooling flows (Stewart *et al.* 1984), which leads to the introduction of the $\dot{m}$ term. The possible effect of this term (and corresponding extra terms in the momentum and energy equations) will only be considered in Section 2.3.3, where it is shown that it may be important.

2.2.1 BRUNT-VĀSĀILĀ WAVES

The solution of the Eulerian equations has been attempted by a number of authors (MRB; White & Sarazin 1987; Balbus 1986; Pallister 1987). This will be reviewed briefly so that points relevant to the present discussion can be emphasized. Denoting Eulerian perturbations by δ,

$$\delta F = F(\mathbf{r},t) - F_0(\mathbf{r},t), \tag{2.5}$$

time derivatives by dots, the perturbed velocity by $\mathbf{u}$, and $\delta_F = \delta F/F$, the Eulerian equations may be written (for an ideal gas) as

$$\delta_P = \delta_\rho + \delta_T \tag{2.6}$$

$$\rho\dot{\delta}_\rho + \nabla.(\rho\mathbf{u}) = 0 \tag{2.7}$$

$$\dot{\mathbf{u}} + \mathbf{u}.\nabla\mathbf{v} + (\delta_P - \delta_\rho)\frac{\nabla P}{\rho} + P\frac{\nabla\delta_P}{\rho} = 0 \tag{2.8}$$

$$\dot{\delta}_P - \gamma\dot{\delta}_\rho + \Gamma\delta_\rho - \frac{\gamma\omega_{BV}^2}{g}u_r = 0. \tag{2.9}$$

Here the Brunt-Väsäilä frequency ω_{BV} and the dissipation term Γ are defined by

$$\omega_{BV}^2 = -\frac{g}{\gamma}\frac{d\ln(P/\rho^\gamma)}{dr} \quad \text{where} \quad g = -\nabla_r\Phi, \tag{2.10}$$

$$\Gamma\delta_\rho = (\gamma-1)\frac{\Lambda}{P}\left(\frac{\rho}{\mu m_p}\right)^2(2\delta_\rho + \alpha\delta_T - \delta_P)$$
$$-(\gamma-1)\frac{\kappa_{Sp}}{P}\{\nabla.[f(T^{7/2}\nabla\delta_T + \frac{7}{2}T^{5/2}\delta_T\nabla T)] - \delta_P\nabla.(fT^{5/2}\nabla T)\}. \tag{2.11}$$

In the case where $\mathbf{v}$ is zero, eliminating the velocity $\mathbf{u}$ leads to the two equations

$$\rho\ddot{\delta}_\rho - \nabla.[(\delta_P - \delta_\rho)\nabla P + P\nabla\delta_P] = 0 \tag{2.12}$$

$$\ddot{\delta}_P - \gamma\ddot{\delta}_\rho + \Gamma\dot{\delta}_\rho + \frac{\gamma\omega_{BV}^2}{\rho g}[(\delta_P - \delta_\rho)\nabla_r P + P\nabla_r\delta_P] = 0. \tag{2.13}$$

A local dispersion relation can now be derived, as given by MRB [although they neglected the term $\mathbf{u}.\nabla\mathbf{v}$ in equation (2.8)]. An alternative derivation is given here. We look for solutions with wavelengths that are short compared to a pressure scale height, and are of low frequency. Then in equation (2.12) the dominant terms are $\nabla.(P\nabla\delta_P)$ and $\nabla.(\delta_\rho\nabla P)$. Define the small quantity

$$\epsilon = \frac{k_r\nabla_r P}{k^2 P} \approx \lambda/h, \tag{2.14}$$

where h is a pressure scale height, so ϵ is much less than unity. Then

$$\delta_P = i\epsilon\delta_\rho + O(\epsilon^2), \tag{2.15}$$

and the oscillations are not isobaric, but are nearly so.

We can also assume that the dissipation timescale (determined by Γ) is long compared to the period of the oscillation. Then to leading order the energy equation (2.13) is

$$-\gamma\ddot{\delta}_\rho - \gamma\frac{k_t^2}{k^2}\omega_{BV}^2\delta_\rho = 0, \tag{2.16}$$

which has solution

$$\delta_\rho \sim \exp(i\omega t), \qquad \text{where} \quad \omega^2 = \frac{k_t^2}{k^2}\omega_{BV}^2. \tag{2.17}$$

In the absence of Γ the solution is time reversible and stable, so the frequency ω must remain real to all orders in ϵ. Therefore the only interesting correction to order ϵ is the dissipation term. Thus to order ϵ

$$\omega^2 + \frac{i\omega\Gamma}{\gamma} - \frac{k_t^2}{k^2}\omega_{BV}^2 = 0, \tag{2.18}$$

which yields

$$\delta_\rho \sim \exp\left(i\frac{k_t}{k}\omega_{BV}t\right)\exp\left(\frac{\Gamma t}{2\gamma}\right). \tag{2.19}$$

In the absence of thermal conductivity, this leads to overstable oscillations whose amplitude is increased by radiative losses. Thermal conductivity preferentially damps the shorter wavelength oscillations.

The relevance of the Eulerian approach, first given by MRB, is that it demonstrates the mechanism of instability simply. It does, however, have some drawbacks. The inclusion of a flow greatly complicates matters. There is a choice between using inertial coordinates or comoving coordinates. Using inertial coordinates involves handling the flow explicitly, which is difficult. In comoving coordinates the amplitude will be a function of time, even in the absence of dissipation, because the amplitude of oscillation will in general be a function of position in the flow. In the local plane wave approximation, the wavelength is chosen sufficiently small to ensure that the change in amplitude over one wavelength is negligible. In a cooling flow the relevant distance is that travelled in a flow time which includes many wavelengths and the change in amplitude on this timescale may be considerable. In addition, as the following Lagrangian analysis shows, the conclusion of instability is misleading. Eulerian considerations of instability are not relevant when a parcel of gas can move towards a new equilibrium position. A fuller discussion of this point will be given at the end of this Chapter.

The root of the problem is that the Eulerian equations are difficult to solve, and a high wavenumber plane wave attack is successful because it avoids having

to include the large scale structure present in the oscillations. In problems where the large scale structure is important the plane wave approach fails badly. The inclusion of a flow necessitates that the large scale structure is known even for small wavelength oscillations.

2.3 Lagrangian Analysis

In the previous Section problems with the high wavenumber Eulerian approach were found. Some of these problems can be avoided by using the Lagrangian displacement $\boldsymbol{\xi}$ instead of the Eulerian perturbed quantities. The linearized perturbed equations are now given in terms of $\boldsymbol{\xi}$.

The notation of Shapiro & Teukolsky (1983) is used. To summarize, Eulerian perturbations are the difference between perturbed and unperturbed quantities at a fixed point, whereas Lagrangian perturbations refer to the same element of fluid, displaced by $\boldsymbol{\xi}$

$$\Delta F = F(\mathbf{r} + \boldsymbol{\xi}(\mathbf{r}, t), t) - F_0(\mathbf{r}, t). \tag{2.20}$$

Expanding ΔF shows that the two operators Δ and δ are related to first order in $\boldsymbol{\xi}$ by

$$\Delta = \delta + \boldsymbol{\xi}.\boldsymbol{\nabla}. \tag{2.21}$$

This relation allows us to use whichever of δ or Δ is the more convenient for evaluating a given quantity. It should be noted that the Eulerian δ commutes with space and time derivatives whereas the Lagrangian Δ commutes with the total time derivative. It is this that makes the analysis in the presence of a background flow easier in the Lagrangian formalism.

The continuity equation and perturbed velocity are given by

$$\Delta\rho = -\rho\boldsymbol{\nabla}.\boldsymbol{\xi}; \quad \delta\rho = -\boldsymbol{\nabla}.(\rho\boldsymbol{\xi}) \tag{2.22}$$

$$\Delta \mathbf{v} = \frac{d\boldsymbol{\xi}}{dt}. \tag{2.23}$$

The Eulerian perturbed velocity $\mathbf{u}$ is related to $\Delta\mathbf{v}$ by

$$\Delta \mathbf{v} = \delta \mathbf{v} + \boldsymbol{\xi}.\nabla \mathbf{v} = \mathbf{u} + \boldsymbol{\xi}.\nabla \mathbf{v} \tag{2.24}$$

$$\mathbf{u} = \frac{d\boldsymbol{\xi}}{dt} - \boldsymbol{\xi}.\nabla \mathbf{v} = \frac{\partial \boldsymbol{\xi}}{\partial \mathrm{t}} + \mathbf{v}.\nabla \boldsymbol{\xi} - \boldsymbol{\xi}.\nabla \mathbf{v}. \tag{2.25}$$

Acting with δ upon the equation of motion (2.2) and using (2.25) to eliminate $\mathbf{u}$ leads to the perturbed equation of motion

$$\frac{\partial^2 \boldsymbol{\xi}}{\partial \mathrm{t}^2} + 2\mathbf{v}.\nabla \frac{\partial \boldsymbol{\xi}}{\partial \mathrm{t}} + (\mathbf{v}.\nabla)^2 \boldsymbol{\xi} - \boldsymbol{\xi}.\nabla(\mathbf{v}.\nabla \mathbf{v}) + \delta\left(\frac{\nabla P}{\rho} + \nabla \Phi\right) = 0. \tag{2.26}$$

The perturbed gravitational potential is

$$\begin{aligned}
\delta\Phi(\mathbf{r}) &= -G \int \frac{\delta\rho(\mathbf{r}')}{|\mathbf{r} - \mathbf{r}'|}\, d^3\mathbf{r}' \\
&= G \int \frac{\nabla.'(\rho' \boldsymbol{\xi}')}{|\mathbf{r} - \mathbf{r}'|}\, d^3\mathbf{r}' \\
&= -G \int \rho' \boldsymbol{\xi}'.\nabla' \frac{1}{|\mathbf{r} - \mathbf{r}'|}\, d^3\mathbf{r}',
\end{aligned} \tag{2.27}$$

where the last expression has involved integrating by parts and dropping a surface term.

The energy equation can be written in the form

$$\frac{dS}{dt} + (\gamma - 1)\Theta = 0, \tag{2.28}$$

where from equation (2.4)

$$S = \ln(P/\rho^\gamma); \qquad \Theta = \frac{1}{P}\left[\left(\frac{\rho}{\mu m_p}\right)^2 \Lambda - \nabla.(\kappa \nabla T)\right]. \tag{2.29}$$

The perturbed form of equation (2.28) is

$$\begin{aligned}
0 &= \frac{d\Delta S}{dt} + (\gamma - 1)\Delta\Theta \\
&= \frac{d}{dt}\left[\frac{\Delta P}{P} - \gamma \frac{\Delta\rho}{\rho}\right] + (\gamma - 1)\Delta\Theta \\
&= \frac{d}{dt}\left[\frac{\Delta P}{P} - \gamma \frac{\Delta\rho}{\rho}\right] + (\gamma - 1)[\Theta_{P,\rho}\Delta P + \Theta_{\rho,P}\Delta\rho] \\
&= \frac{d}{dt}\left[\frac{\delta P + \boldsymbol{\xi}.\nabla P + \gamma P \nabla.\boldsymbol{\xi}}{P}\right] \\
&\quad + (\gamma - 1)[\Theta_{P,\rho}(\delta P + \boldsymbol{\xi}.\nabla P) - \rho\Theta_{\rho,P}\nabla.\boldsymbol{\xi}],
\end{aligned} \tag{2.30}$$

where

$$\Theta_{X,Y} = \left(\frac{\partial \Theta}{\partial X}\right)_Y .$$

I now assume that the oscillation timescale given by ω is much shorter than the flow timescale. In this case the total time derivative is a partial time derivative to the desired accuracy, and

$$\begin{aligned} i\omega(\delta P + \boldsymbol{\xi}.\boldsymbol{\nabla} P + \gamma P \boldsymbol{\nabla}.\boldsymbol{\xi}) &= (\gamma - 1)P[\Theta_{P,\rho}(\delta P + \boldsymbol{\xi}.\boldsymbol{\nabla} P) - \rho \Theta_{\rho,P} \boldsymbol{\nabla}.\boldsymbol{\xi}] \\ \delta P \left(1 - \frac{P(\gamma-1)\Theta_{P,\rho}}{i\omega}\right) &= -\boldsymbol{\xi}.\boldsymbol{\nabla} P - \gamma P \boldsymbol{\nabla}.\boldsymbol{\xi} \\ &\quad + \frac{(\gamma-1)P}{i\omega}(\Theta_{P,\rho}\boldsymbol{\xi}.\boldsymbol{\nabla} P - \rho\Theta_{\rho,P}\boldsymbol{\nabla}.\boldsymbol{\xi}). \end{aligned} \tag{2.31}$$

The left hand side can be divided to give δP in terms of $\boldsymbol{\xi}$,

$$\begin{aligned} \delta P &= -\boldsymbol{\xi}.\boldsymbol{\nabla} P - \gamma P \boldsymbol{\nabla}.\boldsymbol{\xi} - \frac{(\gamma-1)P}{i\omega - (\gamma-1)P\Theta_{P,\rho}}(\gamma P \Theta_{P,\rho} + \rho\Theta_{\rho,P})\boldsymbol{\nabla}.\boldsymbol{\xi} \\ &= \delta_0 P - \frac{(\gamma-1)^2 P}{i\omega - (\gamma-1)P\Theta_{P,\rho}} \tau \Theta_{\tau,S} \boldsymbol{\nabla}.\boldsymbol{\xi} \end{aligned} \tag{2.32}$$

where $\tau = P/\rho$ and $\delta_0 P$ is the isentropic value of δP:

$$\delta_0 P + \boldsymbol{\xi}.\boldsymbol{\nabla} P + \gamma P \boldsymbol{\nabla}.\boldsymbol{\xi} = 0. \tag{2.33}$$

If the oscillation time is short compared to the dissipation timescale then

$$\delta_P = \delta_0 P - \frac{P(\gamma-1)^2}{i\omega} \tau \Theta_{\tau,S} \boldsymbol{\nabla}.\boldsymbol{\xi}. \tag{2.34}$$

To summarize, the important equations are the equation of motion

$$\frac{\partial^2 \boldsymbol{\xi}}{\partial t^2} + 2\mathbf{v}.\boldsymbol{\nabla}\frac{\partial \boldsymbol{\xi}}{\partial t} + (\mathbf{v}.\boldsymbol{\nabla})^2\boldsymbol{\xi} - \boldsymbol{\xi}.\boldsymbol{\nabla}(\mathbf{v}.\boldsymbol{\nabla}\mathbf{v}) + \delta\left(\frac{\boldsymbol{\nabla} P}{\rho} + \boldsymbol{\nabla}\Phi\right) = 0, \tag{2.26}$$

where $\delta\Phi$ is obtained from equation (2.27) and δP is obtained from the energy equation

$$\delta P = -\boldsymbol{\xi}.\boldsymbol{\nabla} P - \gamma P \boldsymbol{\nabla}.\boldsymbol{\xi} - \frac{P(\gamma-1)^2}{i\omega - (\gamma-1)P\Theta_{P,\rho}} \tau \Theta_{\tau,S} \boldsymbol{\nabla}.\boldsymbol{\xi}. \tag{2.32}$$

2.3.1 THE STATIC ISENTROPIC CASE

The simplest case to consider is when the background is static (**v** zero) and the system is isentropic so that $\delta P = \delta_0 P$. Then total and partial time derivatives are the same and the equation of motion becomes

$$\frac{\partial^2 \boldsymbol{\xi}}{\partial t^2} + \frac{\boldsymbol{\nabla}\delta P}{\rho} + \frac{\boldsymbol{\nabla} P}{\rho^2}\boldsymbol{\nabla}.(\rho\boldsymbol{\xi}) + \boldsymbol{\nabla}\delta\Phi = 0. \tag{2.35}$$

Substituting for δP from the isentropic condition, equation (2.33), leads to the following equation for the displacement $\boldsymbol{\xi}$,

$$\frac{\partial^2 \boldsymbol{\xi}}{\partial t^2} - \frac{\boldsymbol{\nabla}(\boldsymbol{\xi}.\boldsymbol{\nabla} P + \gamma P \boldsymbol{\nabla}.\boldsymbol{\xi})}{\rho} + \frac{\boldsymbol{\nabla} P}{\rho^2}\boldsymbol{\nabla}.(\rho\boldsymbol{\xi}) + \boldsymbol{\nabla}\delta\Phi = 0. \tag{2.36}$$

In Appendix 2 I show that the system of equations (2.36) is self-adjoint, although not of Sturm-Liouville form. This means that the eigenfunctions corresponding to different eigenvalues are orthogonal, and that the eigenvalues themselves are real.

In the following I neglect the perturbed gravitational potential (the Cowling approximation). This means that we are not interested in the effects of self gravity. In the regime of interest self gravity is probably of minor importance, although it must be considered in the later nonlinear evolution.

In general the vector $\boldsymbol{\xi}$ (neglecting toroidal oscillations) can be written as a sum of modes which are of the form

$$\boldsymbol{\xi} = \left[\xi_r(r), \xi_h(r)\frac{\partial}{\partial\theta}, \xi_h(r)\frac{1}{\sin\theta}\frac{\partial}{\partial\phi}\right] \mathrm{Y}_l^m(\theta,\phi)e^{-i\omega t}. \tag{2.37}$$

The three components of $\boldsymbol{\xi}$, for any given mode, can be expressed in terms of only two functions ξ_r and ξ_h, which are functions of r only. This, and the appearance of the spherical harmonics, are a consequence of the spherical symmetry of the problem.

Expressing $\boldsymbol{\xi}$ in the form (2.37), we may write the r and θ components of equation (2.36) in terms of the functions ξ_r and ξ_h:

$$-\omega^2\xi_r\,\mathrm{Y}_l^m - \frac{1}{\rho}\frac{\partial}{\partial r}\left(\xi_r\frac{\partial P}{\partial r}\mathrm{Y}_l^m + \gamma P\boldsymbol{\nabla}.\boldsymbol{\xi}\,\mathrm{Y}_l^m\right) + \frac{1}{\rho}\frac{\partial P}{\partial r}\boldsymbol{\nabla}.\boldsymbol{\xi}\,\mathrm{Y}_l^m + \xi_r\frac{\mathrm{Y}_l^m}{\rho^2}\frac{\partial P}{\partial r}\frac{\partial \rho}{\partial r} = 0 \tag{2.38}$$

$$-\omega^2\xi_h\frac{\partial \mathrm{Y}_l^m}{\partial \theta} - \frac{1}{r\rho}\frac{\partial}{\partial \theta}\left(\xi_r\frac{\partial P}{\partial r}\mathrm{Y}_l^m + \gamma P\boldsymbol{\nabla}.\boldsymbol{\xi}\,\mathrm{Y}_l^m\right) = 0 \tag{2.39}$$

where $\boldsymbol{\nabla}.\boldsymbol{\xi}$ represents the divergence without the associated θ, ϕ, or time dependence:

$$\boldsymbol{\nabla}.\boldsymbol{\xi} \equiv \left(\frac{1}{r^2}\frac{\partial}{\partial r}(r^2\xi_r) - \frac{l(l+1)}{r}\xi_h\right). \tag{2.40}$$

The above equations simplify to

$$\omega^2\xi_r + \frac{1}{\rho}\frac{\partial}{\partial r}\left(\xi_r\frac{\partial P}{\partial r} + \gamma P\boldsymbol{\nabla}.\boldsymbol{\xi}\right) - \frac{1}{\rho}\frac{\partial P}{\partial r}\boldsymbol{\nabla}.\boldsymbol{\xi} - \frac{\xi_r}{\rho^2}\frac{\partial P}{\partial r}\frac{\partial \rho}{\partial r} = 0 \tag{2.41}$$

$$\omega^2\xi_h + \frac{1}{r\rho}\left(\xi_r\frac{\partial P}{\partial r} + \gamma P\boldsymbol{\nabla}.\boldsymbol{\xi}\right) = 0. \tag{2.42}$$

Rearranging equation (2.42) gives ξ_h in terms of ξ_r,

$$\xi_h = -\frac{\gamma P^{1-1/\gamma}}{r\rho\alpha^2}\frac{1}{r^2}\frac{\partial}{\partial r}(r^2\xi_r P^{1/\gamma}), \tag{2.43}$$

where

$$\alpha^2 = \omega^2 - \frac{\gamma P}{\rho}\frac{l(l+1)}{r^2}. \tag{2.44}$$

Eliminating $\boldsymbol{\nabla}.\boldsymbol{\xi}$ from (2.41) and (2.42) gives

$$\omega^2\xi_r - \frac{1}{\rho}\frac{\partial}{\partial r}(r\rho\omega^2\xi_h) + \frac{1}{\gamma P\rho}\frac{\partial P}{\partial r}(r\rho\omega^2\xi_h + \xi_r\frac{\partial P}{\partial r}) - \frac{\xi_r}{\rho^2}\frac{\partial P}{\partial r}\frac{\partial \rho}{\partial r} = 0. \tag{2.45}$$

Finally, eliminating ξ_h and tidying up the result leads to

$$\frac{P^{1/\gamma}}{\rho}\frac{\partial}{\partial r}\left(\frac{\gamma\omega^2}{\alpha^2}P^{1-2/\gamma}\frac{1}{r^2}\frac{\partial}{\partial r}(r^2\xi_r P^{1/\gamma})\right) + (\omega^2 - \omega_{BV}^2)\xi_r = 0. \tag{2.46}$$

Note that this equation is exact. It is this equation that must be solved for the eigenfrequencies and eigenfunctions. It is only of Sturm-Liouville form in the case of radial oscillations, when ω^2 and α^2 are identical. For nonradial motions it is not linear in ω^2 and we would expect more than one branch to the dispersion relation.

At the high frequency, short wavelength end of the spectrum space derivatives of background quantities may be neglected and the dispersion relation $\omega^2 = c^2k^2$ for sound waves is obtained. The Brunt-Väsäilä frequency also appears as a natural frequency. For the low frequency (Brunt-Väsäilä) solutions ω^2 is negligible in (2.42), but not in (2.41) which contains ω_{BV}^2, so that Brunt-Väsäilä waves are characterized by

$$\xi_r \frac{\partial P}{\partial r} + \gamma P \nabla . \boldsymbol{\xi} \approx 0. \tag{2.47}$$

This has the consequence that for these modes

$$(\omega^2 - \omega_{BV}^2)\xi_r \approx 0, \tag{2.48}$$

which is of course not an exact expression but will be used later.

2.3.2 ENERGY, DISSIPATION AND INSTABILITY

The effect of dissipation (that is, departures from entropy conservation) must now be considered. The basic mechanism was illustrated in Section 2.2.1, where an overstable solution was given. An analysis in terms of the global modes described by $\boldsymbol{\xi}$ will now be given.

First the relevant details from perturbation theory are needed. If a perturbation $\epsilon V\boldsymbol{\xi}$ is added to equation (2.36), the new eigenfunctions and eigenvalues may be expanded as

$$\begin{aligned} \boldsymbol{\xi}_i &= \boldsymbol{\xi}_i^0 + \sum_{k \neq i} a_i^k \epsilon \boldsymbol{\xi}_k^0 + \sum_{k \neq i} b_i^k \epsilon^2 \boldsymbol{\xi}_k^0 \quad \ldots \\ \omega_i^2 &= \omega_{0,i}^2 + \epsilon \Delta_1^i + \epsilon^2 \Delta_2^i \quad \ldots \end{aligned} \tag{2.49}$$

We substitute this into the perturbed equation (2.36), multiply through by $\rho \boldsymbol{\xi}_j^{0*}$ and integrate over all space. Collecting coefficients of various powers of ϵ and considering the case $j = i$ gives the well known formula

$$\Delta_1^i = \epsilon \int \boldsymbol{\xi}_i^{0*} . V \boldsymbol{\xi}_i^0 \rho \, d^3\mathbf{r}. \tag{2.50}$$

The full expression for δP, equation (2.32), perturbs equation (2.36) by

$$\epsilon V \boldsymbol{\xi} = -\frac{1}{\rho}\boldsymbol{\nabla}\left[\frac{(\gamma-1)^2 P}{i\omega-(\gamma-1)P\Theta_{P,\rho}}\tau\Theta_{\tau,S}\,\boldsymbol{\nabla}.\boldsymbol{\xi}\right]. \tag{2.51}$$

If the unperturbed frequency is ω_0 then

$$\begin{aligned}\omega^2 &= \omega_0^2 - \int \boldsymbol{\xi}^*.\boldsymbol{\nabla}\left[\frac{(\gamma-1)^2 P\tau\Theta_{\tau,S}\boldsymbol{\nabla}.\boldsymbol{\xi}}{i\omega-(\gamma-1)P\Theta_{P,\rho}}\right] d^3\mathbf{r} \\ &= \omega_0^2 + \int \frac{(\gamma-1)^2 P\tau\Theta_{\tau,S}|\boldsymbol{\nabla}.\boldsymbol{\xi}|^2}{i\omega-(\gamma-1)P\Theta_{P,\rho}}\, d^3\mathbf{r} \\ &= \omega_0^2 + \int \frac{(\gamma-1)^2 P[-i\omega^*-(\gamma-1)P\Theta_{P,\rho}]\tau\Theta_{\tau,S}|\boldsymbol{\nabla}.\boldsymbol{\xi}|^2}{|i\omega-(\gamma-1)P\Theta_{P,\rho}|^2}\, d^3\mathbf{r}, \end{aligned} \tag{2.52}$$

and we can split the frequency into its real and imaginary parts, $\omega = \omega_r + i\omega_i$. Equating the imaginary parts on both sides of equation (2.52) gives

$$2\omega_r\omega_i = \int \frac{(\gamma-1)^2\omega_r P\tau\Theta_{\tau,S}|\boldsymbol{\nabla}.\boldsymbol{\xi}|^2}{|i\omega-(\gamma-1)P\Theta_{P,\rho}|^2}\, d^3\mathbf{r}. \tag{2.53}$$

This expression gives ω_i for all oscillatory modes. If a mode does not oscillate but evolves monotonically in time then ω_r is zero and this expression cannot be used.

Equation (2.53) gives the imaginary contribution to ω due to the perturbation. This causes the oscillation amplitude to grow by a factor

$$\exp\left[-\frac{t}{2}\int \frac{(\gamma-1)^2}{\gamma}\frac{\gamma P}{\rho}\frac{\tau\Theta_{\tau,S}}{|i\omega-(\gamma-1)P\Theta_{P,\rho}|^2}|\boldsymbol{\nabla}.\boldsymbol{\xi}|^2\rho\, d^3\mathbf{r}\right]. \tag{2.54}$$

This is valid for all oscillations. In this expression, all factors except $\Theta_{\tau,S}$ are positive. Stability is therefore determined solely by the sign of $\Theta_{\tau,S}$. If the emissivity Λ is proportional to T^α then $\tau\Theta_{\tau,S} = (\alpha+1/2)\Theta$, and if cooling is due to thermal bremsstrahlung the gas is thermally stable. With line cooling (at temperatures less than 4×10^7 K) the gas is thermally unstable. Nothing whatsoever needs to be known about the structure of the eigenfunctions or what sort of a mode we have. The only assumptions made are that the mode is oscillatory and remains so in the presence of the perturbation, and that the flow time is long compared to the oscillation period.

If the unperturbed oscillation frequency is very small then the above analysis may not be accurate. This is because the perturbation may change the time behaviour from oscillatory to monotonic. It is difficult to study this effect because we need to know the actual eigenvalues and eigenfunctions. It should be noted that we can have waves (g-waves) of very low frequency. The modes affected are those with $k_t \ll k_r$, or with large tangential wavelengths compared to the radial wavelength. It is difficult to imagine such modes being excited, especially in an inhomogeneous intracluster medium.

Brunt-Väsäilä waves are characterized by being nearly divergence free:

$$\nabla.\boldsymbol{\xi} \sim -\frac{\xi_r}{\gamma}\frac{d\ln P}{dr} \tag{2.47}$$

and it is convenient to write ω_{BV}^2 in the form

$$\omega_{BV}^2 = -\frac{g}{\gamma}\frac{d\ln(P/\rho^\gamma)}{dr} = \frac{\gamma P}{\rho}\frac{1}{\gamma^2}\left(\frac{d\ln P}{dr}\right)^2\left(\frac{\gamma d\ln\rho}{d\ln P}-1\right). \tag{2.55}$$

Substituting these expressions into equation (2.54) gives the following expression for the growth factor:

$$\exp\left[-\frac{t}{2}\int\frac{(\gamma-1)^2}{\gamma}\frac{\omega_{BV}^2\tau\Theta_{\tau,S}}{|i\omega-(\gamma-1)P\Theta_{P,\rho}|^2}\left(\frac{\gamma d\ln\rho}{d\ln P}-1\right)^{-1}|\xi_r|^2\rho\,d^3\mathbf{r}\right]. \tag{2.56}$$

If the frequency is large (compared to $(\gamma-1)P\Theta_{P,\rho}$) then this can be simplified slightly to

$$\exp\left[-\frac{t}{2\omega^2}\int\frac{(\gamma-1)^2}{\gamma}\omega_{BV}^2\tau\Theta_{\tau,S}\left(\frac{\gamma d\ln\rho}{d\ln P}-1\right)^{-1}|\xi_r|^2\rho\,d^3\mathbf{r}\right]. \tag{2.57}$$

If the frequency is approximated by equation (2.48)

$$\omega^2 \approx \int\omega_{BV}^2|\xi_r|^2\rho\,d^3\mathbf{r}, \tag{2.58}$$

then this expression can be compared to that given by Balbus (1988). In both cases the isentropic derivative appears. There are two differences (i) the growth rate is

a global integral expression, not a local factor, and (ii) the growth rate is weighted by the Brunt-Väsäilä frequency squared. For a disturbance localized to a region in which the background variables remain constant (which is not an eigenfunction but would have to be constructed as a wavepacket), the results of Balbus (1988) are obtained.

2.3.3 INCLUDING THE FLOW

Now the flow must be included. To keep things as simple as possible, however, I assume the flow to be steady so that, although a velocity field is present, the background variables do not depend on time. The isentropic condition will be assumed to hold, although it must be remembered that this is not consistent with the existence of a flow. The aim is simply to keep the dynamics and energetics of the flow separated. First write equation (2.36) as

$$H_0\boldsymbol{\xi} = \omega^2\boldsymbol{\xi}. \tag{2.59}$$

The full equation of motion is then

$$H_0\boldsymbol{\xi} + (\mathbf{v}.\nabla)^2\boldsymbol{\xi} + 2\mathbf{v}.\nabla\frac{\partial\boldsymbol{\xi}}{\partial \mathrm{t}} - \boldsymbol{\xi}.\nabla(\mathbf{v}.\nabla\mathbf{v}) = \omega^2\boldsymbol{\xi}. \tag{2.60}$$

Define two operators $\mathbf{b}$ and $\mathbf{c}$ by

$$\mathbf{b}.\boldsymbol{\xi} \equiv (\mathbf{v}.\nabla)^2\boldsymbol{\xi} - \boldsymbol{\xi}.\nabla(\mathbf{v}.\nabla\mathbf{v}) \quad ; \quad \mathbf{c}.\boldsymbol{\xi} \equiv 2\mathbf{v}.\nabla\boldsymbol{\xi}. \tag{2.61}$$

First consider the operator $i\mathbf{c}$, which appears in equation (2.60) multiplied by ω. This is self-adjoint because

$$\int \boldsymbol{\xi}'^*.(\mathbf{v}.\nabla)\boldsymbol{\xi}\rho\, d^3\mathbf{r} = -\int \boldsymbol{\xi}.(\mathbf{v}.\nabla)\boldsymbol{\xi}'^*\rho\, d^3\mathbf{r}. \tag{2.62}$$

As shown by Lynden-Bell & Ostriker (1967) the presence of this term can alter the conclusions reached regarding the nature of the eigenvalues. Such complications will not be required in this case; the perturbation due to $\mathbf{c}$ is assumed small and so will not affect the reality of the eigenvalues.

For slow flows $\mathbf{c}$ is much larger than $\mathbf{b}$, so the change in frequency due to the flow is

$$\Delta\omega = \frac{1}{2\omega} i\omega \int \boldsymbol{\xi}'^{*}.(2\mathbf{v}.\nabla)\boldsymbol{\xi}\rho\, d^3\mathbf{r}$$

and the group velocity $\mathbf{v}_g$ changes by

$$\Delta\mathbf{v}_g = i\nabla_{\mathbf{k}} \int \boldsymbol{\xi}'^{*}.(\mathbf{v}.\nabla)\boldsymbol{\xi}\rho\, d^3\mathbf{r} \approx \mathbf{v} \tag{2.63}$$

in the high wavenumber limit where $\boldsymbol{\xi} \sim e^{-i\mathbf{k}.\mathbf{x}}$, so that all high wavenumber wavepackets comove with the flow.

Now consider the operator $\mathbf{b}$, and form in the usual way

$$\begin{aligned}
A &= \int [\boldsymbol{\xi}'^{*}.\mathbf{b}.\boldsymbol{\xi} - \boldsymbol{\xi}.(\mathbf{b}.\boldsymbol{\xi})'^{*}]\rho\, d^3\mathbf{r} \\
&= \int [\boldsymbol{\xi}'^{*}.(\mathbf{v}.\nabla)(\mathbf{v}.\nabla)\boldsymbol{\xi} - \boldsymbol{\xi}'^{*}.(\boldsymbol{\xi}.\nabla)(\mathbf{v}.\nabla\mathbf{v}) \\
&\qquad + \boldsymbol{\xi}.(\boldsymbol{\xi}'^{*}.\nabla)(\mathbf{v}.\nabla\mathbf{v}) - \boldsymbol{\xi}.(\mathbf{v}.\nabla)(\mathbf{v}.\nabla)\boldsymbol{\xi}'^{*}]\rho\, d^3\mathbf{r} \\
&= \int [-(\mathbf{v}.\nabla\boldsymbol{\xi}'^{*}).(\mathbf{v}.\nabla\boldsymbol{\xi}) + (\mathbf{v}.\nabla\boldsymbol{\xi}).(\mathbf{v}.\nabla\boldsymbol{\xi}'^{*}) \\
&\qquad - \xi_r'^{*}\xi_r \frac{\partial}{\partial r} v_r \frac{\partial v_r}{\partial r} + \xi_r \xi_r'^{*} \frac{\partial}{\partial r} v_r \frac{\partial v_r}{\partial r}]\rho\, d^3\mathbf{r} \\
&= 0.
\end{aligned} \tag{2.64}$$

Surface terms have been dropped and it is assumed that $\nabla.(\rho\mathbf{v})$ is everywhere zero. Therefore $\mathbf{b}$ is a self-adjoint operator. The consequences of $\nabla.(\rho\mathbf{v})$ being non zero will be considered later in this Section, but at present the interest is purely in the dynamics of the flow.

Some conclusions can now be stated. I have shown that the purely dynamical effect of the flow does not change the nature of the problem from the static case.

If a local treatment were made this conclusion would not necessarily be reached. The reason for this is that the amplitude of oscillation at a point remains constant, but an individual element will continually change the amplitude of its oscillation to keep step with its local oscillation amplitude.

The strategy is now clear. The above result implies that the solution for the case including the flow will not differ in character from the static case, and the effect of the flow on the modes will be to act as a (perhaps small) perturbation. It is therefore possible to analyse the static case, neglecting the presence of the operators **b** and **c**, and have confidence that the solutions thus obtained are good approximations to the real solutions of the problem including the flow. In particular, the growth or damping rate of modes will be almost the same in both cases, provided the correct form of the energy equation is used. Equation (2.56) is therefore a valid expression for the growth of modes not only in the static case for which it was derived but also for the more general case where a flow is present.

Equation (2.64) shows that, if $\nabla.(\rho\mathbf{v})$ is everywhere zero, then the operator **b** was self-adjoint. In the case of an accretion flow onto a solid body, a neutron star for example, we would expect $\nabla.(\rho\mathbf{v}) = 0$. In the case of clusters of galaxies and elliptical galaxies, however, material is believed to be dropping out of the flow at a range of radii, and material may also be added to the flow by mass loss from individual galaxies. It is therefore now necessary to consider what effect the inclusion of mass loss or gain has on the stability of the solutions.

Considering **b** as a perturbation of H_0, the change in the eigenvalues is

$$\Delta = \int \{\boldsymbol{\xi}^*.(\mathbf{v}.\nabla)(\mathbf{v}.\nabla)\boldsymbol{\xi} - \boldsymbol{\xi}^*.[\boldsymbol{\xi}.\nabla(\mathbf{v}.\nabla\mathbf{v})]\}\rho\, d^3\mathbf{r}. \tag{2.65}$$

The second term in the integrand is purely real and cannot lead to instability. Integrating by parts and neglecting both surface terms and those that are obviously real leaves

$$-\int \boldsymbol{\xi}^*.(\mathbf{v}.\nabla)\boldsymbol{\xi}\,\nabla.(\rho\mathbf{v})\, d^3\mathbf{r}, \tag{2.66}$$

and a growth rate (given by $\mathrm{Im}(\Delta)/2\omega$) of

$$\frac{\int[\boldsymbol{\xi}.(\mathbf{v}.\nabla)\boldsymbol{\xi}^* - \boldsymbol{\xi}^*.(\mathbf{v}.\nabla)\boldsymbol{\xi}]\nabla.(\rho\mathbf{v})\,d^3\mathbf{r}}{4i\omega}$$
$$\approx \int \frac{1}{2\omega}|\xi_r|^2 v_r k_r \nabla.(\rho\mathbf{v})\,d^3\mathbf{r} \qquad (2.67)$$

where I have assumed $\xi_r \sim e^{-ik_r r}$. It can be seen that mass dropping out of or being added to the flow can affect stability, although the effect is probably small. The precise effect depends on the sign of both $\nabla.(\rho\mathbf{v})$ and k_r. The removal or addition of mass will also involve the transfer of energy, so that an extra term will be present in the energy equation. Since the energetics of such mass transfer are not well understood, this point will not be pursued further.

2.3.4 NON STEADY FLOWS

So far the discussion has been restricted to the case where the background variables $(P, \rho, T, \mathbf{v})$ are not explicit functions of time. All real cooling flows evolve, at present rather slowly, but perhaps on short timescales early in their history. The time evolution of cooling flows is not well understood but it is clear that some evolution must take place.

It would of course be possible to include the time dependence explicitly in our equations, and then use perturbation theory to study the consequences. This would be restricted to the case where the evolution occurs over timescales long compared to the oscillation period. In this limit, however, the change is adiabatic so that a system in an eigenstate n given by $\boldsymbol{\xi}_n$ remains in that eigenstate. The amplitude will change adiabatically so we can write

$$\xi \sim a(t)\mathrm{e}^{-i\int \omega \mathrm{d}t}$$
$$\dot{\xi} \sim (\dot{a} - i\omega a)\mathrm{e}^{-i\int \omega \mathrm{d}t}$$
$$\ddot{\xi} \sim (\ddot{a} - 2i\dot{a}\omega - ia\dot{\omega} - \omega^2 a)\mathrm{e}^{-i\int \omega \mathrm{d}t}.$$

At any time the value of ω^2 is given by the instantaneous value of H_0, so neglecting $\ddot{a}$ as a small term the amplitude evolves as

$$\frac{2\dot{a}}{a} + \frac{\dot{\omega}}{\omega} = 0 \quad ; \quad a \sim \omega^{-1/2}. \tag{2.68}$$

This can easily be cast into another form. The velocity $\Delta \mathbf{v} = \dot{\boldsymbol{\xi}} \sim \omega^{+1/2}$ so that the energy $E \sim \omega$ and E/ω is an adiabatic invariant, as might have been expected.

2.4 Relating Eulerian and Lagrangian results

The Eulerian and Lagrangian analyses give contradictory criteria for stability. The Eulerian result indicates overstability, whereas the Lagrangian analysis implies stability (for bremsstrahlung cooling). Are they indeed contradictory? Which result is correct?

The apparent contradiction arises because we are not asking the same question in the two cases. Let us be clear about exactly what the results imply. In the Eulerian case, we are considering the evolution of the overdensity relative to an unperturbed parcel of gas at our current position,

$$\delta_\rho = \delta\rho(t)/\rho(0). \tag{2.69}$$

In other words, the overdensity, as a fraction of some fiducial density, grows with time. In the Lagrangian view the perturbations are always relative to the instantaneous equilibrium position. If the evolution of the system causes the equilibrium position of a fluid element to move, Eulerian and Lagrangian results will not agree.

The hot gas in clusters is unstable (according to an Eulerian analysis) because it loses energy faster than its surroundings. Its mean density must then increase, and its equilibrium position moves inward. We are interested solely in the stability of the gas relative to its continually changing equilibrium state, not relative to some

arbitrary initial state. The Lagrangian analysis shows that, in these terms, cluster gas is thermally stable.

The Lagrangian result states that, if a single mode is present, then cooling (by thermal bremsstrahlung) will cause the amplitude of the mode to decay. The evolution of an element of gas moving with the inward flow is due to two causes: the change in amplitude due to the change in conditions and the effects of dissipation. The Lagrangian result indicates that the amplitude of a perturbation rises less rapidly as it is convected inward than would be the case without cooling. The overdensity of a parcel of gas might rise as the gas moves inward, but this has nothing to do with thermal instability.

A full comparison of the Eulerian and Lagrangian results thus requires a knowledge of the structure of the modes, so that the variation of amplitude with radius is known. A demonstration of this using plane waves in a comoving frame has been given by Balbus & Soker (1989a).

2.5 Discussion

The evolution of the hot thermal plasma in clusters of galaxies is difficult to analyse because it is essential to include in the analysis the gravitationally induced stratification of the medium in the unperturbed equilibrium (or quasiequilibrium) state—failure to take this inhomogeneity into account seriously undermined analyses prior to MRB since gravitational stratification causes the classical Field thermal instability to become an overstability of smaller growth rate. In Section 2.2.1 I recovered this result with an Eulerian formulation similar to MRB. This analysis has two major shortcomings: (i) it is valid only for wavelengths much shorter than a pressure scale height, and (ii) it is difficult to modify so as to include the effect of

a steady cooling flow. Therefore in Section 2.3 I reformulate the problem posed by a general flowing atmosphere in Lagrangian form.

It is helpful to proceed in two stages. One first neglects cooling and the background flow, and then adds them back in as perturbations of the linearized equations. The oscillations of a static adiabatic atmosphere are governed by a system of self-adjoint equations [equation (2.36)]. In the case of spherical symmetry, neglecting toroidal modes leads to a single self-adjoint equation [equation (2.46)] which is of Sturm-Liouville form when the motions are entirely radial. The self-adjoint form of the underlying equations makes it easy to determine the effects of perturbations due to the background flow and cooling. I find that the 'growth' rate is an integral expression involving both the eigenfunctions and eigenvalues of the problem. This result, equation (2.56), contains the result of Balbus (1988) as a major part of the integrand. I have also shown that the inclusion of mass loss or gain in the flow will affect the instability criterion. More work is needed on the physics of the loss or gain process before the effect of this can be evaluated fully. The effect of a time dependent flow has also been considered and it has been shown that the modes will evolve adiabatically with E/ω being invariant.

The Eulerian and Lagrangian analyses give different (and apparently contradictory) stability criteria. This is because the Eulerian analysis fails to include the evolution of the mean density of a parcel of gas. The change in mean density causes the parcel of gas to move inwards. Relative to gas at the continually changing mean position, the density perturbation is damped. We may then conclude that hot gas in clusters is generally thermally stable. Optical filament systems do not arise from small thermally unstable perturbations going nonlinear (as was also concluded by Balbus 1988).

The damping time for the oscillations is not too dissimilar to the flow time, so that in fact little evolution takes place. This effect is again clearly seen in the

models of Loewenstein (1989).

One can therefore conclude that thermal instability in cluster gas has been widely misinterpreted in the past. It is not the cause of the optical filaments observed near the centres of some clusters—at least, not alone. Thermal instability can only exist if the perturbed material is pinned to the background flow in some way, whether by viscosity or magnetic fields. The origin of the optical filaments must be sought elsewhere.

2.5.1 COMMENT

The analysis presented is wholly global, although no solutions have been given. This is not a real problem. As emphasised in Section 2.3.2, stability can be discussed without reference to the structure of the modes, so long as the perturbation due to cooling and conductivity is small.

The solution of the equations must be found numerically. Although it may be possible to find some solutions by means of a high wavenumber approximation, it is not clear that this would be desirable, for two reasons. First, the observed filament structures in clusters of galaxies have dimensions that are not necessarily small compared to a scale height, and second, the very low order modes are of considerable interest. We would expect the low order global oscillation modes to be excited to non-infinitesimal amplitude by, for example, oscillating cD galaxies, central binary pairs of galaxies, the infall of small groups, and the merging of clusters. A study of these modes is therefore important, and a partial analysis of their structure and excitation is presented in the following Chapter.

Even if a 'blob' treatment (as opposed to expansion in eigenmodes) should prove to be appropriate, an oscillating blob of material will excite the waves considered here, leading to waves (and energy) propagating away from the blob. The

damping caused by this effect can only be calculated if the resultant waves are well understood.

Later discussion of the rôle of magnetic fields in determining the structure of the intracluster medium (Chapter 5) leads one to conclude that the gas in clusters is most probably highly inhomogeneous and therefore intrinsically nonlinear. Linear analysis of waves is inappropriate in these circumstances, and the theory must be revised.

Chapter 3. Structure and Excitation of Oscillations

In the previous Chapter the equations describing oscillations in cluster atmospheres were derived, and the effects of a cooling flow, mass deposition, radiative losses and (partially) thermal conductivity considered. I now move on to a more detailed examination of the structure of the eigenfunctions and the rôle of galaxy motions in exciting these oscillations. No attempt is made to calculate the excitation of g-waves, which is extremely difficult. Rather, I consider only losses into sound waves and treat this as a lower limit on the total emitted energy.

Binney (1988) considered the excitation of sound waves by a rotating triaxial galaxy in a homogeneous medium. He realized that excitation of internal gravity waves ('g-waves') is expected to be resonant because the Brunt-Väsäilä frequency ω_{BV} and the galaxy circular frequency Ω_c are similar, both being determined by the same gravitational potential. Indeed, as Balbus & Soker (1989b) point out,

$$\omega_{BV}^2 = \Omega_c^2 \left(\frac{3}{5} \frac{d\ln T}{d\ln r} - \frac{2}{5} \frac{d\ln \rho}{d\ln r} \right). \tag{3.1}$$

One might therefore expect resonant excitation of these waves to be an important process. Against this expectation is the fact that the propagation velocity of g-waves is small, so that although g-waves might be excited to large amplitudes, the energy flux they carry will be reduced. Before quantitative estimates of these energy losses can be given I examine the structure of the modes.

3.1 Structure of oscillations

Returning to equation (2.46), which we must solve for the eigenfunctions, let us consider the two quantities

$$\alpha^2 = \omega^2 - \frac{\gamma P}{\rho} \frac{l(l+1)}{r^2}, \tag{2.44}$$

$$\beta^2 = \omega^2 - \omega_{BV}^2, \tag{3.2}$$

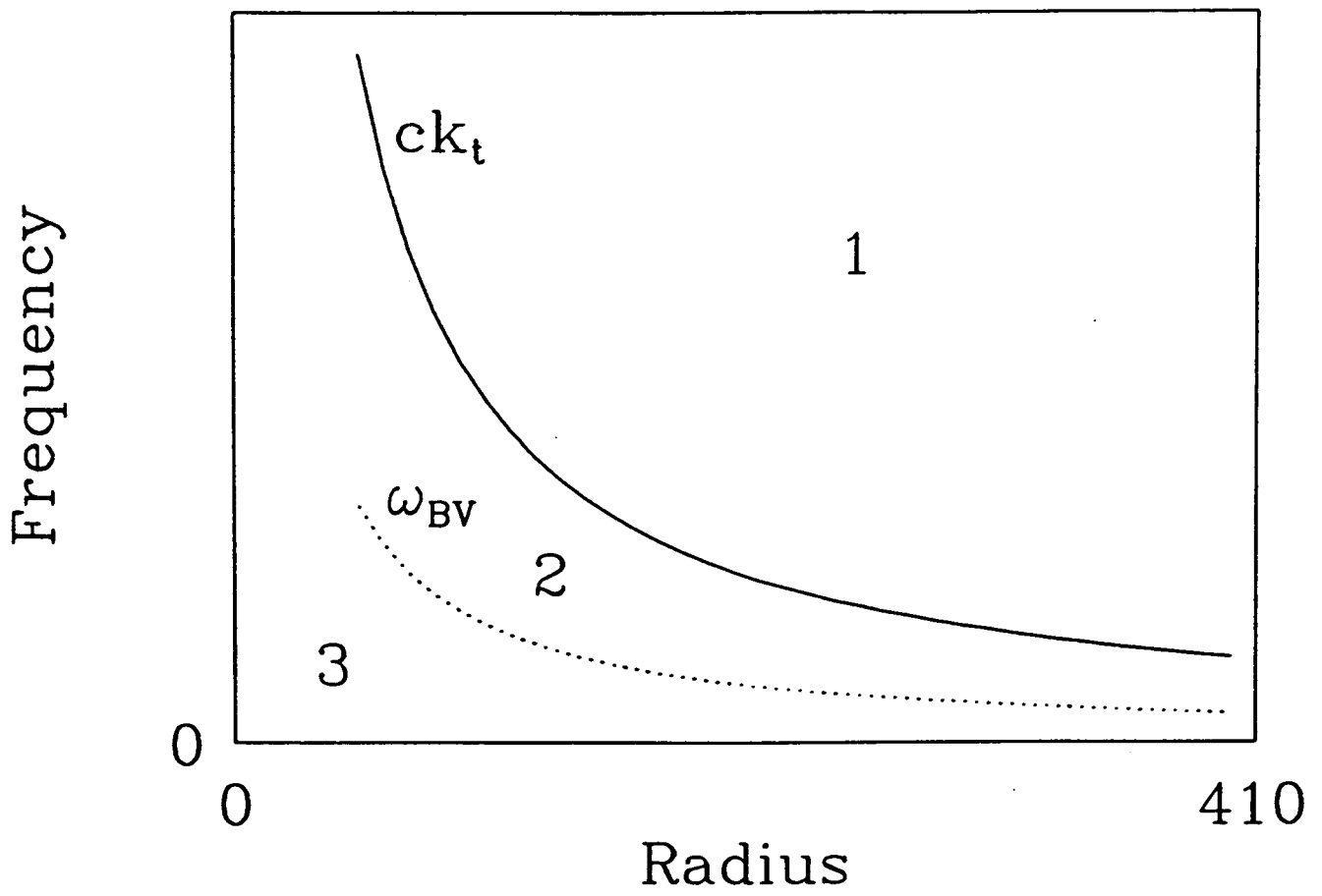

Figure 3.1. A sketch of the r-ω plane for an isothermal $1/r$ density profile. The plane is split into three regions by the two lines showing ω_{BV} and $ck_t(l=1)$ as a function of r. In region 1 there are oscillatory p-waves, in region 3 oscillatory g-waves, and nonoscillatory behaviour is found in region 2.

in terms of which we may write equation (2.46) in the form

$$\frac{P^{1/\gamma}}{\rho}\frac{\partial}{\partial r}\left(\frac{\gamma\omega^2}{\alpha^2}P^{1-2/\gamma}\frac{1}{r^2}\frac{\partial}{\partial r}(r^2\xi_r P^{1/\gamma})\right)+\beta^2\xi_r=0. \qquad (2.46)$$

We may distinguish three cases:

1) ω^2 large, so that α^2 and β^2 are both positive.

2) ω^2 taking intermediate values, so that α^2 and β^2 are of opposite signs.

3) ω^2 small, so that α^2 and β^2 are both negative.

In the short wavelength (large k) limit, equation (2.46) becomes similar to the simple harmonic oscillator equation,

$$\frac{d^2y}{dr^2}+qy=0,$$

where $q \propto \alpha^2\beta^2$. The nature of the solution depends on the sign of q, with an oscillatory solution if q is positive and an exponential (spatially damped) solution

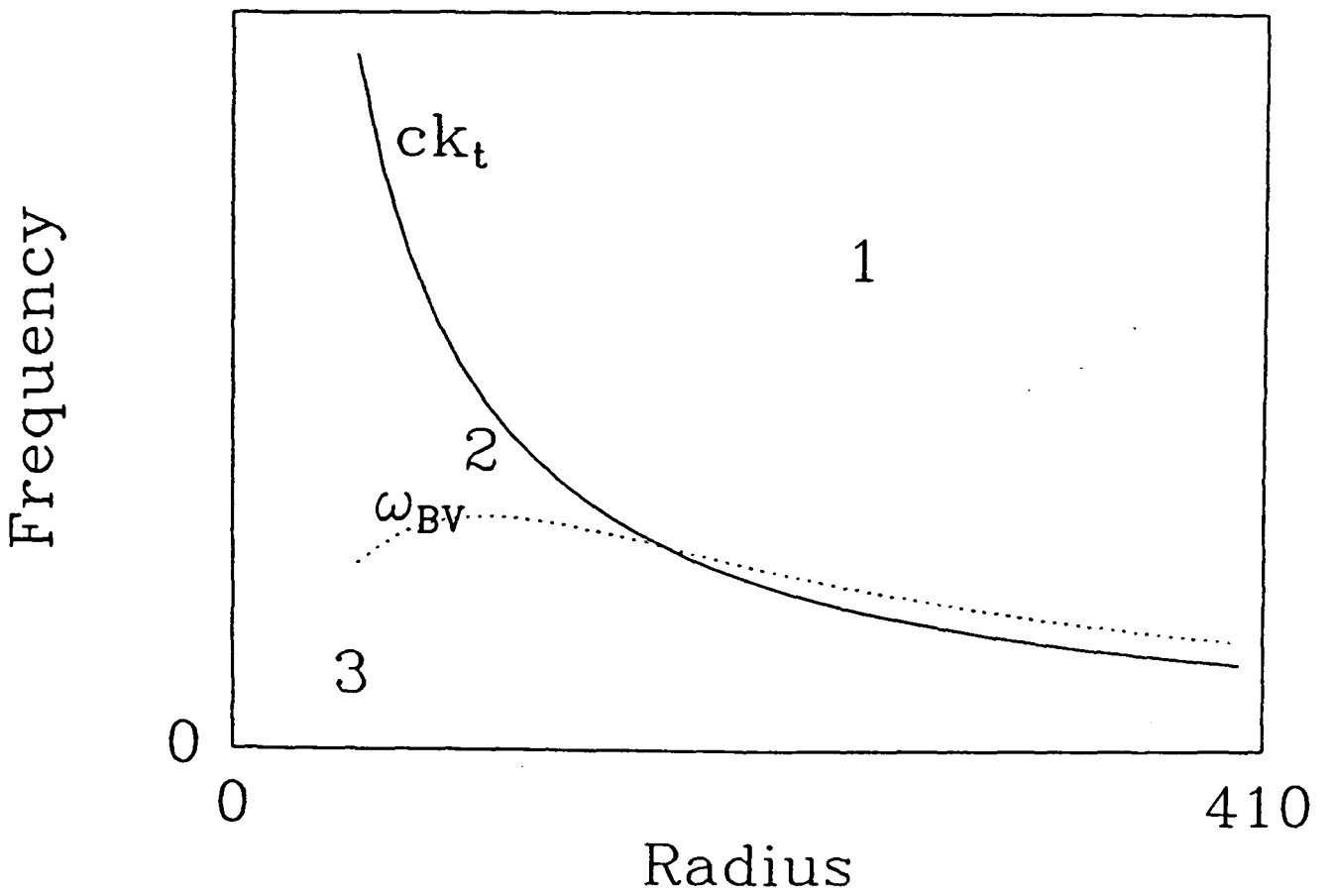

Figure 3.2. A sketch of the r-ω plane for an isothermal analytic King model with core radius 100. The plane is split into three regions by the two lines showing ω_{BV} and $ck_t(l = 1)$ as a function of r. In region 1 there are oscillatory p-waves, in region 3 oscillatory g-waves, and nonoscillatory behaviour is found in region 2.

if q is negative. We therefore expect oscillatory solutions for large and small ω^2, and an exponential (growing or damped) solution for intermediate values of ω^2.

Alternatively, one can consider the local dispersion relation derived from equation (2.46), which is

$$c^2\omega^2k^2 = \alpha^2\beta^2, \tag{3.3}$$

which shows that k is real when α^2 and β^2 are of the same sign and that k is imaginary (implying a spatially damped solution) when α^2 and β^2 are of opposite sign.

Similarly, for a given mode (a solution of fixed ω) we can distinguish three regions. At small r we get oscillatory g-wave behaviour, at large r the mode looks like a sound wave, and the two regions are joined by a nonoscillatory region. The three regions in the r-ω plane are shown in Figs. 3.1 and 3.2. A single mode corresponds to drawing a horizontal line across these figures.

In contrast, we can consider the situation at fixed r by drawing a vertical line on the figures. This would be the case if we were considering an object with a boundary (e.g., a star) or if we were deriving a local dispersion relation. We clearly see that low frequency g-waves and high frequency p-modes are present. This distinction of p-waves and g-waves is not so useful in a cluster which has no definite outer boundary. A given mode is of different character at different radii.

As long as the nonoscillatory region is avoided, equation (2.46) can be simplified and solved in the extreme p-wave and extreme g-wave cases.

3.1.1 SOUND WAVES

At sufficiently large radii or sufficiently high frequency we can approximate both α^2 and β^2 by ω^2. We must then attempt to solve

$$\frac{\gamma P^{1/\gamma}}{\rho}\frac{\partial}{\partial r}\left(\frac{P^{1-2/\gamma}}{r^2}\frac{\partial}{\partial r}(r^2\xi_r P^{1/\gamma})\right)+\omega^2\xi_r=0. \tag{3.4}$$

This is of Sturm-Liouville form. Assuming a solution of the form $\xi_r = Ae^{ikr}/r$ and assuming k to be large we find that

$$\omega^2=\frac{\gamma P}{\rho}k^2=c^2k^2, \tag{3.5}$$

and

$$\frac{P'}{P}+\frac{2A'}{A}+\frac{k'}{k}=0. \tag{3.6}$$

Therefore the amplitude A varies as

$$A\sim\frac{1}{\sqrt{Pk}}\sim\sqrt{\frac{c}{P}}. \tag{3.7}$$

The power transmitted by the wave across a spherical surface at radius r is (Landau & Lifshitz 1959)

$$\dot{E}=\frac{1}{2}\int\rho v^2 v_g r^2\,d\Omega. \tag{3.8}$$

The velocity v is $\dot{\xi}_r \equiv \omega \xi_r$, where the frequency is independent of radius for a given mode, and the group velocity v_g for sound waves is the sound speed. Therefore

$$\dot{E} \propto \rho A^2 c \sim \frac{c^2}{p/\rho} \tag{3.9}$$

and thus a constant. The radial dependence of A ensures that energy is conserved by the wave.

3.1.2 INTERNAL GRAVITY WAVES

Neglecting ω^2 equation (2.46) becomes

$$\frac{P^{1/\gamma}}{\rho}\frac{\partial}{\partial r}\left(\frac{\omega^2\rho}{l(l+1)P^{2/\gamma}}\frac{\partial}{\partial r}(r^2\xi_r P^{1/\gamma})\right) + \omega_{BV}^2 \xi_r = 0. \tag{3.10}$$

This can be written in the form

$$\frac{P^{2/\gamma}}{\rho}\frac{\partial}{\partial r}\left(\frac{\rho}{P^{2/\gamma}}\frac{\partial}{\partial r}(r^2\xi_r P^{1/\gamma})\right) + \frac{l(l+1)\omega_{BV}^2}{r^2\omega^2} r^2\xi_r P^{1/\gamma} = 0. \tag{3.11}$$

In the short wavelength limit we get

$$\frac{P^{1/\gamma}}{\sqrt{\rho}}\frac{\partial^2}{\partial r^2}\left(\frac{\sqrt{\rho}}{P^{1/\gamma}} r^2\xi_r P^{1/\gamma}\right) + \frac{l(l+1)\omega_{BV}^2}{r^2\omega^2} r^2\xi_r P^{1/\gamma} = 0. \tag{3.12}$$

Now assume that P and ρ vary as power laws of radius so that $\omega_{BV}^2 \sim 1/r^2$. Then, with $y = \sqrt{\rho} r^2 \xi_r$ and $\eta^2 = l(l+1)r^2\omega_{BV}^2/\omega^2$, equation (3.12) can be written

$$\frac{\partial^2 y}{\partial r^2} + \eta^2 \frac{y}{r^4} = 0, \tag{3.13}$$

which has an approximate solution

$$y \sim e^{i\eta/r}. \tag{3.14}$$

Define a radial wavenumber k_r by $k_r r = \eta/r$, so $k_r = \eta/r^2$ with $\eta \propto 1/\omega$. Then at small radii k_r is much greater then k_t, and $k_t^2\omega_{BV}^2/k^2 \approx k_t^2\omega_{BV}^2/k_r^2$ which

is independent of radius, so that the structure of the mode changes with radius to keep the local oscillation frequency in step with the fixed mode frequency. The group velocity is then

$$v_g = \frac{d\omega}{dk_r} = -\frac{(\eta\omega)}{k_r^2 r^2} = -\frac{\omega}{k_r} = -\frac{r^2\omega}{\eta}. \tag{3.15}$$

The group velocity is equal in magnitude and opposite in sign to the phase velocity, and both are proportional to r^2.

The energy transported by the wave is

$$\dot{E} \propto \rho r^2 v^2 v_g \propto \rho \xi_r^2 r^4,$$

where $\xi_r \propto 1/(r^2\sqrt{\rho})$. So the amplitude again varies to ensure energy conservation by the wave.

3.2 General theory of wave excitation

We proceed by adding a small time-dependent gravitational potential as a perturbation to the problem discussed in the previous chapter. Initially the case of a homogeneous background will be considered (see also Binney 1988) which limits the discussion to sound waves but is simpler than a more general analysis. Only small modifications are required if the background is stratified, but the discussion is still limited to sound waves.

3.2.1 SCALAR APPROACH

The unperturbed state is characterized by the density and pressure being independent of position and time, and no velocity field or gravitational potential. Therefore

the perturbed continuity equation and equation of motion are

$$\begin{aligned} \frac{\partial \delta\rho}{\partial t} + \rho_0 \nabla.\mathbf{v} &= 0 \\ \rho_0 \frac{\partial \mathbf{v}}{\partial t} + c^2 \nabla \delta\rho + \rho_0 \nabla \Phi &= 0. \end{aligned} \tag{3.16}$$

where the energy equation (with no losses) has been used to give $\delta P = c^2 \delta\rho$.

We now introduce a velocity potential ψ where $\mathbf{v} = \nabla\psi$, in terms of which the equations become

$$\begin{aligned} \frac{\partial \delta\rho}{\partial t} + \rho_0 \nabla^2 \psi &= 0 \\ \rho_0 \nabla \dot{\psi} + c^2 \nabla \delta\rho + \rho_0 \nabla \Phi &= 0. \end{aligned} \tag{3.17}$$

Differentiating the equation of motion with respect to time and substituting from the continuity equation leads to

$$\nabla \left[\left(\nabla^2 - \frac{1}{c^2} \frac{\partial^2}{\partial t^2} \right) \psi - \frac{\dot{\Phi}}{c^2} \right] = 0, \tag{3.18}$$

which implies that

$$\left(\nabla^2 - \frac{1}{c^2} \frac{\partial^2}{\partial t^2} \right) \psi = \frac{\dot{\Phi}}{c^2}. \tag{3.19}$$

3.2.2 VECTOR APPROACH

Using the perturbed equations (3.16) we substitute for $\mathbf{v}$ using the Lagrangian displacement $\boldsymbol{\xi}$ instead of the velocity potential,

$$\mathbf{v} = \frac{\partial \boldsymbol{\xi}}{\partial t}. \tag{3.20}$$

The perturbed equations are now

$$\begin{aligned} \delta\rho + \rho_0 \nabla.\boldsymbol{\xi} &= 0 \\ \rho_0 \frac{\partial^2 \boldsymbol{\xi}}{\partial t^2} - c^2 \nabla(\rho_0 \nabla.\boldsymbol{\xi}) + \rho_0 \nabla \Phi &= 0 \end{aligned} \tag{3.21}$$

which lead to

$$\nabla(\nabla.\boldsymbol{\xi}) - \frac{1}{c^2} \frac{\partial^2 \boldsymbol{\xi}}{\partial t^2} = \frac{\nabla \Phi}{c^2}. \tag{3.22}$$

If the velocity field (and hence $\boldsymbol{\xi}$) is irrotational then

$$\left(\nabla^2 - \frac{1}{c^2}\frac{\partial^2}{\partial t^2}\right)\boldsymbol{\xi} = \frac{\boldsymbol{\nabla}\Phi}{c^2}. \tag{3.23}$$

Note that equation (3.23) for $\boldsymbol{\xi}$ is similar to equation (3.19), and that both lead to

$$\left(\nabla^2 - \frac{1}{c^2}\frac{\partial^2}{\partial t^2}\right)\mathbf{v} = \frac{\boldsymbol{\nabla}\dot{\Phi}}{c^2}. \tag{3.24}$$

3.2.3 STRATIFIED WAVES

For wave excitation we are interested in the form of the solution at large radii. Then the solution of the previous Section may be used, and if $\xi_r = \chi/\sqrt{P/c}$,

$$\frac{\partial}{\partial r}\left(\frac{1}{r^2}\frac{\partial}{\partial r}(r^2\chi)\right) - \frac{1}{c^2}\frac{\partial^2\chi}{\partial t^2} = \frac{\boldsymbol{\nabla}\Phi}{c^2}\sqrt{P/c}. \tag{3.25}$$

This is again a standard wave equation with a source term.

3.2.4 SOLUTION

A perfectly good theory exists to solve this sort of problem, and is found in most electromagnetism and quantum theory textbooks. Consider equation (3.19), which can be written in the form

$$\left(\nabla^2 - \frac{1}{c^2}\frac{\partial^2}{\partial t^2}\right)\psi = -4\pi f, \tag{3.26}$$

where $f = -\dot{\Phi}/4\pi c^2$. This is solved in the usual way (Jackson 1975) by finding the time dependent Green function,

$$G^+ = \frac{\delta(t' - [t - |\mathbf{x} - \mathbf{x}'|/c])}{|\mathbf{x} - \mathbf{x}'|}, \tag{3.27}$$

so that the solution is

$$\psi = \iint d^3\mathbf{x}' dt' \frac{-\dot{\Phi}(\mathbf{x}', t')}{4\pi c^2} \frac{\delta(t' - [t - |\mathbf{x} - \mathbf{x}'|/c])}{|\mathbf{x} - \mathbf{x}'|}. \tag{3.28}$$

For generality assume that

$$\begin{aligned} \Phi &= \frac{1}{\sqrt{2\pi}} \int \tilde{\Phi} e^{-i\omega t}\, d\omega, \\ \dot{\Phi} &= \frac{-i}{\sqrt{2\pi}} \int \omega \tilde{\Phi} e^{-i\omega t}\, d\omega. \end{aligned} \tag{3.29}$$

Then

$$\begin{aligned} \psi(\mathbf{x}, t) = \frac{i}{\sqrt{2\pi}} \iiint d\omega\, dt'\, d^3\mathbf{x}' \\ \times \frac{1}{4\pi c^2} \frac{\omega \tilde{\Phi}(\mathbf{x}', \omega)}{|\mathbf{x} - \mathbf{x}'|} e^{-i\omega t'} \delta(t' - [t - |\mathbf{x} - \mathbf{x}'|/c]). \end{aligned} \tag{3.30}$$

The t' integral can be easily done:

$$\psi(\mathbf{x}, t) = \frac{i}{4\pi c^2 \sqrt{2\pi}} \iint d\omega\, d^3\mathbf{x}' \frac{\omega \tilde{\Phi}(\mathbf{x}', \omega)}{|\mathbf{x} - \mathbf{x}'|} e^{-i\omega t} e^{i\omega |\mathbf{x} - \mathbf{x}'|/c}. \tag{3.31}$$

The general procedure now is to find $\mathbf{v} = \nabla\psi$, and to integrate the energy flux $\rho v^2 c/2$ over a spherical surface at large radius. At large radius r

$$\mathbf{v}(\mathbf{x}, t) \approx \frac{-\mathbf{n}}{4\pi r c^3 \sqrt{2\pi}} \iint d\omega\, d^3\mathbf{x}'\, \omega^2 \tilde{\Phi}(\mathbf{x}', \omega) e^{-i\omega t} e^{i\omega r/c} e^{-i\omega \mathbf{n}.\mathbf{x}'/c} \tag{3.32}$$

where $\mathbf{n}$ is a unit vector in the direction of $\mathbf{x}$.

In the case of stratified waves, there is an extra factor of $\sqrt{P/c}$ in the integrand, and a corresponding factor outside the integral. The velocity $\mathbf{v}$ can thus be written as

$$\mathbf{v}(\mathbf{x}, t) \approx \frac{-i\omega \mathbf{n}}{4\pi r c^3 \sqrt{P(r)/c(r)}} e^{i\omega r/c} \int d^3\mathbf{x}' \sqrt{P(r')/c(r')} \dot{\Phi}(\mathbf{x}', t) e^{-i\omega \mathbf{n}.\mathbf{x}'/c}. \tag{3.33}$$

3.3 Oscillating central galaxy

It is widely believed that cD galaxies are at rest at the centres of their clusters. Such a belief was shown by Quintana & Lawrie (1982) to be consistent with the evidence then available, the cD galaxy having the same velocity as the cluster mean to within the errors. The errors were large, however, and other massive central (such as D) galaxies are allowed much more motion by the data. More recent observations show that the cD galaxy has a velocity different from the cluster mean in three cases: A1795 (Hill *et al.* 1988), A2029 (Bower, Ellis & Efstathiou 1988) and A2670 (Sharples, Ellis & Gray 1988). In each case the cD galaxy is moving at $\sim 400\,\mathrm{km\,s^{-1}}$ with respect to the cluster mean. It is then to be expected that massive central galaxies in clusters are not at rest with respect to the cluster, but have some motion. The other interesting case, that of a central binary pair of galaxies, is considered in the next Section.

I therefore consider the case where a central galaxy considered to be a point mass of mass M is executing simple harmonic motion at the bottom of the cluster potential well. The motion is taken to be along the z-axis.

In order to conserve momentum, the cluster must oscillate in antiphase. The emission depends critically on how the cluster responds to conserve momentum. If the cluster moves bodily then the following analysis applies, whereas if the momentum is conserved by a small fraction of the cluster near the cD then this cancels the dipole term in $\dot{\Phi}$ and the emission is due to the quadrupole term, which is much smaller. The distinction between the two cases is whether the balancing mass is interior or exterior to the region (about a wavelength across) where the waves are mostly excited. With this in mind, I calculate the dipole emission first, and then the quadrupole emission.

3.3.1 DIPOLE EMISSION

The gravitational potential of a point mass at position $\mathbf{r}_g(t)$ is

$$\Phi(\mathbf{x}', t) = -\frac{GM}{|\mathbf{x}' - \mathbf{r}_g(t)|}. \tag{3.34}$$

Φ may be expanded as a sum over spherical harmonics,

$$\Phi = -\frac{4\pi GM}{r_>} \sum_{l=0}^{\infty} \frac{1}{2l+1} \sum_{m=0}^{\infty} \mathrm{Y}_l^m(\theta', \phi') \mathrm{Y}_l^m(\theta_g, \phi_g) \left(\frac{r_<}{r_>}\right)^l, \tag{3.35}$$

where $r_>$ ($r_<$) is the greater (lesser) of r' or r_g. The potential is axisymmetric so we only have $m = 0$ terms, and

$$\Phi = -\frac{GM}{r_>} \sum_{l=0}^{\infty} P_l(\cos\theta') P_l(\cos\theta_g) \left(\frac{r_<}{r_>}\right)^l. \tag{3.36}$$

The galaxy is oscillating along the z-axis so $\theta_g = 0$ and $P_l(\cos\theta_g) = 1$. If the amplitude of the galaxy oscillation is small (r_g is much smaller than the wavelength of the oscillation that is being excited) then

$$\Phi = -\frac{GM}{r'} - \frac{GM}{r'^2} r_g P_1(\cos\theta'), \tag{3.37}$$

and

$$\dot{\Phi}(\mathbf{x}', t) = -\frac{GM}{r'^2} \dot{r}_g \cos\theta' = \frac{i\omega GMa\cos\theta'}{r'^2} e^{-i\omega t}, \tag{3.38}$$

where a is the amplitude of the galaxy oscillation. The velocity $\mathbf{v}$ is

$$\mathbf{v}(\mathbf{x}, t) \approx -\frac{GMa\omega^2}{4\pi r c^3 \sqrt{P(r)/c(r)}} \mathbf{n} e^{-i\omega(t - r/c)} \int d^3\mathbf{x}' \frac{\cos\theta'}{r'^2} \sqrt{P(r')/c(r')} e^{-ik\mathbf{n}.\mathbf{x}'}. \tag{3.39}$$

In terms of spherical polar coordinates, the cartesian components of $\mathbf{x}'$ and $\mathbf{n}$, and their scalar product, are (we are free to set $\phi = 0$ as the system has axial symmetry)

$$\begin{aligned} \mathbf{x}' &= (r'\sin\theta'\cos\phi', r'\sin\theta'\sin\phi', r'\cos\theta') \\ \mathbf{n} &= (\sin\theta, 0, \cos\theta) \\ \mathbf{n}.\mathbf{x}' &= r'(\cos\theta\cos\theta' + \sin\theta\sin\theta'\cos\phi'). \end{aligned} \tag{3.40}$$

Integrating over ϕ' using the result

$$J_0(br) = \frac{1}{2\pi}\int_0^{2\pi} e^{ibr\sin\phi'}\,d\phi' \tag{3.41}$$

gives

$$\mathbf{v}(\mathbf{x},t) \approx -\frac{GMa\omega^2}{2rc^3\sqrt{P(r)/c(r)}}\mathbf{n}e^{-i\omega(t-r/c)} \times \int dr'\sqrt{\frac{P(r')}{c(r')}}\,\sin\theta' d\theta'\,\cos\theta' e^{-ikr'\cos\theta\cos\theta'}J_0(kr'\sin\theta\sin\theta') \tag{3.42}$$

The integral over θ' is discussed in Appendix 3. We get

$$\mathbf{v}(\mathbf{x},t) \approx \frac{i\cos\theta GMa\omega^2}{rc^3\sqrt{P(r)/c(r)}}\mathbf{n}e^{-i\omega(t-r/c)}\int dr'\sqrt{P(r')/c(r')}\,j_1(kr'). \tag{3.43}$$

The total emitted power is

$$\begin{aligned}\dot{E} &= \frac{1}{2}\int \rho v^2 cr^2\,d\Omega \\ &= \frac{\rho c^2}{2P}\left(\frac{GMa\omega^2}{c^3}\right)^2\int\cos^2\theta\,d\Omega\left[\int dr'\sqrt{P(r')/c(r')}\,j_1(kr')\right]^2 \\ &= \frac{2\pi\rho c^2}{3P}\left(\frac{GMa\omega^2}{c^3}\right)^2\left[\int dr'\sqrt{P(r')/c(r')}\,j_1(kr')\right]^2.\end{aligned} \tag{3.44}$$

3.3.2 QUADRUPOLE EMISSION

I model the quadrupole as two point masses of mass M and M', oscillating in antiphase along the z-axis. The leading order (quadrupole) contribution to the time dependent potential is

$$\dot{\Phi}(\mathbf{x}',t) = -\frac{GM}{r'^3}2r_g\dot{r}_gP_2(\cos\theta') = \frac{2i\omega GMa^2P_2(\cos\theta')}{r'^3}e^{-i\omega t}, \tag{3.45}$$

and the velocity is

$$\mathbf{v}(\mathbf{x},t) \approx -\frac{2GMa^2\omega^2}{4\pi rc^3\sqrt{P(r)/c(r)}}\mathbf{n}e^{-i\omega(t-r/c)}\int d^3\mathbf{x}'\,\frac{P_2(\cos\theta')}{r'^3}\sqrt{P(r')/c(r')}e^{-ik\mathbf{n}.\mathbf{x}'}. \tag{3.46}$$

Integrating over ϕ' as before gives

$$\mathbf{v}(\mathbf{x},t) \approx -\frac{GMa^2\omega^2}{rc^3\sqrt{P(r)/c(r)}}\mathbf{n}e^{-i\omega(t-r/c)} \times \int \frac{dr'}{r'}\sqrt{\frac{P(r')}{c(r')}}\,\sin\theta'\,d\theta'\,P_2(\cos\theta')e^{-ikr'\cos\theta\cos\theta'}\,J_0(kr'\sin\theta\sin\theta') \quad (3.47)$$

and integrating over θ' (Appendix 3) we get

$$\mathbf{v}(\mathbf{x},t) \approx \frac{2i\cos\theta GMa\omega^2}{rc^3\sqrt{P(r)/c(r)}}\mathbf{n}e^{-i\omega(t-r/c)}\int \frac{dr'}{r'}\sqrt{P(r')/c(r')}\,j_2(kr'). \quad (3.48)$$

The total emitted power is

$$\begin{aligned}\dot{E} &= \frac{1}{2}\int \rho v^2 cr^2\,d\Omega \\ &= \frac{\rho c^2}{2P}\left(\frac{2GMa^2\omega^2}{c^3}\right)^2\int [P_2(\cos\theta)]^2\,d\Omega\left[\int \frac{dr'}{r'}\sqrt{P(r')/c(r')}\,j_2(kr')\right]^2 \\ &= \frac{2\pi\rho c^2}{5P}\left(\frac{2GMa^2\omega^2}{c^3}\right)^2\left[\int \frac{dr'}{r'}\sqrt{P(r')/c(r')}\,j_2(kr')\right]^2. \end{aligned} \quad (3.49)$$

3.3.3 POWER LAW PROFILES

It is easy to evaluate the integral over r' in equations (3.49) and (3.44) if the background variation is a power law function of radius. (We need to assume the sound speed c to be constant as only then is k constant.) Assuming this to be of the form

$$\frac{P}{c} \propto r^{-2\alpha},$$

then we wish to evaluate

$$\begin{aligned} I(dipole) &= \sqrt{\frac{c}{P}}\int dr'\,j_1(kr')\sqrt{P/c} \\ &= r^\alpha k^{-1}\int d(kr')\,J_{3/2}(kr')(r')^{-\alpha}\sqrt{\frac{\pi}{2kr'}} \\ &= r^\alpha k^{\alpha-1}\frac{\sqrt{\pi}}{2}\frac{\Gamma(1-\alpha/2)}{2^\alpha\Gamma([3+\alpha]/2)}, \end{aligned} \quad (3.50)$$

and

$$I(dipole) = \sqrt{\frac{c}{P}} \int \frac{dr'}{r'} j_2(kr') \sqrt{P/c}$$
$$= r^\alpha \int \frac{d(kr')}{kr'} J_{5/2}(kr')(r')^{-\alpha} \sqrt{\frac{\pi}{2kr'}}$$
$$= (kr)^\alpha \frac{\sqrt{\pi}}{2} \frac{\Gamma(1-\alpha/2)}{2(\alpha+1)\Gamma([5+\alpha]/2)}. \tag{3.51}$$

The ratio of quadrupole to dipole integrals is $k/(3+\alpha)$.

For the dipole emission, this can be evaluated for the cases $\alpha = 0$, corresponding to a homogeneous background, $\alpha = 1/2$, which might be typical for a cooling flow, and $\alpha = 1$, a more extreme case. The power lost is, in the homogeneous case,

$$\dot{E} = \frac{2\pi\rho c}{3} \left(\frac{GMa\omega}{c^2} \right)^2,$$

for $\alpha = 1/2$,

$$\dot{E} = \frac{4\pi^2\rho r c}{27k} \left(\frac{GMa\omega^2}{c^3} \right)^2,$$

and for $\alpha = 1$,

$$\dot{E} = \frac{\pi^3 r^2 \rho c}{24} \left(\frac{GMa\omega^2}{c^3} \right)^2.$$

The quadrupole emission is reduced by a factor $(3/5)(2ka/[3+\alpha])^2$ from the dipole case.

3.3.4 ESTIMATE OF ENERGY LOSSES

Given the result of the previous Section [equation (3.44)] we can now try and estimate the energy loss of a central galaxy due to emission of sound waves. This requires an estimate of the frequency. For this, I assume that the potential in which the galaxy moves can be described using the King analytic approximation to an

isothermal sphere. The frequency can then be expressed in terms of the observed velocity dispersion and core radius:

$$\omega^2 = \frac{4\pi G\rho}{3} = \frac{3\sigma_r^2}{r_c^2} \tag{3.52}$$

where σ_r is the line of sight velocity dispersion and r_c the core radius.

Assuming that the specific kinetic energies of the gas and the galaxies are the same, $c^2 = 3\sigma_r^2$. We then have that $\omega = c/r_c$, or $k = 1/r_c$. In this case the results for different values of α agree to within a factor of two, as long as all quantities are evaluated at r_c.

This gives the expression

$$\begin{aligned}\dot{E} &= 2\pi\rho\frac{G^2M^2a^2\sigma_r^2}{r_c^2c^3} \\ &= \frac{2\pi\rho}{3\sqrt{3}}\frac{G^2M^2}{\sigma_r}\left(\frac{a}{r_c}\right)^2 \\ &= 3.5\times10^{41}\mu n_{-3}\frac{M_{12}^2}{\sigma_{1000}}\left(\frac{a}{r_c}\right)^2 \mathrm{erg\,s^{-1}}.\end{aligned} \tag{3.53}$$

In this expression μ is the mean mass per electron in amu, n_{-3} is the electron density in $10^{-3}\,\mathrm{cm^{-3}}$, M_{12} is the galaxy mass in $10^{12}\,\mathrm{M_\odot}$, and σ_{1000} is the line of sight velocity dispersion in units of $1000\,\mathrm{km\,s^{-1}}$. If the galaxies are in thermal equilibrium then the kinetic energy of the central galaxy should be the same as the general cluster galaxies (of mass m), which implies that

$$\left(\frac{m}{M}\right) = \left(\frac{a}{r_c}\right)^2. \tag{3.54}$$

This allows the energy loss to be written in the form

$$\dot{E} = 3.5\times10^{41}\mu n_{-3}\frac{M_{12}m_{12}}{\sigma_{1000}}\,\mathrm{erg\,s^{-1}}. \tag{3.55}$$

The timescale for the central galaxy to lose its kinetic energy in this way is

$$\begin{aligned}t_D &= \frac{1}{2}Mv^2/\dot{E} \\ &= \frac{9\sqrt{3}}{4\pi\rho}\frac{\sigma_r^3}{G^2M} \\ &= \frac{2.7\times10^{12}}{\mu n_{-3}}\frac{\sigma_{1000}^3}{M_{12}}\,\mathrm{yr}.\end{aligned} \tag{3.56}$$

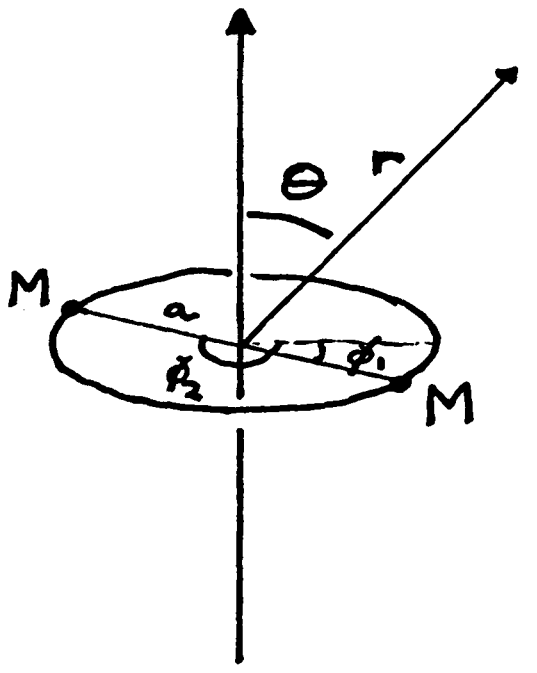

Figure 3.3. The geometry and coordinate system used in the calculation of the acoustic energy emitted by galaxies on circular orbits.

For the quadrupole case the emission is reduced by a factor $(3/5)(2ka/[3+\alpha])^2$. Observations indicate that the line of sight velocity of the cD is ~half the velocity dispersion, giving $a \sim r_c/2$, so the emission is reduced (and the energy loss timescales increased) by about a factor of twenty from the dipole case.

3.4 Central binaries

Clusters of galaxies often contain binary galaxies at their centres. These will also radiate sound waves. For the geometry used in this section see Fig. 3.3. I will assume that both galaxies are of equal mass M and that the orbits are circular and of radius a. The angular frequency of rotation is $\omega = \dot{\phi}$.

The potential due to the binary pair is

$$\Phi_b(\mathbf{x}', t) = -\frac{GM}{|\mathbf{x}' - \mathbf{r}_1(t)|} - \frac{GM}{|\mathbf{x}' - \mathbf{r}_2(t)|}. \tag{3.57}$$

We use equation (3.35) to express this in terms of spherical harmonics. We have

$\phi_2 = \phi_1 + \pi/2$ and $\theta_1 = \theta_2 = \pi/2$, so the potential for $r' > a$ is

$$\Phi_b = -\frac{GM}{r'} \sum_{l=0}^{\infty} \frac{4\pi}{2l+1} \sum_{m=0}^{\infty} Y_l^m(\theta', \phi')[1 + (-1)^m] Y_l^m(\pi/2, \phi_1) \left(\frac{a}{r'}\right)^l. \quad (3.58)$$

The only terms which make a nonzero contribution to $\dot{\Phi}$ have m even and $m \neq 0$. So again assuming that the orbital radius a is small compared to the wavelength of the wave excited, and rotating the coordinates so that $\phi_1 = \pi/4$ (the location of the coordinate origin is arbitrary, but this choice leads to a neater expression for $\dot{\Phi}_b$),

$$\dot{\Phi}_b(\mathbf{x}') = \frac{6GMa^2\omega}{r'^3} \sin^2\theta' \sin\phi' \cos\phi'. \quad (3.59)$$

In this case we do not have axial symmetry, so that

$$\mathbf{n}.\mathbf{x}' = r'[\sin\theta \sin\theta'(\cos\phi \cos\phi' + \sin\phi \sin\phi') + \cos\theta \cos\theta']. \quad (3.60)$$

The velocity is

$$\mathbf{v}(\mathbf{r}, t) = \frac{-i\omega}{4\pi r c^3 \sqrt{P(r)/c(r)}} \mathbf{n} e^{ikr} \int \dot{\Phi}_b e^{-ik\mathbf{n}.\mathbf{x}'} \sqrt{P(r')/c(r')}\, d^3\mathbf{x}'. \quad (3.61)$$

The integral over ϕ' is done first, and is

$$\begin{aligned} I_1 &= \int d\phi' \sin\phi' \cos\phi' \exp[-ikr' \sin\theta \sin\theta'(\cos\phi \cos\phi' + \sin\phi \sin\phi')] \\ &= \int d\phi'' \sin(\phi'' - \phi) \cos(\phi'' - \phi) \exp(-ikr' \sin\theta \sin\theta' \cos\phi''). \end{aligned} \quad (3.62)$$

Expanding the trigonometric functions, changing variables to $\mu = \cos\phi''$, using the result

$$\int_{-1}^{1} e^{ip\mu}(1 - \mu^2)^{\nu - 1/2}\, d\mu = J_\nu(p) \left(\frac{2}{p}\right)^\nu \Gamma(1/2)\Gamma(\nu + 1/2), \quad (3.63)$$

and the recurrence relation $J_{n+1}(x) = (2n/x)J_n(x) - J_{n-1}(x)$, leads to the result

$$I_1 = 2\pi \sin\phi \cos\phi J_2(kr' \sin\theta \sin\theta'). \quad (3.64)$$

Therefore,

$$\mathbf{v} = \frac{3GMa^2\omega^2}{rc^3\sqrt{P(r)/c(r)}}\mathbf{n}\sin\phi\cos\phi \times \int \frac{dr'}{r'}\sqrt{\frac{P(r')}{c(r')}}\,\sin^3\theta'\,d\theta'\exp(-ikr'\cos\theta\cos\theta')J_2(kr'\sin\theta\sin\theta'). \quad (3.65)$$

Referring to Appendix 3, the integral over θ' can be done, and the result is

$$\mathbf{v} = \frac{6GMa^2\omega^2}{rc^3\sqrt{P(r)/c(r)}}\mathbf{n}\sin^2\theta\sin\phi\cos\phi\int\frac{dr'}{r'}\sqrt{P(r')/c(r')}j_2(kr'). \quad (3.66)$$

The total emitted power is

$$\begin{aligned}\dot{E} &= \frac{1}{2}\int \rho v^2 cr^2\,d\Omega \\ &= \frac{\rho c^2}{2P}\left(\frac{6GMa^2\omega^2}{c^3}\right)^2\int\sin^4\theta\sin^2\phi\cos^2\phi\,d\Omega \\ &\qquad \times\left[\int\frac{dr'}{r'}\sqrt{P(r')/c(r')}\,j_2(kr')\right]^2. \end{aligned} \quad (3.67)$$

3.4.1 POWER LAW PROFILES

It is again easy to evaluate the integral over r' in equation (3.67) if the background variation is a power law function of radius. (We need to assume the sound speed c to be constant as only then is k constant.) Assuming this to be of the form

$$\frac{P}{c} \propto r^{-2\alpha},$$

then we wish to evaluate (as for the quadrupole case before)

$$\begin{aligned} I &= \sqrt{\frac{c}{P}}\int\frac{dr'}{r'}j_2(kr')\sqrt{P/c} \\ &= r^\alpha\int\frac{d(kr')}{kr'}J_{5/2}(kr')(r')^{-\alpha}\sqrt{\frac{\pi}{2kr'}} \\ &= (kr)^\alpha\frac{\sqrt{\pi}}{2}\frac{\Gamma(1-\alpha/2)}{2^{\alpha+1}\Gamma([5+\alpha]/2)}. \end{aligned} \quad (3.68)$$

This can be evaluated for the cases $\alpha = 0$, corresponding to a homogeneous background, $\alpha = 1/2$, which might be typical for a cooling flow, and $\alpha = 1$, a more extreme case. The power lost is, in the homogeneous case,

$$\dot{E} = \frac{2\pi\rho c}{15}\frac{1}{9}\left(\frac{6GMa^2\omega^2}{c^3}\right)^2,$$

for $\alpha = 1/2$,

$$\dot{E} = \frac{2\pi\rho c}{15}\frac{8\pi kr}{441}\left(\frac{6GMa^2\omega^2}{c^3}\right)^2,$$

and for $\alpha = 1$,

$$\dot{E} = \frac{2\pi\rho c}{15}\frac{\pi^2(kr)^2}{256}\left(\frac{6GMa^2\omega^2}{c^3}\right)^2.$$

3.4.2 ESTIMATE OF ENERGY LOSSES

For the different backgrounds, the numerical factors are within a factor of 3 of each other (the effect of changing the background is greater in the binary case because a higher order multipole is being excited), so as long as we evaluate the expressions at the radius where $kr = 1$, denoted by r_k, we will get a reasonable estimate for the energy loss.

For a binary system with separation $2a$, $\omega^2 = GM/4a^3$, $r_k = \sqrt{4a^3c^2/GM}$, and assuming that $3\sigma_r^2 = c^2$,

$$\begin{aligned}\dot{E} &= \frac{\pi\rho(r_k)}{30}\frac{G^4M^4}{9\sqrt{3}a^2\sigma_r^5} \\ &= 4\times10^{37}\mu n_{-3}(r_k)\frac{M_{12}^4}{(a/30\,\mathrm{kpc})^2\sigma_{1000}^5}\,\mathrm{erg\,s^{-1}}. \end{aligned} \tag{3.69}$$

The timescale for the loss of this energy by the binary pair is

$$\begin{aligned} t_b &= \frac{1}{2}2M(a\omega)^2/\dot{E} \\ &= \frac{30\times9\sqrt{3}a}{4\pi}\frac{\sigma_r^5}{G^3M^2\rho(r_k)} \\ &= 5.6\times10^{14}\frac{(a/30\,\mathrm{kpc})\sigma_{1000}^5}{M_{12}^2\mu n_{-3}(r_k)}\,\mathrm{yr}. \end{aligned} \tag{3.70}$$

Mean separations of binary galaxies in clusters (Struble & Rood 1982) are in the range 30–50 kpc, and even at the lower end of the range the energy loss is small. The wavelength corresponding to $a = 30\,\mathrm{kpc}$ is a few hundred kpc, and clusters with central binaries tend not to have cooling flows and may be described by King models. In this case the density may be approximated by that at the core radius. Note that the loss of energy by a binary pair of galaxies is much less than that of an oscillating central galaxy.

3.5 Emission in the stratified case

Recall that in the case of a stratified medium the power is calculated assuming that

$$\mathbf{v} = \frac{-i\omega}{4\pi r c^3}\mathbf{n}\frac{1}{\sqrt{P(r)/c(r)}}\int d^3\mathbf{x}'\,\sqrt{P(r')/c(r')}\,\dot{\Phi}e^{-ik\mathbf{n}.\mathbf{x}'}. \tag{3.71}$$

This allows only for the weighting of the integrand by the non-uniform background. It does not take into account the changed dynamics of the gas which would change the Green's function. As such, it is only an approximation. The effect of stratification on the dynamics of the gas is parameterized by the Brunt-Väsäilä frequency. The approximation will be valid provided the driving frequency is large compared to the Brunt-Väsäilä frequency over most of the region of interest.

The time dependent equation we must solve in the general case is equation (2.36) with a source term. This can be written for curl free displacements in the form,

$$\frac{\partial^2\boldsymbol{\xi}}{\partial t^2} - c^2\nabla^2\boldsymbol{\xi} - \frac{\nabla(\boldsymbol{\xi}.\nabla P) + \gamma\nabla.\boldsymbol{\xi}\nabla P}{\rho} + \frac{\nabla P}{\rho^2}\nabla.(\rho\boldsymbol{\xi}) = -\nabla\dot{\Phi}. \tag{3.72}$$

Although I will not attempt to derive the Green's function for this problem, I will point out that equation (3.72) is nothing more than the Klein-Gordon equation for a massive particle, where the mass of the particle depends on position. At large radii (p-waves) the mass term goes to zero and the solution is simple.

The dynamics alters the Green's function in the central regions where the Brunt-Väsäilä frequency is comparable to or greater than the exciting frequency. The integral we use to evaluate the emission has contributions from a region of size of order the wavelength λ. In the central galaxy case where we have a cooling flow with a isothermal $1/r$ density profile $\omega_{BV}^2 = 6c^2/25r^2$ and $\omega = 2\pi c/\lambda$. Therefore the two frequencies coincide at a radius

$$\frac{r}{\lambda} = \frac{\sqrt{6}}{10\pi}. \tag{3.73}$$

The region over which the dynamics is important is in this case small. The calculation presented is therefore a good estimate of the power lost in sound waves. This calculation cannot be used to study the excitation of g-waves directly.

Binary galaxy systems are not often found in cooling flows. We can therefore describe the density variation using the analytic King approximation. In this case the Brunt-Väsäilä frequency has a maximum value (see Fig. 3.2). The exciting frequency can in principle take any value. For the parameters chosen in equation (3.69) the frequency is similar to the maximum Brunt-Väsäilä frequency. For any case of interest (by which I mean an important loss of energy over a Hubble time) the driving frequency will be larger and the approximation better.

Balbus & Soker (1989b) have considered resonant g-wave excitation, and argue that g-waves are trapped in the core and cannot escape to infinity. This is obviously feasible—the non oscillatory region acts as a barrier and waves must tunnel through to the p-wave region. The width of the tunnelling region depends on the angular momentum eigenvalue l, so that high l waves are more efficiently trapped than are low l waves. Balbus & Soker (1989b) considered only high l waves, which will be effectively trapped, whereas I have considered only the lowest l wave that is excited, which can leak through the barrier quite easily. (Tunnelling cannot be an important process for p-waves as it doesn't depend on the stratification, and you know it has no effect in the homogeneous case.)

The total energy flux at infinity is little different in the stratified case compared to the homogeneous case. Stratification has little effect on the emission of sound waves.

3.6 Wave amplitudes

The amplitudes of the waves are not negligible. The most interesting case is that of waves from an oscillating central galaxy. The velocity in this case is, for quadrupole emission in the homogeneous case, from equation (3.48),

$$v(\mathbf{x},t) \approx \frac{2ka}{3}\frac{GMa\omega P_2(\cos\theta)}{rc^2}.$$

Using the King analytic approximation to an isothermal sphere, we get $\omega^2 = c^2/r_c^2$.

$$\begin{aligned}\frac{v(\mathbf{x},t)}{c} &\approx \frac{2a}{3r_c}\frac{GMaP_2(\cos\theta)}{rc^2r_c} \\ &\approx \frac{M_{12}a^2P_2(\cos\theta)}{\sigma_{1000}^2r_c^2}\left(\frac{r}{\text{kpc}}\right)^{-1}.\end{aligned} \tag{3.74}$$

So the speed relative to the sound speed is of order $1/r$ with r in kpc. This is only valid in the far zone with r a Mpc or so, but the amplitude is a fraction of a per cent (for quadrupole emission this is reduced by a factor of approximately three). The amplitude of p-waves in the near zone is expected to be large. G-waves will be of even larger amplitude.

As a first estimate of the amplitude of g-waves let us take the energy lost into sound waves as an order of magnitude estimate of the energy loss to g-waves, and calculate the resultant g-wave amplitude.

From equation (3.8), the power transported across a spherical surface of radius r is

$$\dot{E} = \frac{1}{2}\rho\bar{v^2}4\pi r^2 v_g \tag{3.75}$$

where v_g is $r^2\omega/\eta$. Therefore

$$\dot{E} = \frac{2\pi\rho\overline{v^2}r^4\omega^2}{\sqrt{l(l+1)}r\omega_{BV}}$$

and the dimensionless amplitude is

$$\overline{\left(\frac{v}{c}\right)^2} = \frac{\dot{E}r\omega_{BV}\sqrt{l(l+1)}}{2\pi\rho r^4 c^2\omega^2}. \tag{3.76}$$

For an isothermal $1/r$ density profile $\omega_{BV}^2 = 6c^2/25r^2$, and using the homogeneous result for $\dot{E}$,

$$\overline{\left(\frac{v}{c}\right)^2} = \frac{\sqrt{6l(l+1)}}{25r^4}\left(\frac{2GMa^2}{3c^2r_c}\right)^2$$

$$\left(\frac{v}{c}\right) \sim 0.4\left(\frac{a^2}{r_c r}\right)\left(\frac{\mathrm{kpc}}{r}\right)\frac{M_{12}}{\sigma_{1000}^2}. \tag{3.77}$$

This implies that large scale motions with velocities approaching the sound speed are quite plausibly excited in the centres of clusters. This fits in well with the observed large spread in velocities of optical filament systems. The oscillations may mask the velocity structure of the background flow, and complicate observations designed to observe the flow directly.

If g-waves excited to large amplitudes are present then nonlinear cooling effects could lead to instabilities which lead, in turn, to the observed optical filament systems. Such a scenario has also been suggested by Balbus & Soker (1989b) who look at g-wave excitation in the vicinity of the resonance. We then expect to see extended filament systems in clusters in which the central galaxy is not at rest relative to the cluster gas. A1795 could be one example of this phenomenon at work.

3.7 Damping of Oscillations

Acoustic oscillations are conductively damped by a factor

$$\Gamma = -\frac{(\gamma-1)^2}{2}\frac{\kappa_{Sp}}{P}k^2T^{7/2}. \tag{3.78}$$

The damping time t_d (a time dependence of e^{-t/t_d}) is $2/\Gamma$

$$\begin{aligned} t_d &= 6\times10^{-33}\lambda^2 n_e T_8^{-5/2} \\ &= 180\lambda_{kpc}^2 n_{-3} T_8^{-5/2}\,\mathrm{yr} \end{aligned} \tag{3.79}$$

where a 10% Helium density by number has been assumed. λ_{kpc} is the wavelength in kpc, n_{-3} is the electron density in $10^{-3}\,\mathrm{cm}^{-3}$ and T_8 is the temperature in 10^8 K. For waves travelling at the sound speed c this leads to a damping length of

$$L_d = 2.77\times10^{-4} n_{-3}\lambda_{kpc}^2 T_8^{-2}\,\mathrm{kpc}. \tag{3.80}$$

If waves have L_d much greater than a core radius then they will not heat the core effectively. T rises and n_{-3} falls with increasing radius so that L_d is largest in the middle of a cooling flow cluster—heat is always deposited more effectively in the outside regions than at the centre. Indeed, there will always be some radius at which the waves will be critically damped and will cease to be oscillatory. At the centre of a cooling flow cluster we might have $T\sim10^7$ K and $n_e\sim10^{-2}\,\mathrm{cm}^{-3}$, so that

$$L_d \approx 0.277\lambda_{kpc}^2\,\mathrm{kpc}. \tag{3.81}$$

The wavelength of the sound waves considered in this Chapter are sufficiently long that conductive damping in the core is not an important process. In the cluster centre the character of the wave changes to a g-wave and the wavelength is shorter, so damping can become important. At large radii conductive damping is more efficient. Provided the temperature falls off slower than density (in a non-isothermal atmosphere the wavelength also changes with radius), the damping length decreases outwards. All outgoing waves eventually come to a radius at which they are damped.

Waves may be also be generated in the turbulent wakes of galaxies on scales of $\sim 10\,\mathrm{kpc}$ (Jaffe 1977; Roland 1981) which gives $L_d \sim 25\,\mathrm{kpc}$. Such waves will be damped before leaving the core. Waves of wavelength 4 kpc or shorter will be critically damped. Waves of wavelengths greater than 20 kpc will lose some energy in the core but will be able to reach to outside a core radius. If waves are generated at large radii they will be unable to reach the core unless conductivity is suppressed.

Interesting consequences for stability follow from equation (3.80). Because of the strong variation in thermal conductivity with temperature, $L_d \sim T^{-3}$ at constant pressure. Therefore, hot gas subjected to a barrage of sound waves will be unstable—a slightly hotter region of gas will have a shorter damping length and will be heated more than a cooler region, exaggerating the initial difference.

The effect of the magnetic field in creating inhomogeneities (see Chapter 5) also leads to the focussing of the waves along field lines, because field lines define lines of constant (or nearly so) propagation velocity (equivalent to refractive index). In the same way that heat finds it difficult to flow because of the circuitous route it has to follow, waves generated at one point in the cluster will follow the field lines and are damped by an amount corresponding to the distance they have travelled along a field line. Therefore, the distance they can travel in real space is even more severely reduced. Note, though, that they will be preferentially focussed into the cooler, denser phase where the damping length is longest, countering this effect.

Magnetic suppression of conductivity alters the effective conductivity. In the presence of a magnetic field the conductivity is not scale independent (see Chapter 5). The scale on which conductivity should be evaluated is the wavelength of the wave, as this determines the scale of the temperature gradient. Conductive damping then depends more strongly on wavelength. If the wavelength of the waves is short compared to the scale length of the magnetic field and long compared to the electron mean free path then the damping is reduced by a factor of 1/3 to allow for the

varying orientations of the field relative to the direction of wave propagation.

Another factor to be taken into account is the fact that the coulomb mean free path of the electrons that conduct heat is long, typically 10 kpc. Thermal conductivity on scales smaller than or similar to the mean free path is reduced.

The above considerations imply that, if we start from an initial state in which sound waves are found everywhere, they will soon be found concentrated in the cooler, denser phase, for two reasons (i) the focussing effect (ii) those that are not focussed will be more quickly damped.

For g-waves the conductive damping time is the same as above, but the damping length is much shorter because the group velocity of these modes is rather small. In addition, the wavelength of g-waves decreases inwards, so that conductive damping becomes more effective at small radii. Much of the energy is likely to be deposited where it is generated, rather than propagating to other parts of the cluster. Note that in this case the channeling or focussing into the denser phase will not occur as much as for sound waves, if at all.

3.8 Discussion

We can conclude that oscillating central galaxies lose a large amount of energy in the form of sound waves. This energy is, however, insufficient in itself to make a major contribution to the energy balance of the X-ray emitting gas, and does not lead to much damping of the galaxy's motion. This result agrees with that of Binney (1988), who found that emission of p-waves over a Hubble time by a rotating triaxial galaxy was only a small drain on the galaxy's energy resources.

The evaluation of energy loss is only approximate due to the use of the Green's function for a homogeneous gas. The true Green's function will differ substantially

from this wherever the Brunt-Väsäilä frequency is not small compared to the frequency of the wave we are considering. I have argued that the approximation is acceptable because the size of the region where the Green's function is in error is small compared to a wavelength.

The radiative damping length (damping time times sound speed) for sound waves is long, and the wavelengths of the p-waves excited are sufficiently long that conductive damping is not efficient. The waves, once they escape from the g-wave zone right at the centre of the cluster, can propagate to large radii.

Conductive damping is important for shorter wavelength waves. Because conductive damping is more efficient in hotter gas, hot gas is preferentially heated. A barrage of sound waves in cluster gas drives an instability.

The oscillations excited by cluster galaxies (especially central galaxies) can reach nonlinear amplitudes in the central regions of cooling flows. Nonlinear effects could then produce the structures seen as optical filaments. The presence of a strong optical filament system around the cD galaxy in A1795, which is known to be moving relative to the cluster, supports this view.

Chapter 4. Faraday Rotation and Cluster Radio Sources

Although magnetic fields are known to be an important component of the intracluster medium (Tribble 1989b; and Chapter 5), their properties are not well known. The aims of this Chapter are to review the arguments regarding the existence of magnetic fields in the intracluster medium, and to use the radio source Cygnus A in an attempt to derive the properties of the field. Section 4.1 discusses Faraday rotation due to the intracluster magnetic field. Section 4.2 considers how this can be used to measure magnetic field properties. In Section 4.3 the analysis of the rotation measure of Cygnus A is presented. In Section 4.4 the depolarization of double radio sources is shown to be consistent with the results derived for Cygnus A.

4.1 Faraday Rotation

Radio waves from extragalactic (and, of course, other) radio sources are due to synchrotron emission from relativistic electrons spiralling in a magnetic field, and the emission is thus highly polarized (see Saikia & Salter 1988 and Radhakrishnan 1989). This is not always evident from low resolution observations as the direction of the electric vector defining the polarization is not constant over a resolution element. When observed at sufficiently high resolution, a very high degree (up to 70%) of polarization is seen.

Material intervening between the places of emission and observation alters the polarization properties of the waves. One major effect that is of interest in this Chapter is that of Faraday rotation. When polarized radio emission of wavelength λ passes through a magnetized plasma the Faraday effect rotates the plane of polarization through an angle

$$\Delta\theta = \mathrm{RM}\,\lambda^2, \tag{4.1}$$

where the rotation measure (RM) is

$$\mathrm{RM} = 810 \int (1+z_c)^{-2} n_e \mathbf{B}.d\mathbf{l}. \tag{4.2}$$

Here n_e is the electron density in cm^{-3}, $\mathbf{B}$ is the magnetic field in μG and $\mathbf{l}$ the path length in kpc. The factor $(1+z_c)^{-2}$ where z_c is the redshift of the intervening material allows for the fact that the wavelength where rotation occurs differs from that observed.

To find the RM for a source, the position angle of the electric vector of the radiation is measured at a range of wavelengths. A relation of the form (4.1) is assumed and used to derive the RM. The position angles are ambiguous by $\pm n\pi$ which makes it difficult to determine the RM uniquely (see Ruzmaikin & Sokoloff 1979).

Having measured the RM for a source, we then wish to deduce the properties of the medium causing the rotation, through equation (4.2). Of particular interest is the intracluster medium, where the density n_e is known from X-ray observations.

Unfortunately, every point along the line of sight contributes to the integral so that isolating the precise location of the Faraday medium will be difficult. If the source is in or behind a cluster of galaxies the contributions to the RM are,

$$\mathrm{RM} = \mathrm{RM}_{int} + \mathrm{RM}_{cl} + \mathrm{RM}_{ig} + \mathrm{RM}_{gal}. \tag{4.3}$$

The contributing factors are, respectively,

(i) The internal structure of the radio source. In other words, material mixed in with the radio emitting plasma. This leads to differential rotation from front to back of the emitting region, and thus to depolarization. Observations of very high percentage polarization imply that this effect is unimportant. In general, this is not well understood, although the polarization properties can be used

to give some clues as to the internal structure (Burn 1966; see also Cioffi & Jones 1980 and Laing 1981).

(ii) The intracluster medium. In the related case of elliptical galaxies with hot coronae and possible cooling flows this would correspond to the hot ISM (Forman, Jones & Tucker 1985; Thomas *et al.* 1986).

(iii) Intergalactic and intercluster space. Some authors claim (on the basis of RM measurements) that there is a large scale metagalactic magnetic field (Andreasyan 1986). Vallée (1989) found a mean RM of 0 ± 4 for radio sources in the direction of the great attractor, implying a mean uniform line of sight magnetic field of less than $0.1\,\mu$G.

(iv) Our own galaxy. This is becoming well understood, with a well defined galactic RM distribution (Simard-Normandin & Kronberg 1980).

For an individual source separating the above components is difficult. Kronberg & Simard-Normandin (1976) noted that the distribution of RM's of extragalactic radio sources split into two classes: a large number of sources have small RM's, and there is in addition a group of sources distributed over a much larger range of RM. A natural interpretation of this result is that the first class of sources have an RM due solely to the galaxy, whereas the second class of sources have some extra intrinsic contribution.

Lawler & Dennison (1982) split radio sources into two samples, one with lines of sight passing through clusters and one with lines of sight that didn't pass through clusters, and attributed a statistical difference in the RM distributions of the two samples to a cluster contribution. Vallée, Macleod & Broten (1986) looked at ten sources behind or near the cluster A2319 and discovered an excess RM for those sources with lines of sight nearest the cluster centre. Kim *et al.* (1987,1989) found a similar result for the Coma cluster (see figures 4.1 and 4.2). In these cases n_e and

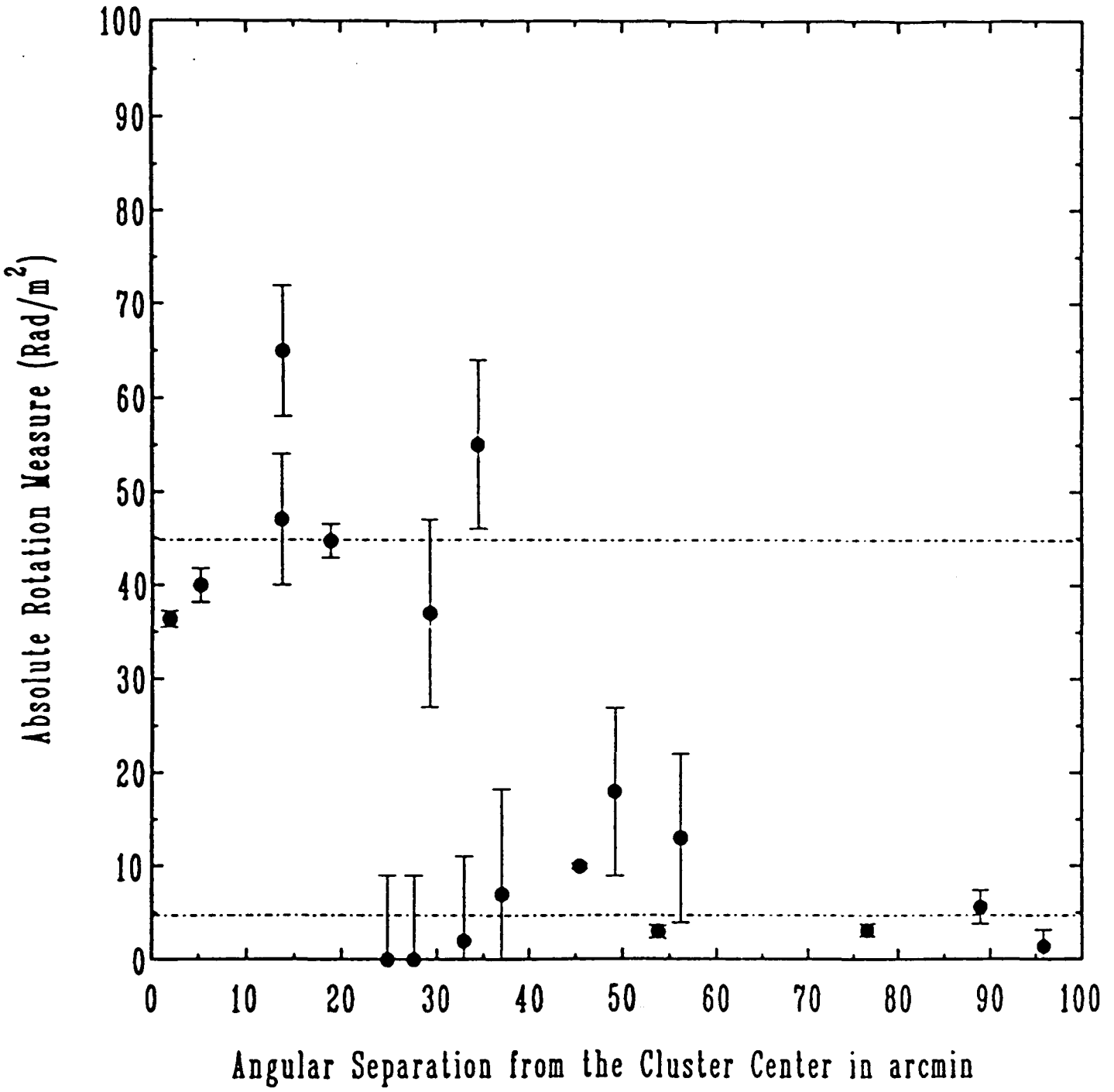

Figure 4.1. The magnitude of the Rotation Measures of sources in or behind the Coma cluster of galaxies plotted against distance from the cluster centre. A clear excess RM toward the cluster centre is seen. (From Kim *et al.* 1987.)

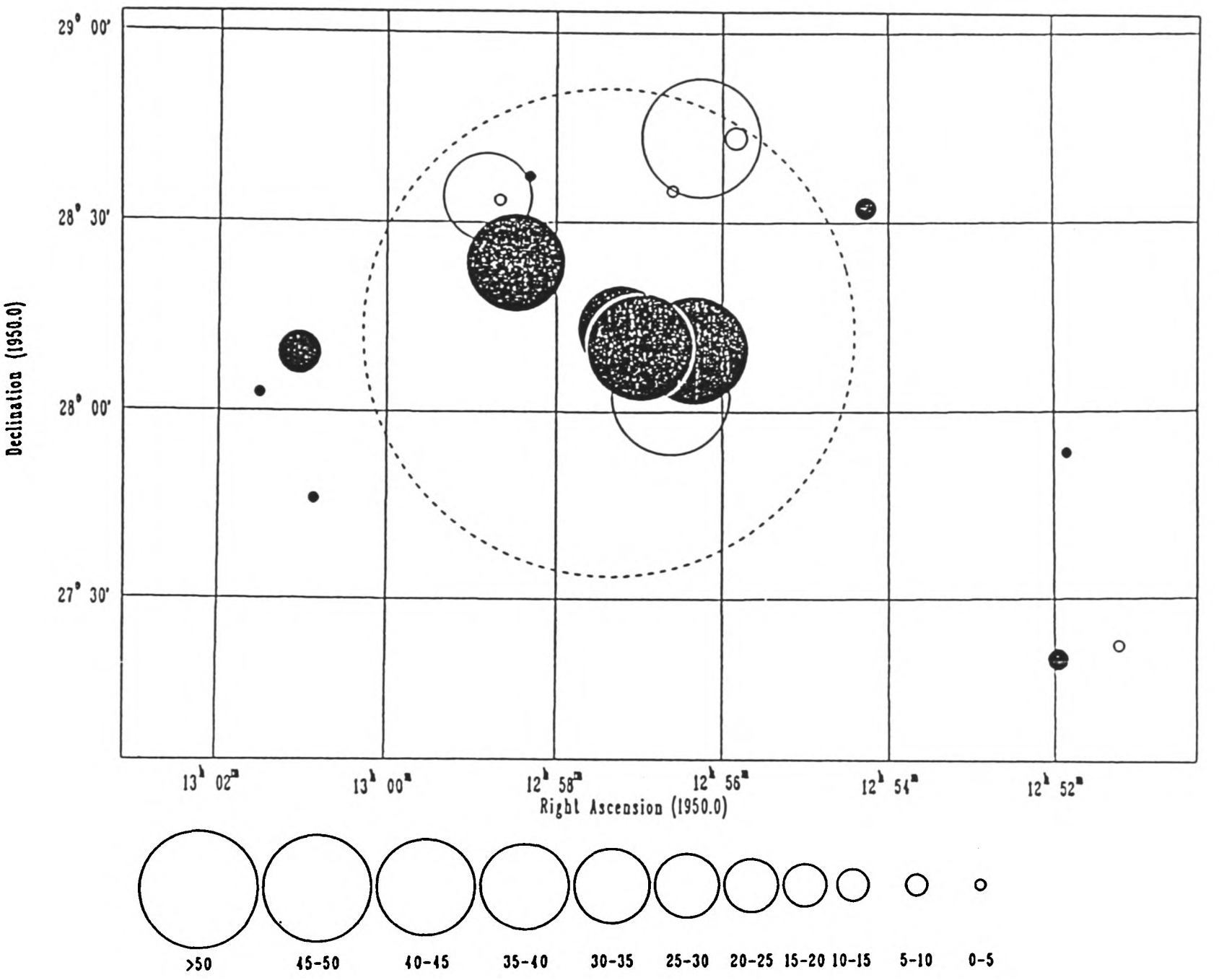

Figure 4.2. The rotation measures of the sources in the previous plot plotted against position. Filled circles are positive values, and unfilled circles are negative. The dashed circle is at one Abell radius. (From Kim *et al.* 1989.)

l can be estimated from X-ray data. The derived field strengths are small: Lawler & Dennison infer a mean line of sight magnetic field strength of $0.07\,\mu$G.

In clusters with radio halos a lower limit can be derived for the magnetic field. The luminosity of the radio halo depends on both the density of relativistic electrons and the magnetic field. The electrons responsible for the radio emission will also cause inverse Compton emission of X-rays. The observed X-rays are predominantly thermal so we have an upper limit on the contribution of inverse Compton emission (proportional to the number of relativistic electrons) and thus a lower limit on the magnetic field (Rephaeli & Gruber 1988). This limit is generally greater then that inferred from the Faraday rotation observations, which give the mean line of sight field. The magnetic field must therefore be reversed (perhaps many times) along the line of sight, implying that the magnetic field is tangled. The actual field strength could then be a few μG.

In a recent larger survey, Kim & Kronberg (1989) have obtained RM values for 157 radio sources near 51 clusters of galaxies. These are plotted against projected Abell radius in Fig. 4.3. Note the clear widening of the envelope at small projected radii. This provides convincing evidence for the presence of magnetic fields in clusters of galaxies.

4.1.1 RESOLVED SOURCES

Early Faraday rotation measurements were unable to resolve radio sources so the measured RM value was the real RM integrated (weighted by polarized intensity) over the source. Because different parts of the source have different initial polarization angles and different lines of sight have different RM values, depolarization and a breakdown of the linearity of equation (4.1) will generally occur.

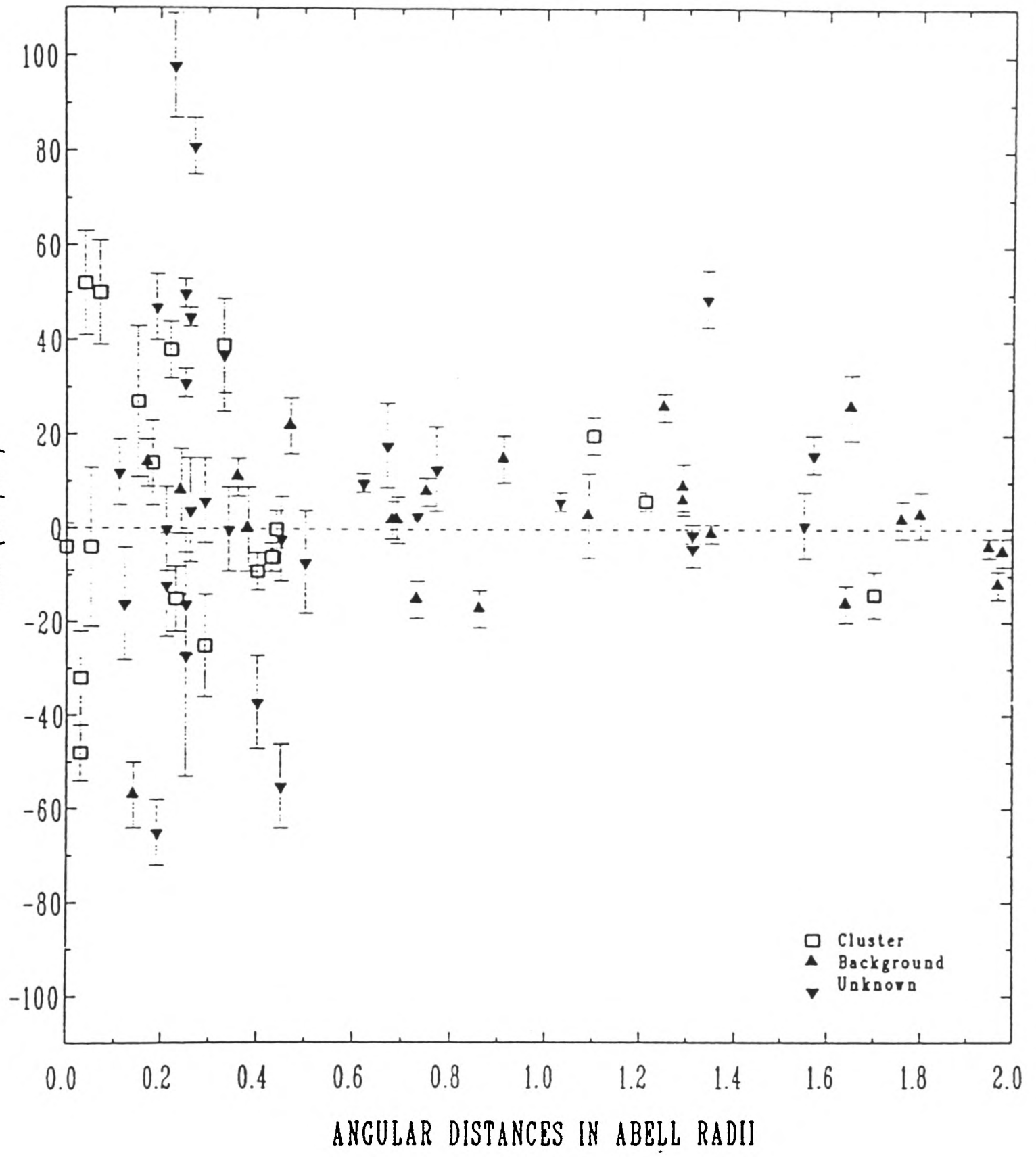

Figure 4.3. The Rotation Measures of 157 sources obtained by Kim & Kronberg (1989) plotted against projected Abell radius. Note the clear rise towards the central regions of clusters. Sources known to be within clusters are denoted by open squares, those known to be behind clusters by upward triangles, and those whose location along the line of sight is unknown by downward triangles. The sources within the cluster sample only a fraction (half on average) of the cluster Faraday depth.

Radio measurements can now resolve the Faraday rotation structure of extended sources. Such observations have been reported by De Young, Hogg & Wilkes (1979); Perley, Bridle & Willis (1984); Leahy (1984); Patnaik, Malkan & Salter (1986); O'Dea & Owen (1986, 1987); Leahy, Jägers & Pooley (1986); Leahy, Pooley & Riley (1986); Killeen, Bicknell & Ekers (1986); Dreher, Carilli & Perley (1987); Laing & Bridle (1987); and Pedelty *et al.* (1989). These maps of RM against position obviously contain substantially more information than unresolved measurements.

The most striking example of a resolved RM measurement yet published is that of Cygnus A (Dreher, Carilli & Perley 1987). Cygnus A is unusual in being a classical double source at the centre of a cooling flow cluster, and is an extreme example of the variations in RM that can be seen across radio sources. Other sources have RM's typically an order of magnitude less. The extreme nature of Cygnus A can be turned to advantage because it is difficult to produce such large RM's or RM gradients. Dreher, Carilli & Perley argue that in particular contributions (i), (iii) and (iv) to equation (4.3) are insufficient to produce such large RM's. There is, in general, no correlation of RM with the morphology of the radio source [except for the observation of the bow shock in the western lobe (Carilli, Perley & Dreher 1988)], and no significant depolarization, arguing against an internal origin. All sources are subject to (iii) and (iv), but very few have an RM like Cygnus A, so that the RM is probably associated with Cygnus A itself. It is possible that the line of sight through our galaxy to Cygnus A passes through a very unusual region, but this is unlikely. Having ruled out an internal origin the majority of the RM must be due to the intracluster medium in the Cygnus A cluster.

An alternative model has been suggested by Bicknell, Cameron & Gingold (1989). They claim to be able to correlate the RM variations with wiggles in the brightness contours that they interpret as nonlinear Kelvin-Helmholtz instabilities in the backflow from the hotspots. This model suffers from many defects, principally

that projection effects have not been included. In order to see variations along the lobes the field should be aligned with the jet axis. If this is the case then the amplitude of the RM variations should be largest at the centre of the lobes. It is not. In addition the model fails to explain the asymmetry between the east and west lobes.

One might argue that (ii) is also insufficient to produce the observed RM because no other similar sources are seen. This argument is false because Cygnus A is sampling the very centre of a cooling flow, where the density and magnetic field strength are expected to be higher than at larger radii or in clusters of galaxies without cooling flows. Indeed, other central cluster sources (such as 3C295 and Hydra A, Perley 1989) also show extremely large RM's.

Other resolved sources have smaller RM's because they are in the outlying regions of clusters, or are not in clusters of galaxies at all. In such cases it is probable that part of the observed RM is due to the cluster, but it is difficult to establish the exact proportion of the RM due to the various contributions. The use of depolarization measurements of double radio sources will be considered further in Section 4.4.

Even a cursory examination of the RM map of Cygnus A indicates that there are considerable variations of RM. No obvious pattern is discernible although the RM variations are smooth everywhere. The RM appears to change on a scale of 5-10 arcsec or 5-10kpc. Allowing for the effect of foreshortening we would therefore expect structure in the intracluster magnetic field on scales $\approx$10kpc.

4.2 Properties of the RM distribution

The RM distribution can be described statistically using the RM autocorrelation

function $\xi(s)$ defined as

$$\xi(s) = \langle \mathrm{RM}(\mathbf{x})\mathrm{RM}(\mathbf{x}+\mathbf{s}) \rangle. \tag{4.4}$$

In equation (4.4) $\mathbf{x}$ represents coordinates on the sky and $\mathbf{s}$ is the difference between the coordinates of two points. The brackets $\langle \ldots \rangle$ represent averaging over all $\mathbf{x}$ and all directions of $\mathbf{s}$. The function $\xi(s)$ is thus a measure of the mean correlation of the RM at two points a distance $s = |\mathbf{s}|$ apart. The distance at which ξ falls appreciably from its maximum value defines a length over which the RM is well correlated. In practice observations are at discrete points and one sums over all pairs of points separated by s.

By analogy with equation (4.4) we can define n-point autocorrelation functions by taking the $\langle \ldots \rangle$ of the product of the RM at n different points—the whole infinite hierarchy of such functions is needed for a complete statistical description of the RM distribution. Knowledge of $\xi(s)$ alone may not be sufficient to differentiate between competing models of the magnetic field in the intracluster medium although, as shown below, limited information can be gained.

4.2.1 TURBULENT MAGNETIC FIELDS

Radio sources are distant and of small angular size, so that all lines of sight through the cluster are approximately parallel. I assume the magnetic field to be turbulent, homogeneous and isotropic, and variations in density and magnetic field are assumed to be independent. These approximations are valid provided the scale on which the turbulence is not homogeneous and isotropic is much larger than the correlation length of the field. The magnetic field is analogous to the velocity in an incompressible fluid, so the treatment of turbulence in an incompressible, isotropic, homogeneous fluid in Batchelor (1953) can now be used: I follow his notation in what follows.

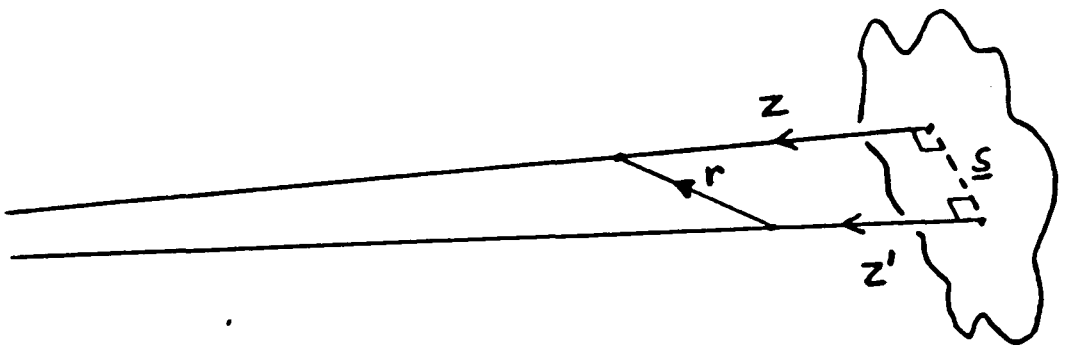

Figure 4.4. The coordinate system used in the text.

The situation is portrayed in Fig. 4.4. The autocorrelation function is

$$\xi(s) = \langle 810^2 \iint dz dz' (1+z_c)^{-2}(1+z_c')^{-2} n_e(z) n_e(z') B_z(\mathbf{x}, z) B_z(\mathbf{x}+\mathbf{s}, z') \rangle. \quad (4.5)$$

For a localized source such as a cluster of galaxies $z_c = z_c'$ and can be taken outside the integral. The $\langle \ldots \rangle$ can be taken inside the integral and applied to the magnetic field only to give

$$\xi(s) = 810^2 (1+z_c)^{-4} \iint dz dz' n_e(z) n_e(z') \langle B_z(\mathbf{x}, z) B_z(\mathbf{x}+\mathbf{s}, z') \rangle \quad (4.6)$$

where the magnetic field autocorrelation function is $\langle B_z(\mathbf{x}, z) B_z(\mathbf{x}+\mathbf{s}, z') \rangle \equiv R_{zz}$. R_{ij} is an isotropic second order tensor and may be written in the form

$$R_{ij}(\mathbf{r}) = A(r) r_i r_j + B(r) \delta_{ij}, \quad (4.7)$$

where $r^2 = s^2 + (z - z')^2$ and A and B are even functions of r. It is convenient to introduce normalized longitudinal and lateral correlation functions f and g, in terms of which,

$$R_{ij}(\mathbf{r}) = \frac{\langle B^2 \rangle}{3} \left(\frac{f-g}{r^2} r_i r_j + g \delta_{ij} \right). \quad (4.8)$$

The constraint $\nabla . \mathbf{B} = 0$ implies that $g = f + rf'/2$. R_{zz} may therefore be written as

$$R_{zz}(s, z - z') = \frac{\langle B^2 \rangle}{3} (f + \frac{s^2}{2r} \frac{df}{dr}). \quad (4.9)$$

This is as far as I can go without knowing the form of f. The normalization implies that $f(0) = 1$. Given this, there remains a lot of freedom in the choice of

f. For no better reason than it being analytically convenient, I use a gaussian as an illustration,

$$f = e^{-r^2/2r_0^2}, \tag{4.10}$$

which leads to

$$\xi(s) = \frac{810^2}{3}(1+z_c)^{-4} \iint dz dz' e^{-s^2/2r_0^2} \left(1 - \frac{s^2}{2r_0^2}\right) \langle B^2 \rangle n_e(z) n_e(z') e^{-(z-z')^2/2r_0^2}. \tag{4.11}$$

If $\langle B^2 \rangle$ and f are independent of radius then for small r_0 the gaussian in the integral approximates a Dirac delta function that can be integrated out to give

$$\xi(s) = e^{-s^2/2r_0^2} \left(1 - \frac{s^2}{2r_0^2}\right) \frac{810^2 \langle B^2 \rangle r_0 \sqrt{2\pi}}{3} (1+z_c)^{-4} \int dz\, n_e^2(z). \tag{4.12}$$

In the general case we need to know $n_e(z)$ in order to do the integral. The value of the integral is often given directly by the X-ray measurements from the *Einstein observatory* satellite, because at the temperatures typical of the intracluster medium the response of the detectors is dependent only on the integral and only weakly dependent on temperature. There may be no need to deproject the X-ray emission to give the density profile. This is unfortunately not so at the centre of a cooling flow, which is the most interesting case.

If $\langle B^2 \rangle$ and f are functions of r then integrating as before gives

$$\xi(s) = \sqrt{2\pi}\, \frac{810^2}{3}(1+z_c)^{-4} \int dz\, n_e^2(z)\, \langle B^2 \rangle(r)\, r_0(r)\, e^{-s^2/2r_0^2(r)} \left[1 - \frac{s^2}{2r_0^2(r)}\right]. \tag{4.13}$$

When $s = 0$, $\langle \mathrm{RM}^2 \rangle$ is given as a function of projected radius R,

$$\langle \mathrm{RM}^2 \rangle = \frac{\sqrt{2\pi}\, 810^2}{3}(1+z_c)^{-4} \int dz\, r_0(R,z) n_e^2(R,z) \langle B^2 \rangle(R,z). \tag{4.14}$$

Assuming that the density, magnetic field strength and scale length vary as power laws in radius, so that $n_e = n_0 r^{-\alpha}$, $B = B_0 r^{-\beta}$, and $r_0 = \epsilon r^{\delta}$, gives

$$\langle \mathrm{RM}^2 \rangle = \frac{\sqrt{2\pi}\, 810^2}{3}(1+z_c)^{-4} \epsilon B_0^2 n_0^2 R^{-2\alpha-2\beta+\delta+1} \int dx\, (1+x^2)^{-\alpha-\beta+\delta/2} \tag{4.15}$$

where $x = z/R$. Equation (4.15) is the main result of this Section and will be used later in the analysis of data from Cygnus A. The above procedure does not depend on the choice of f—any function forming a δ-sequence will give the same result, to within a constant factor of order unity.

Equations (4.12) and (4.15) allow some comments regarding RM distributions to be made.

(i) RM structure will be amplified as it passes through the intracluster medium. It will not be washed out by passing through many field scale lengths in the intracluster medium, as claimed by O'Dea & Owen (1987). In the case of Cygnus A (Dreher, Carilli & Perley 1987) regions of high RM are correlated with regions of high X-ray emission, namely those nearest the centre. This effect is also seen in the Coma cluster (Kim *et al.* 1987; see Figures 4.1 and 4.2), and in A2319 (Vallée, Macleod & Broten 1986).

(ii) The r.m.s. value of RM is determined by $\langle B^2 \rangle$ and r_0. If we measure $\langle \mathrm{RM}^2 \rangle$ and can estimate the scale length r_0 we thus have a fairly good estimate of the magnetic field strength. The most difficult step is measuring the scale length of the field.

(iii) Given that a large part of the RM is intrinsic, the use of RM measurements of double radio sources such as Cygnus A to map the small scale structure of the Galactic RM (Simonetti, Cordes & Spangler 1984; Simonetti & Cordes 1986; Leahy 1987) is questionable. Although sources with obvious (i.e. absurdly large) intrinsic RM are excluded in these analyses, all sources would be expected to have some intrinsic RM.

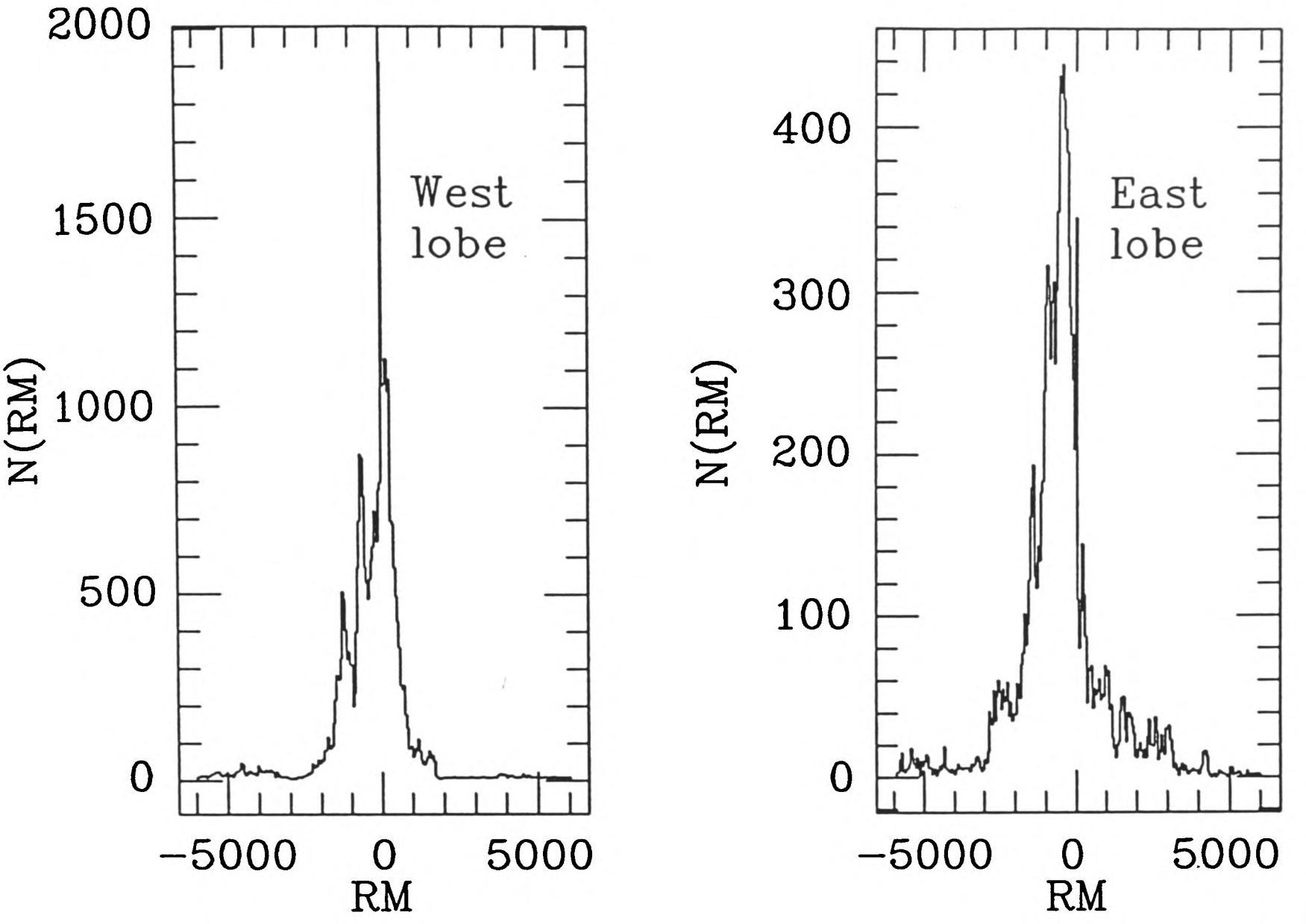

Figure 4.5. Histograms of observed RM for the two lobes of Cygnus A.

4.3 Analysis of Cygnus A

Fig. 4.5 shows histograms of the RM distributions in the two lobes, with their properties in Table 4.1. As expected, the western lobe, on the jet side, which is nearer to us and has a smaller path length through the intracluster medium, has a smaller RM dispersion (see Section 4.6 for further discussion of the front/back asymmetry in radio sources).

The average RM^2, in radial bins, is shown in Fig. 4.6. The large variations in Fig. 4.6 are due to poor sampling of the underlying RM distribution—although there are many field scale lengths along the line of sight, only a very few scale lengths in the plane of the sky are sampled. If data were available over a greater range of radii for the eastern lobe it too would show the rise in RM towards the

Table 4.1. The mean RM, mean square RM, RM dispersion and number of data points for the two lobes separately and for the source as a whole.

	$\overline{\mathrm{RM}}$	$\overline{\mathrm{RM}^2}$	σ_{RM}	N
Eastern Lobe	−500	2986000	1650	14421
Western Lobe	−380	1295000	1070	30816
Whole Source	−420	1834000	1290	45237

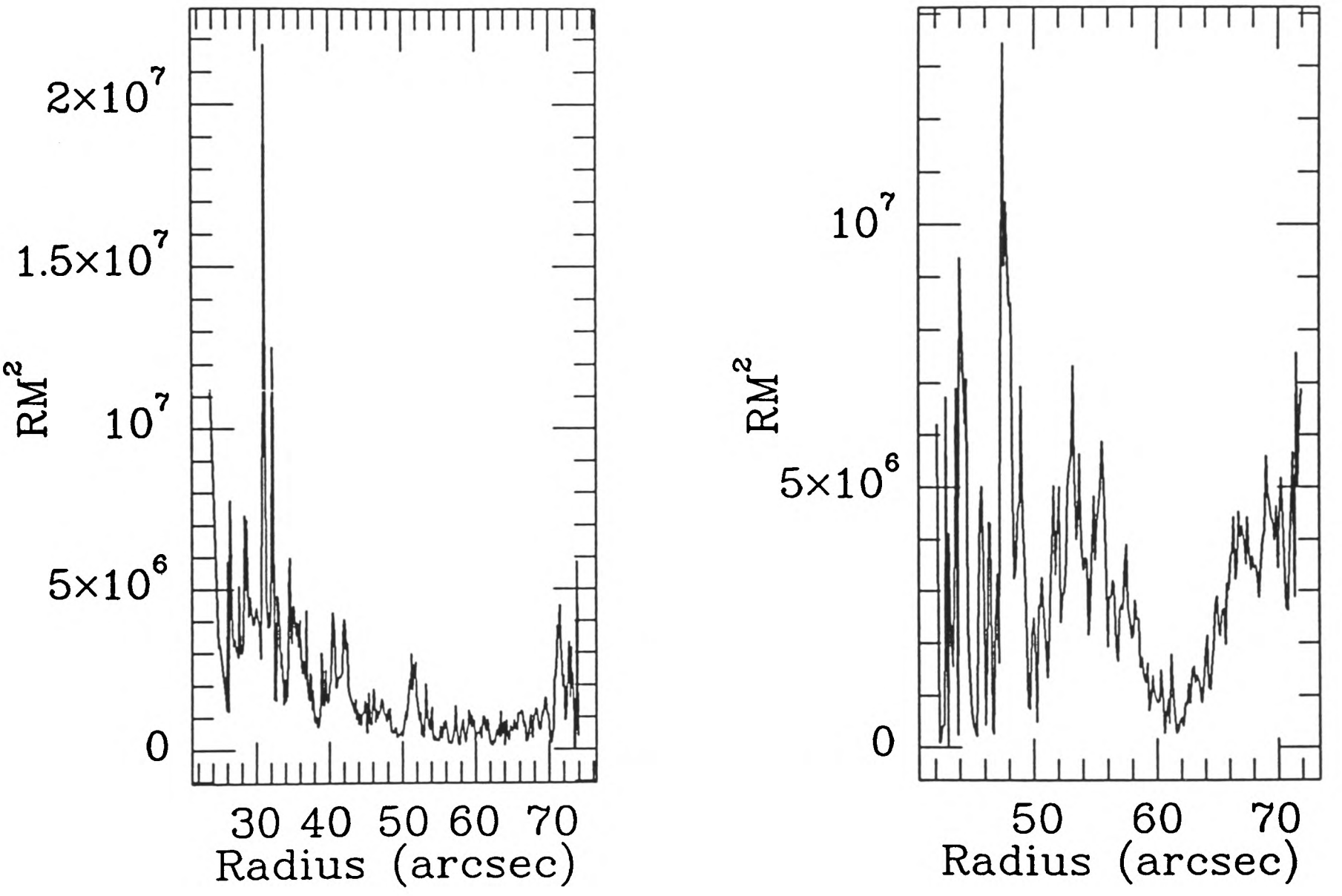

Figure 4.6. RM^2 binned by radius for the western and eastern lobes.

centre seen in the western lobe, but the high RM causes sufficient depolarization to make it unmeasurable. Because of this I only analyze the western lobe.

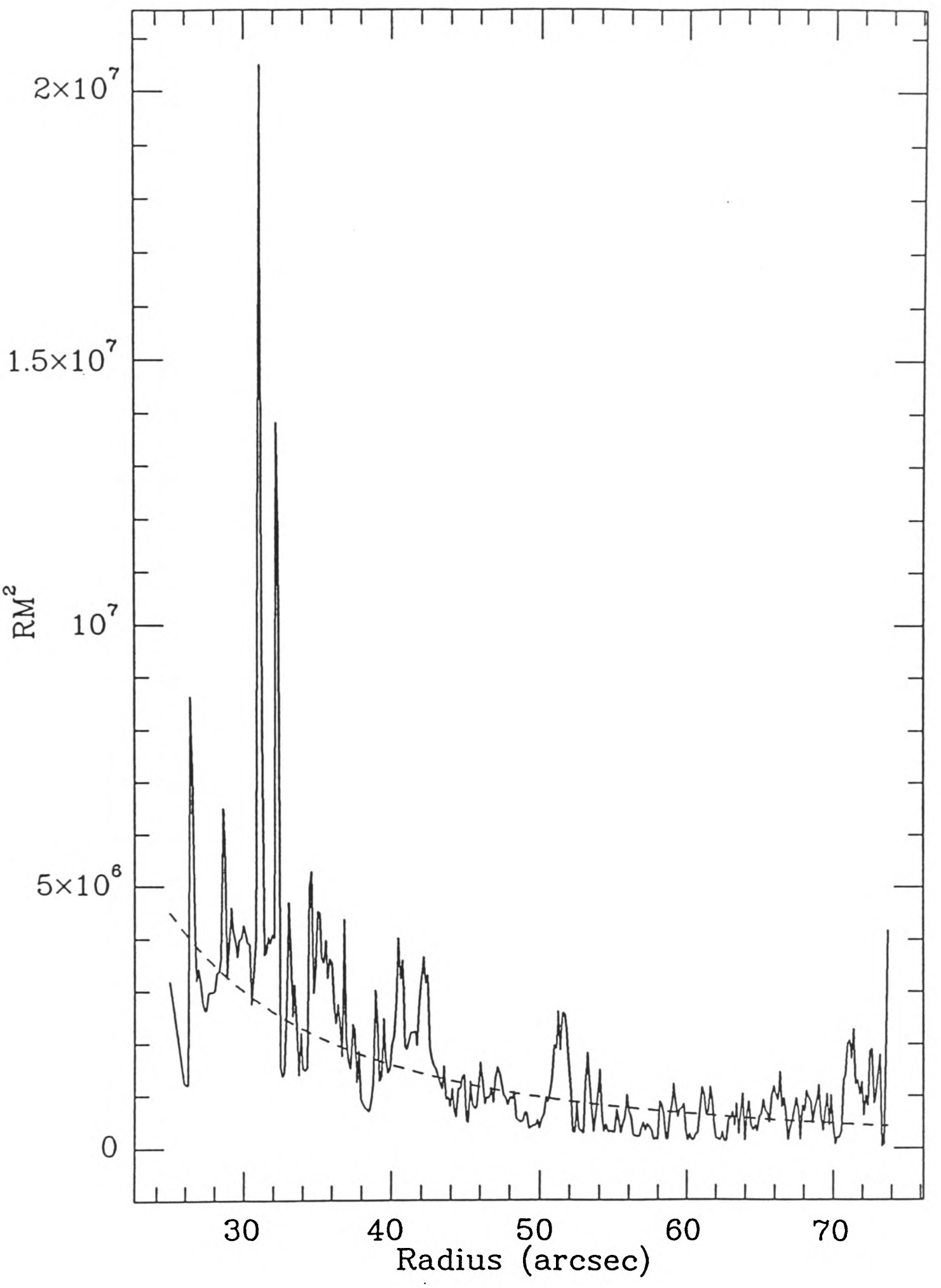

Figure 4.7. RM^2 against radius for the western lobe. Isolated pixels (those with less than four neighbours) have been removed. In addition, the region of the bowshock found by Carilli, Perley & Dreher (1988) and the region of high RM to the northwest of the bowshock but outside the lobe have been removed. The dashed line is a best fit power law to the variation of RM^2.

The RM^2 distribution also contains features that are not due to general intracluster gas. One of these is a feature interpreted as the radio-quiet bowshock by Carilli, Perley & Dreher (1988). This can be seen in Fig. 4.6 as a rise in RM^2 at large radii. There is also a region of large RM just northwest of the bowshock which lies outside the radio lobes. Such isolated features are unwelcome when we are trying to fit the cluster contribution to the RM. Before the fitting was done, both these regions were removed from the data, and isolated pixels (those with less than 4 neighbours) were also removed.

The result is shown in Fig. 4.7, which also shows a power law fit to the data for the western lobe,

$$\langle \mathrm{RM}^2 \rangle = 5 \times 10^9 h_{75}^{-2.2} R^{-2.2}, \tag{4.16}$$

where R is in kpc. This is to be compared with

$$\langle \mathrm{RM}^2 \rangle = \frac{\sqrt{2\pi} 810^2}{3} (1+z_c)^{-4} \epsilon B_0^2 n_0^2 R^{-2\alpha-2\beta+\delta+1} \int dx \, (1+x^2)^{-\alpha-\beta+\delta/2}. \tag{4.15}$$

If N is the coefficient of $1/R$ this can be written as

$$\langle \mathrm{RM}^2 \rangle = \frac{\sqrt{2\pi} 810^2}{3} (1+z_c)^{-4} \epsilon B_0^2 n_0^2 R^{-N} \int dx \, (1+x^2)^{-\frac{N+1}{2}}. \tag{4.17}$$

The integral is $B(1/2, N/2) = 2^{N-2}[\Gamma(N/2)]^2/\Gamma(N)$, and is only weakly dependent on N, being 0.94 for $N = 2.2$. Cygnus A has a redshift $z_c = 0.0567$ so that

$$\langle \mathrm{RM}^2 \rangle = 4.13 \times 10^5 \epsilon B_0^2 n_0^2 R^{-2.2}. \tag{4.18}$$

With $n_e = 0.6 R^{-1} h_{75}^{-1/2}$ (Arnaud *et al.* 1984),

$$\epsilon B_0^2 = 3.36 \times 10^4 h_{75}^{-1.2} \tag{4.19}$$

and

$$2\beta - \delta = 1.2.$$

4.3.1 FROZEN IN FIELDS

If the field is frozen into the gas then isotropic compression by the cooling flow implies that $B \sim n^{2/3}$ and $r_0 \sim n^{-1/3}$, with $B^2 r_0 \sim n$, as observed. Then $\beta \approx 2/3$ and $\delta \approx 1/3$. From the RM map $r_0 \sim 10\,\mathrm{kpc}$ at $50\,\mathrm{kpc}$, so that $r_0 \sim 2.7 r^{1/3}$. Therefore

$$B \sim 110/R^{2/3}, \tag{4.20}$$

implying a field strength of $8\,\mu$G at $50\,$kpc and $5\,\mu$G at $100\,$kpc. Although these values are high, the magnetic pressure is still less than one per cent of the thermal pressure ($P_{th}/P_{mag} \approx 100 T_8 R^{1/3}$). The field strength is also consistent with that required by Carilli, Perley & Dreher (1988) to explain the bowshock in the western lobe.

The field compression is not, however, expected to be isotropic. If all points flow radially then the tangential scale length is proportional to r and the radial field strength varies as $1/r^2$. In a flow with $\dot{m} \propto r$, the inflow velocity is constant. Then the radial scale length is constant, and the tangential field strength varies as $1/r$. The field in such a flow would become predominantly radial at small (compared to the cooling radius) radii. It then becomes possible for matter to flow along the field lines and compression of the field stops.

It is obvious that even assuming magnetic flux to be frozen into the gas, it is difficult to predict the variation of RM^2 with radius. In the isotropic case we find $B^2 r_0 \sim n$. In the more realistic non-isotropic case the field variation with radius is stronger. All that can be said is that the variation of RM^2 with radius is consistent with the magnetic field being frozen into a cooling flow.

We have seen that it is difficult to predict the variation of B and r_0 with radius. Is it possible to measure the scale length from the structure of the RM distribution? This is difficult. The major problem is simply lack of data. It is

difficult to estimate the scale length of the field when the data region is only a few scale-lengths across. Attempting to derive a radial variation is not a good idea. I have attempted to calculate the RM correlation function, but this approach was not successful, yielding no more information than a visual inspection of the RM maps.

4.4 Radio Source Depolarization

The RM distribution of Cygnus A is resolved. When there is unresolved RM structure this leads to depolarization of the radio emission (Burn 1966). This is also a useful probe of the physical properties of hot gaseous halos.

4.4.1 THEORY

The polarized emission from a point with sky coordinates $\mathbf{x}$ can be written in the form

$$p(\mathbf{x}) = \epsilon_\lambda(\mathbf{x}) e^{2i\theta(\mathbf{x})}. \tag{4.21}$$

Here ϵ_λ is the polarized intensity and θ the polarization angle at the point of emission. If we observe a source with an instrument which has an observing window (or beam) W then the fractional polarization, pol, is

$$pol(\mathbf{x}_0) = \frac{\int W(\mathbf{x}-\mathbf{x}_0)\epsilon_\lambda(\mathbf{x}) e^{2i\theta(\mathbf{x})}\, d^2\mathbf{x}}{\int W(\mathbf{x}-\mathbf{x}_0)\epsilon_\lambda(\mathbf{x})\, d^2\mathbf{x}}. \tag{4.22}$$

If the medium through which the radiation passes causes Faraday Rotation then

$$pol(\mathbf{x}_0) = \frac{\int W(\mathbf{x}-\mathbf{x}_0)\epsilon_\lambda(\mathbf{x}) e^{2i[\theta(\mathbf{x})+\mathrm{RM}(\mathbf{x})\lambda^2]}\, d^2\mathbf{x}}{\int W(\mathbf{x}-\mathbf{x}_0)\epsilon_\lambda(\mathbf{x})\, d^2\mathbf{x}}. \tag{4.23}$$

If the window W is much larger than the scale of the fluctuations in RM [Burn (1966) considered the case where the source was unresolved], then W samples the RM distribution. So, averaging over the RM distribution,

$$pol(\mathbf{x}_0) = \frac{\iint W(\mathbf{x}-\mathbf{x}_0)\epsilon_\lambda(\mathbf{x}) P(\mathrm{RM}) e^{2i[\theta(\mathbf{x})+\mathrm{RM}(\mathbf{x})\lambda^2]}\, d^2\mathbf{x}\, d\mathrm{RM}}{\int W(\mathbf{x}-\mathbf{x}_0)\epsilon_\lambda(\mathbf{x})\, d^2\mathbf{x}}. \tag{4.24}$$

If the RM is distributed as a gaussian with r.m.s. deviation σ, [this is reasonable for Cygnus A—a Kolmogorov-Smirnov test (K.-S. test; Press *et al.* 1986) gave probability 1 that the observed RM values are drawn from a gaussian distribution, and see also Chapter 6], then

$$P(\mathrm{RM}) = A \exp(-\mathrm{RM}^2/2\sigma^2), \tag{4.25}$$

and the integral over RM can be done by completing the square,

$$\langle pol(\mathbf{x}_0) \rangle = \exp(-2\sigma^2\lambda^4) \frac{\int W(\mathbf{x}-\mathbf{x}_0)\epsilon_\lambda(\mathbf{x}) e^{2i\theta(\mathbf{x})}\, d^2\mathbf{x}}{\int W(\mathbf{x}-\mathbf{x}_0)\epsilon_\lambda(\mathbf{x})\, d^2\mathbf{x}}. \tag{4.26}$$

The depolarization, D, is the ratio of the percentage polarizations at different wavelengths, so

$$D^{\lambda_1}_{\lambda_2} = \frac{\exp(-2\sigma^2\lambda_1^4)}{\exp(-2\sigma^2\lambda_2^4)} \frac{\int W(\mathbf{x}-\mathbf{x}_0)\epsilon_{\lambda_1}(\mathbf{x}) e^{2i\theta(\mathbf{x})} d^2\mathbf{x}}{\int W(\mathbf{x}-\mathbf{x}_0)\epsilon_{\lambda_2}(\mathbf{x}) e^{2i\theta(\mathbf{x})} d^2\mathbf{x}} \frac{\int W(\mathbf{x}-\mathbf{x}_0)\epsilon_{\lambda_2}(\mathbf{x})\, d^2\mathbf{x}}{\int W(\mathbf{x}-\mathbf{x}_0)\epsilon_{\lambda_1}(\mathbf{x})\, d^2\mathbf{x}}.$$

The variation of polarization with wavelength has three causes;

(i) An unresolved external Faraday screen.

(ii) The variation of the intrinsic properties ϵ and θ across the beam.

(iii) Internal differential Faraday Rotation.

The effect of (iii) will be neglected. In order to use the observed depolarization to study an external Faraday screen, we must be able to quantify the effect of (ii). This gives rise to no depolarization in the following circumstances:

(a) The source is spatially uniform.

(b) The source properties are drawn from a random distribution, the properties of the random distribution being independent of wavelength.

(c) The ratio of the polarized intensities at the two wavelengths is independent of position.

For synchrotron radiation from electrons with a power-law energy distribution the intrinsic degree of polarization depends only on the power-law index, not on frequency. The emitted power is a simple product of functions of frequency and position. Therefore condition (c) applies and we may assume that there is no depolarization due to (ii). So, considering only an external origin for the depolarization, we get

$$D_{\lambda_2}^{\lambda_1} = \exp[-2\sigma^2(\lambda_1^4 - \lambda_2^4)]. \tag{4.27}$$

Under our assumption that W is large, equation (4.27) may be used to investigate the variation of σ^2 with position in the host galaxy of the radio source.

4.4.2 APPLICATION TO DOUBLE RADIO SOURCES - UNRESOLVED

By unresolved, I mean that the depolarization is not known as a function of position but is known for each component of a double radio source. (If the source were fully resolved then only the truly internal depolarization would be seen. This would be fine for studying the internal structure of the lobes, but would make this section irrelevant. In addition, the full RM structure would have been resolved also.)

Garrington *et al.* (1988) and Laing (1988) studied a sample of quasars and showed that there is a strong depolarization asymmetry—the component on the jet side of the nucleus suffers less depolarization. This occurs naturally if the jet is due to relativistic beaming; the component on the jet side is then nearer to us and the path length through the depolarizing medium less.

If we have two point sources, such as the two hotspots or lobes of a double radio source, which is assumed to be at the centre of a gaseous halo such as a cooling flow

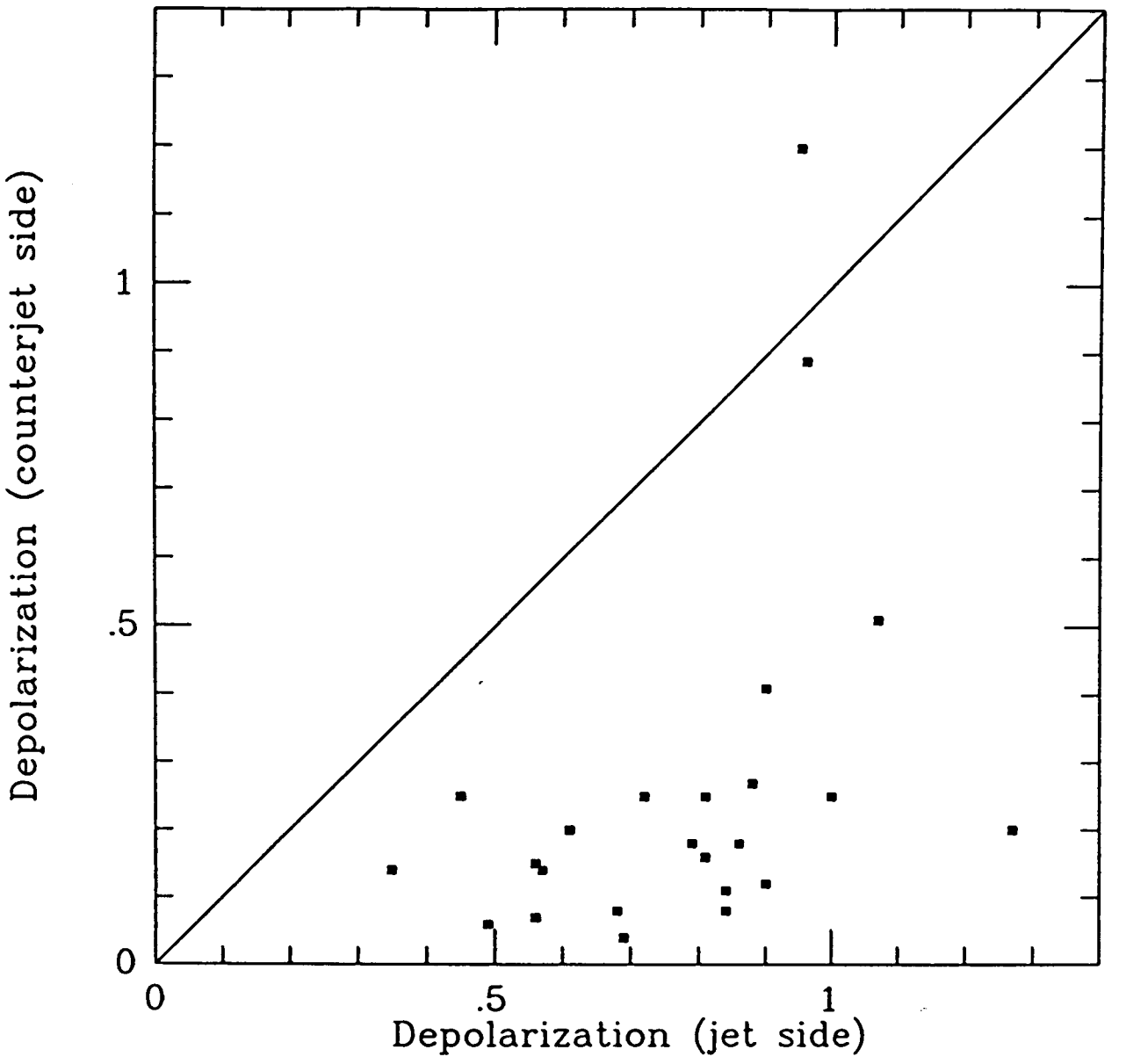

Figure 4.8. The depolarization data for 24 double sources studied by Garrington *et al.* (1988). The Jet side is considerably less depolarized.

(Crawford & Fabian 1989), then the depolarization ratios of the two lobes (where the subscript $_f$ refers to the front lobe, and $_b$ the back lobe) are

$$\begin{aligned} D_f &= \exp(-\alpha\sigma^2[\lambda_1^4 - \lambda_2^4]) \\ D_b &= \exp(-[1-\alpha]\sigma^2[\lambda_1^4 - \lambda_2^4]). \end{aligned} \tag{4.28}$$

In these expressions α is the fraction of the Faraday screen through which the near lobe is seen, which for a power-law distribution is

$$\alpha = \int_u^\infty dx \, \frac{1}{[1+x^2]^m} \Big/ \int_{-\infty}^\infty dx \, \frac{1}{[1+x^2]^m} \, , \tag{4.29}$$

where $m = \alpha + \beta - \delta/2$ and $u = z_0/s$ with $2z_0$ the difference in path length of the two components. The angle to the line of sight is $\theta = \arctan(s/z_0)$.

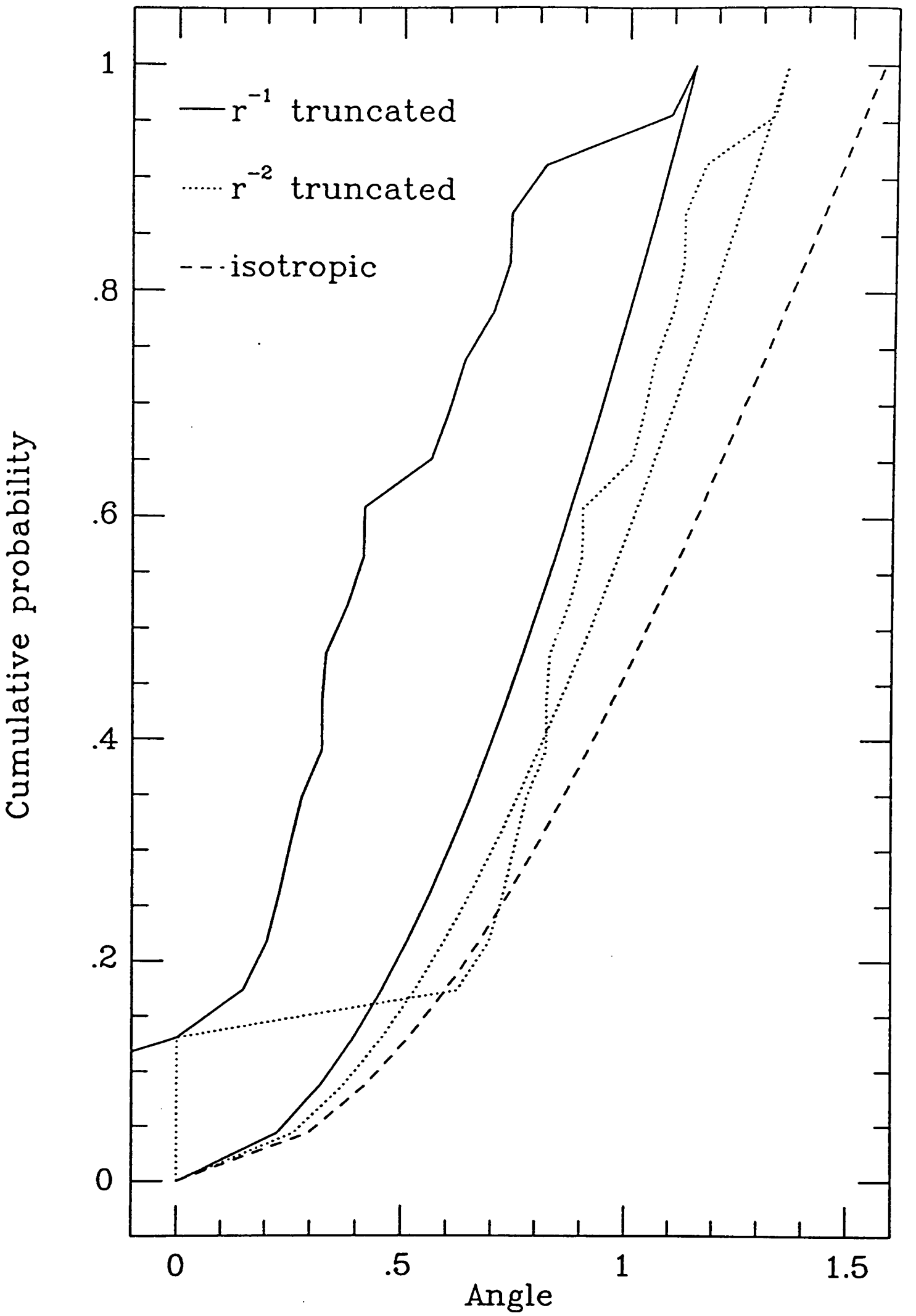

Figure 4.9. The cumulative distribution functions for the $m = 2$ case (dotted line) and the $m = 1$ case (full line). The expected distribution in angle for an isotropic distribution is shown as a dashed line.

So, given α and a model, we can calculate the angle of the radio source to the line of sight. To get α from the data we use the formula,

$$\alpha = \ln D_f / \ln(D_f D_b) \, . \tag{4.30}$$

The relationship between α and θ is, for $m = 1$,

$$\alpha = \theta / \pi . \tag{4.31}$$

With $m = 2$, as found for Cygnus A,

$$\alpha = \frac{1}{\pi} \left(\theta - \frac{\tan \theta}{1 + \tan^2 \theta} \right) , \tag{4.32}$$

which was inverted numerically to get the angles θ from the observed α's.

For these two models I have calculated angles to the line of sight for those radio sources given by Garrington *et al.* (1988). The distribution of these angles can then be compared against those expected if the radio sources are distributed isotropically in angle. A Kolmogorov-Smirnov (K.-S.) test (Press *et al.* 1986) shows that the $m = 1$ case is always a bad fit to the observed distribution. The $m = 2$ case is a passable fit (K.-S. probability 0.023) to an isotropic distribution. If the isotropic distribution is truncated at the largest derived angle to the line of sight then a very good fit to the distribution of angles is obtained. See Fig. 4.9 for details.

The success of this model suggests that halos similar to that around Cygnus A surround the quasars in the Garrington *et al.* sample. Note that, unlike Garrington (1988), I have used simple power laws to describe the Faraday medium. This is sensible because we know that cooling flows are well described by power laws. It should be seen as no coincidence that the derived RM properties for Cygnus A fit the depolarization data well.

The improved agreement when the angular range of the model is restricted is to be expected, as sources in the plane of the sky are selected against by the

requirement that a relativistically beamed jet be seen. The actual angle (nearly 80^o) to the line of sight is large. This tells us that quasars are distributed almost uniformly in angle, and may be an indication that quasars are not specially oriented cases of a more general class of object, which has implications for recent moves toward unified models (Barthel 1989).

4.5 Summary

Magnetic fields in the intracluster medium lead to Faraday rotation of polarized radio emission from radio sources with lines of sight that pass through the magnetized medium. The field in Cygnus A is tangled on scales $\sim 10\,\mathrm{kpc}$ and has a strength of several μG.

If the intracluster medium is responsible for the Faraday rotation, then the RM dispersion is correlated with X-ray surface brightness. Deviations from proportionality indicate variations in magnetic field strength and scale length and can in principle be used to measure these variations.

Cygnus A has been studied in detail. Sampling of the RM distribution in this source is poor, although much better than in most other sources. This is especially acute when the data are binned by radius, rendering the data from the eastern lobe unusable. The western lobe shows evidence for a smooth variation of $\langle \mathrm{RM}^2 \rangle$ with radius, and, when the variation due to the X-ray surface brightness has been taken into account, shows that $\langle B^2 \rangle r_0 \sim 1/r$. This is clear evidence for the variation of magnetic field properties with radius in a cluster.

The variation of $\langle B^2 \rangle r_0$ is consistent with the magnetic field being frozen into the cooling flow. Assuming the flux freezing to be isotropic, the magnetic field strength for Cygnus A varies like $r^{-2/3}$, being $8\,\mu$G at 50kpc.

The depolarization asymmetry found by Garrington *et al.* (1988) and Laing (1988) arises naturally if the radio sources observed are in similar environments to Cygnus A. These sources are consistent with the jet angles being distributed isotropically, with a lack of sources in the plane of the sky being probably a selection effect.

What then of the RM's of other sources? The derived magnetic field strength for Cygnus A may be higher than in other clusters. The variation with radius may well be typical. Therefore one should look at small (and therefore young) sources which are close to the cluster centre in order to see such clear effects. Such sources should show large RM's if intracluster magnetic fields similar to those in Cygnus A are common. Recent observations of such sources (3C295 and Hydra A) have indeed shown this to be the case.

It is of course intriguing that such a large magnetic field strength is associated with a radio source as bright as Cygnus A. The source of cluster-wide magnetic fields is unknown, and the presence of a strong radio source (either at present or in a previous outburst) may be responsible for the observed magnetic field.

Chapter 5. The effect of tangled magnetic fields on hot cluster gas

Our understanding of cooling flows is limited by an almost complete lack of knowledge of transport processes in the hot gas making up such systems. In this Chapter I concentrate on thermal conductivity in clusters of galaxies, although the discussion applies equally well to other transport processes and to elliptical galaxies and the interstellar medium.

As emphasised in Chapter 1, observations of the X-ray spectra of clusters of galaxies indicate that gas at a wide range of temperatures is present (see Sarazin 1986, Section III.C). The thermal continuum is only well modelled if more than one temperature component is assumed to be present. Studies of X-ray line emission with the *Einstein* Solid-State Spectrometer (Mushotzky & Szymkowiak 1988) imply that cooler gas is present that makes little contribution to the continuum emission. In both ultraviolet (Fabian, Nulsen & Arnaud 1984) and optical (Lynds 1970; Heckman 1981; Cowie *et al.* 1983; Heckman *et al.* 1989) wavebands filaments of gas at $\sim 10^4$ K are seen.

The presence of material coexisting at a wide variety of temperatures has led to a longstanding problem, as thermal conductivity at the Spitzer (1962) value is expected to erase temperature gradients and lead to an isothermal intracluster medium. Rephaeli & Wandel (1985) showed that clouds of gas at temperatures between 10^4 K and 10^7 K cannot coexist with hotter intracluster gas unless heat flow between the clouds and hot gas is substantially reduced. Takahara & Takahara (1979) proposed an alternative to the cooling flow scenario in which cold gas in the centre of the system was being conductively evaporated by hotter outlying material. Binney & Cowie (1981) argued that thermal conductivity in M87 had to be reduced by nearly three orders of magnitude.

One would expect that thermal conductivity should play an important part in the energetics of the intracluster medium. The fact that it appears not to requires some explanation. There is no evidence that thermal conductivity differs significantly from the Spitzer (1962) value under a wide range of physical conditions, at least in directions parallel to the magnetic field. Classical conductivity appears to apply in the Interstellar Medium (Cowie & McKee 1977; McKee & Cowie 1977), in the outer atmospheres of stars (see, for example, Jordan *et al.* 1987) and in fusion devices such as Tokamaks (Haas & Thyagaraja 1986). In directions perpendicular to the magnetic field there appears to be anomalous enhanced transport (see Haas & Thyagaraja 1986 for a review). There is no evidence for a reduction in thermal conductivity in any of these cases. Despite this it is commonly assumed that tangled magnetic fields reduce thermal conductivity. In simple treatments (e.g., Pallister 1987) the procedure has been to multiply the Spitzer value of thermal conductivity by a global constant, assuming that the form of the Spitzer conductivity is correct and that the process that reduces thermal conductivity is independent of radius and other physical parameters, although Bregman & David (1988) assumed that the field lines would be stretched by the flow and lead to less reduction at the centre. Such models imply that reduction factors of 1% are necessary. Although this conclusion has not gained universal acceptance (see Meiksin 1988) I will argue that there are good reasons for thinking that the macroscopic heat flux is indeed reduced by a large factor, whilst retaining the Spitzer (1962) conductivity at the microscopic level.

In Section 5.1 I consider the effect of a magnetic field on the flow of heat, and go on to use two simple models of the magnetic field to calculate the heat flux in a clean mathematical setting. The relevance of magnetic fields for thermal instability and the optical filament systems observed in clusters of galaxies is considered in Section 5.2. A short summary is given in Section 5.3.

5.1 The Influence of Magnetic Fields

In the presence of a magnetic field, electrons in a plasma spiral around the field lines. They are free to move parallel to the field but excursions across the field are limited to one gyroradius r_g, which is usually very much smaller than the Coulomb mean free path λ_e. For example, in the intracluster medium $r_g = 3 \times 10^6 T_8^{1/2} B_\mu^{-1}$ m whereas $\lambda_e = 7 \times 10^{20} T_8^2 / n_{-3}$ m, where T_8 is the temperature in 10^8 K, n_{-3} is the electron density in 10^{-3} cm^{-3}, and B_μ is the magnetic field strength in μG, so that $r_g / \lambda_e \approx 10^{-14}$.

Consequently thermal conductivity is almost completely eliminated in directions perpendicular to the magnetic field, and unaffected parallel to the field. I will therefore assume that the heat flux at all points is in the direction of the field, and proportional to the temperature gradient along the field, the proportionality constant being that given by Spitzer (1962). The next Chapter suggests that the conductivity along the field will be reduced somewhat by magnetic mirroring, but this is irrelevant for the present discussion—the important fact is that the conductivity across the field is negligible. Since electrons can only move freely along field lines, the field lines are effectively insulated from each other and are independent. Hence I now analyze the thermal properties of a system of thermally isolated field lines.

5.1.1 THE RANDOM WALK APPROXIMATION

Consider a particularly simple model in which the magnetic field is approximated by a random walk. Two parallel plates of temperatures T_1 and T_2 are placed a distance $L = as$ apart, where s is the step of the random walk. A constant conductivity is assumed. A field line is allowed to walk at random until it reaches one of the bounding plates. Three types of field lines will be found:

(i) Those which have both ends attached to the plate at temperature T_1. The temperature at all points along these field lines is T_1.

(ii) Those which have both ends attached to the plate at temperature T_2. The temperature at all points along these field lines is T_2.

(iii) Those which make it across from one plate to the other. The temperature is assumed to be a linear function of distance along the field line.

When successive steps are uncorrelated, this problem is well known as the Gambler's ruin problem (Feller 1950). Two gamblers, one with capital k and the opponent with capital $a - k$ gamble for one unit of capital with equal probabilities of either player winning. The course of the game, described by the capital of the first player, is a bounded random walk with $k = 0$ corresponding to ruin and $k = a$ to victory. The expected duration of the game can be found. For the thermal conductivity problem winning (ruin) corresponds to reaching the plate at T_2 (T_1) and the duration of the game to the path length between the plates.

The probability of reaching the plate at T_2 starting from position k is

$$P_k = k/a$$

and of reaching the other plate is

$$P_k = 1 - k/a.$$

Therefore at points k steps distant from the plate at T_1 a fraction $(1 - k/a)^2$ of the field lines are at temperature T_1, a fraction $(k/a)^2$ are at T_2 and a fraction $2(k/a)(1 - k/a)$ are at intermediate temperatures. The macroscopic temperature k steps from the first plate is taken to be the average temperature of all field lines through k. For large separations of the plates much of the gradient in the average temperature is given by the varying fractions of field lines of types (i) and (ii). This

clearly demonstrates that in these circumstances a large scale temperature gradient will not necessarily lead to a significant heat flux, even if the conductivity is large.

The probability of reaching plate 2 or 1 from position k in exactly m or n steps is written as P_{km} and Q_{kn} respectively. By assumption (iii) above the temperature at a point on a field line at k that is m steps from T_2 and n steps from T_1 is

$$T_{mn} = \frac{mT_1 + nT_2}{m+n}, \tag{5.1}$$

so the average temperature at k is

$$\begin{aligned} \langle T_k \rangle &= (1-k/a)^2 T_1 + (k/a)^2 T_2 + 2\sum_{n=k}^{\infty}\sum_{m=a-k}^{\infty} Q_{kn}P_{km}T_{mn} \\ &= T_1 + (k/a)(T_2 - T_1) + \Delta T, \end{aligned} \tag{5.2}$$

where

$$\Delta T = (T_1 - T_2)\sum_{n=k}^{\infty}\sum_{m=a-k}^{\infty} Q_{kn}P_{km}\frac{m-n}{m+n}. \tag{5.3}$$

The average temperature distribution is approximately linear, with a small perturbation given by ΔT.

Near to any point there will be a large number of field lines which will have different temperatures. This leads to a very fine scale multiphase picture of the intracluster medium (Nulsen 1986,1988). This can be quantified by considering the temperature dispersion σ_T defined by

$$\sigma_T^2 = \langle (T - \langle T \rangle)^2 \rangle. \tag{5.4}$$

Fig. 5.1 shows graphs of $\langle T \rangle$ and σ_T as a function of distance between the plates. Details of how these quantities were obtained are given in Appendix 5B.

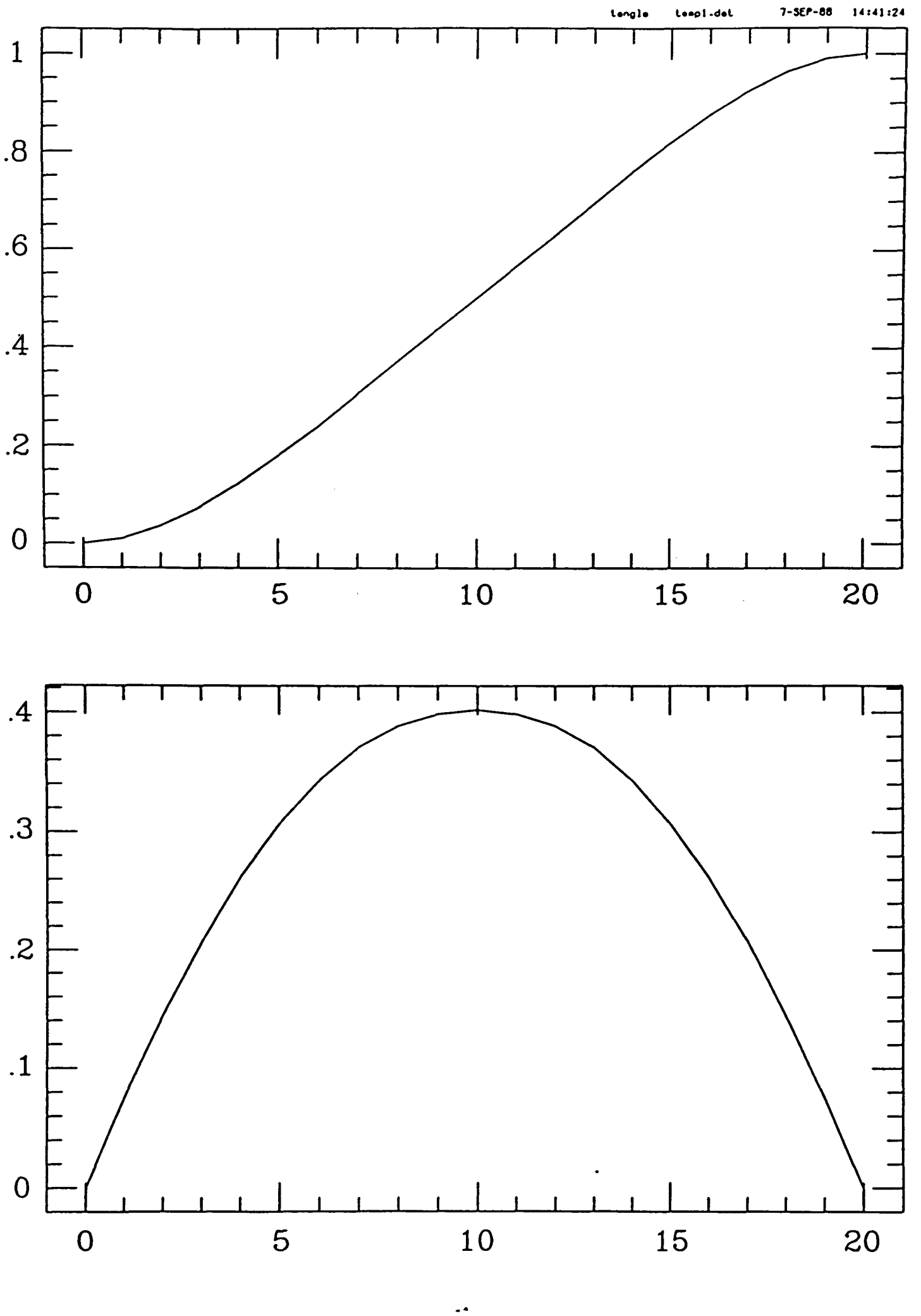

Figure 5.1. The macroscopic temperature structure of a material between two parallel plates: the mean temperature as a function of distance between the plates (top); the temperature dispersion as a function of distance between the plates (bottom). Distances are in terms of the field step length and temperatures are in terms of the temperature difference between the plates.

5.1.2 CALCULATION OF HEAT FLUX

In calculating the heat flux only those field lines that succeed in making it from one plate to the other need be considered. In particular, we may look at those field lines at $k = 1$ that reach the plate at T_1 in one step, so that $n = 1$. This collects all field lines as they leave plate 1. The heat flux between the plates is proportional to the probability of a field line succeeding in reaching plate 2 multiplied by the average temperature gradient along those that do. This is

$$P_1 \nabla T = \sum_{m=a-1}^{\infty} \frac{P_{1m}}{m+1} \frac{(T_2 - T_1)}{s}. \tag{5.5}$$

To evaluate this expression we use the generating function $\mathbf{P}_k(x) = \sum_m P_{km} x^m$ where (Feller 1950)

$$\mathbf{P}_k(x) = \frac{\sin k\phi}{\sin a\phi} \quad ; \quad x \equiv \frac{1}{\cos \phi}. \tag{5.6}$$

This expression allows us to turn the sum in equation (5.5) into an integral:

$$\sum_{m=a-1}^{\infty} \frac{P_{1m}}{m+1} = \int_0^1 \sum P_{1m} x^m dx \tag{5.7}$$

$$= \int_0^1 \mathbf{P}_1(x) dx \tag{5.8}$$

$$= \int_0^{\infty} \frac{\tanh^2 y}{\sinh ay} dy,$$

where $\phi = iy$. Let $z = ay$. Then

$$\sum_{m=a-1}^{\infty} \frac{P_{1m}}{m+1} = \frac{1}{a} \int_0^{\infty} \frac{\tanh^2(z/a)}{\sinh z} dz. \tag{5.9}$$

For large a we may expand $\tanh^2(z/a)$ as z^2/a^2 because the $\sinh z$ in the denominator kills the integrand before this approximation breaks down. This integral is given in Gradshteyn & Ryzhik (1980; 3.523.1) so the sum is approximately

$$\sum_{m=a-1}^{\infty} \frac{P_{1m}}{m+1} \simeq \frac{4}{a^3}. \tag{5.10}$$

The separation of the plates is $L = as$, so the total heat flux is

$$F = -4\kappa \left(\frac{s}{L}\right)^2 \frac{T_2 - T_1}{L}. \tag{5.11}$$

This result can be easily understood. The probability of a field line which leaves one plate reaching the other is $1/a$ and the average number of steps taken is $\sim a^2$.

For an n-dimensional random walk between two parallel plates there is very little change in the mean temperature and temperature dispersion. The extra dimensions are treated by allowing the field lines to walk parallel to the plates, which in the terminology of the gambler's ruin problem is a draw. The heat flux calculation is changed only by the replacement

$$x \to x' \equiv \frac{n}{(n-1) + \cos\phi} \tag{5.12}$$

(see Cox & Miller 1965) which reduces the flux by a factor n.

This result has serious implications. First, a coefficient of thermal conductivity no longer exists in the conventional sense: the heat flux is not inversely proportional to the separation of the plates, so that measuring the "thermal conductivity" of a sample of a material will lead to a result dependent on the size of the sample. Second, if the step length is small compared to the separation of the plates then there is a substantial reduction in the heat flux compared to that expected by taking the macroscopic temperature gradient and applying classical conductivity.

5.1.3 THE CORRELATED RANDOM WALK APPROXIMATION

Although the results of the simple random walk model give a good feel for the reduction process, the description of the magnetic field as a simple random walk is obviously unrealistic. As the next step I therefore describe the field as a correlated random walk, although still in one dimension. A correlated random walk is a random

walk in which the probability of going forward or back on step n depends on the direction chosen on the preceding step, so denoting steps forward and backward by $+$ and $-$ respectively, and the conditional probability of A given B on the preceding step as $P(A \mid B)$:

$$\begin{aligned} P(+ \mid +) &= \alpha \qquad & P(+ \mid -) &= \beta \\ P(- \mid +) &= \beta \qquad & P(- \mid -) &= \alpha. \end{aligned} \tag{5.13}$$

The relevant properties of a correlated random walk are summarized in Appendix 5A. The probability of a field line reaching the other plate is increased over an uncorrelated walk. Denoting the nature of the previous step by a superscript arrow, we again wish to pick up all the field lines as they leave the lower plate. This is done by considering only the generating function $\mathbf{P}_1^{\uparrow}(x)$, where from Appendix 5A

$$\mathbf{P}_1^{\uparrow}(x) = \frac{\alpha}{\beta} \frac{\sin\phi}{\sin[\sin^{-1}(\frac{\alpha}{\beta}\sin\phi) + (a-1)\phi]}. \tag{5.14}$$

Here

$$\cos\phi \equiv \frac{1+(\alpha-\beta)x^2}{2\alpha x}. \tag{5.15}$$

The heat flux is determined from equation (5.5) as before. The result is

$$F = -\frac{4\kappa}{a^3}\left(\frac{\alpha}{\beta}\right)^2 \frac{T_2 - T_1}{s}. \tag{5.16}$$

The heat flux is increased over the uncorrelated case by the factor $(\alpha/\beta)^2$. In the limit as the step length s goes to zero and the correlation goes to unity to keep a finite correlation length L_c (see Appendix 5A) the heat flux becomes

$$F = -16\kappa\left(\frac{L_c}{L}\right)^2 \frac{(T_2 - T_1)}{L}. \tag{5.17}$$

Thus in the more complicated and more realistic case of a correlated random walk the same scaling of the heat flux with the field's correlation length and the separation of the plates is obtained as for the simple random walk. It seems reasonable to extend this behaviour to realistic magnetic fields which are not amenable to so simple an analysis.

5.1.4 RANDOM WALKS IN SPHERICAL SYSTEMS

In a spherical system the bounding plates are concentric spheres. If these are of similar radii then the parallel plate analysis applies. If the spheres are of different sizes then the variation of step length with radius becomes important. The strength and scale lengths of magnetic fields are expected to vary with radius in a cluster (Jaffe 1980). If simply transported by a cooling flow the field strength will increase and the scale length decrease as radius decreases (Soker & Sarazin 1988). If the step length is proportional to r then the grid can be unfolded and the problem is equivalent to the parallel plate case with a position dependent step length. I therefore present results, in Fig. 5.2, from a model in which the scale length scales with radius.

In the unlikely case that the step length were independent of radius then the problem would be qualitatively different: it is well known (Feller 1950) that for a three-dimensional random walk on a cartesian grid approximately 1/3 of all walks leaving a point return and the remaining 2/3 never return, wandering to infinity. If the inner sphere is small compared to a step length approximately 2/3 of all field lines leaving it make it to the outer sphere. The extra path length due to the walk will still act to reduce the heat flux.

The presence of the bounding plates is necessary to make the problem tractable. I assume that the plates are equivalent to regions where the gas is mostly cold (at the centre, due to cooling) and mostly hot (at large radii, due to all thermal timescales being longer than the age of the gas).

One may now estimate the reduction in heat flux. Consider a cluster in which the field scale length is proportional to radius, approximately 10–20 kpc at a few hundred kpc (Lawler & Dennison 1980; Dreher, Carilli & Perley 1987). Therefore the ratio of field scale size to system scale size is $\sim 1/10$ leading to the heat flux

being reduced to 1% of that derived from the macroscopic temperature gradient and Spitzer conductivity.

5.1.5 MULTIPHASE MODELS OF THE INTRACLUSTER MEDIUM

A multiphase medium was shown in Section 5.1.1 to be an inevitable consequence of the presence of tangled magnetic fields in an atmosphere with a temperature gradient. This has also been suggested from observational considerations. First, fitting the X-ray profile to models leads to a mass flow rate that varies with radius (Nulsen 1986,1988; Thomas, Fabian & Nulsen 1987). It is argued that the flow is in a steady state and that this implies that mass is dropping out of the flow at a range of radii, and therefore that a range of gas properties exist at all radii. Second, the volume filling factor of cool gas required to produce the observed Fe XVII line emission in Perseus is such that it would lead to the continuum emission being too centrally concentrated if the cool gas were the only phase present (Canizares, Markert & Donahue 1988).

For any model it is possible to calculate the standard deviation of the temperature from the mean. For the simple random walk this result is shown in Fig. 5.1, and for a more realistic case in spherical symmetry the results of Fig. 5.2 are obtained. These models clearly show that we expect to see a continuous range of temperatures at any radius, with the temperature dispersion at a point being a substantial fraction of the temperature range supported by the entire system.

What of the temperature structure along an individual field line? If the conductivity is not reduced parallel to the field then temperature varies linearly along a field line. In addition, small perturbations will be quickly damped. Perpendicular to the field, conductivity is unable to impose uniformity. The temperature at a point is not determined locally but is fixed by the global temperature structure and

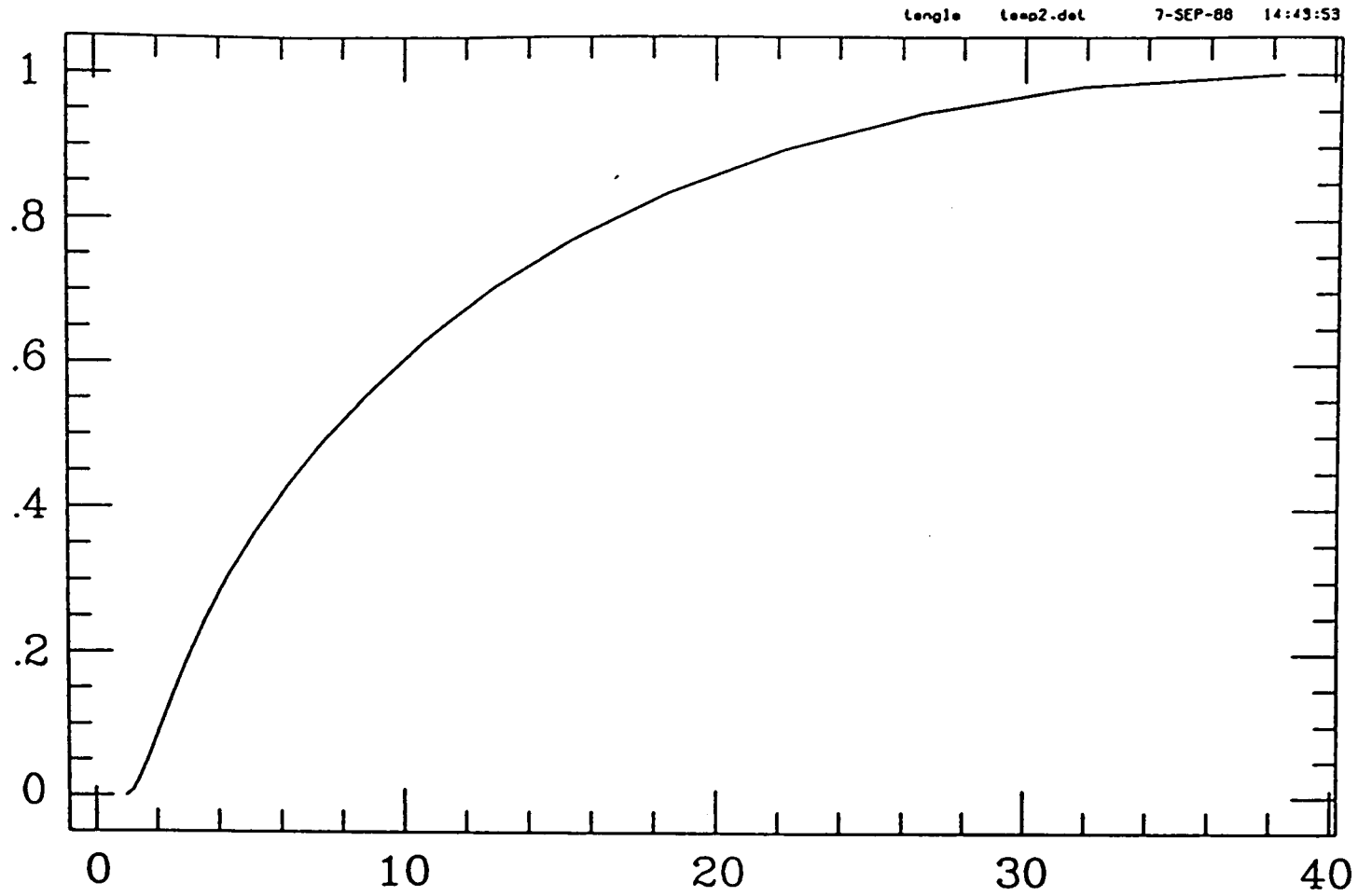

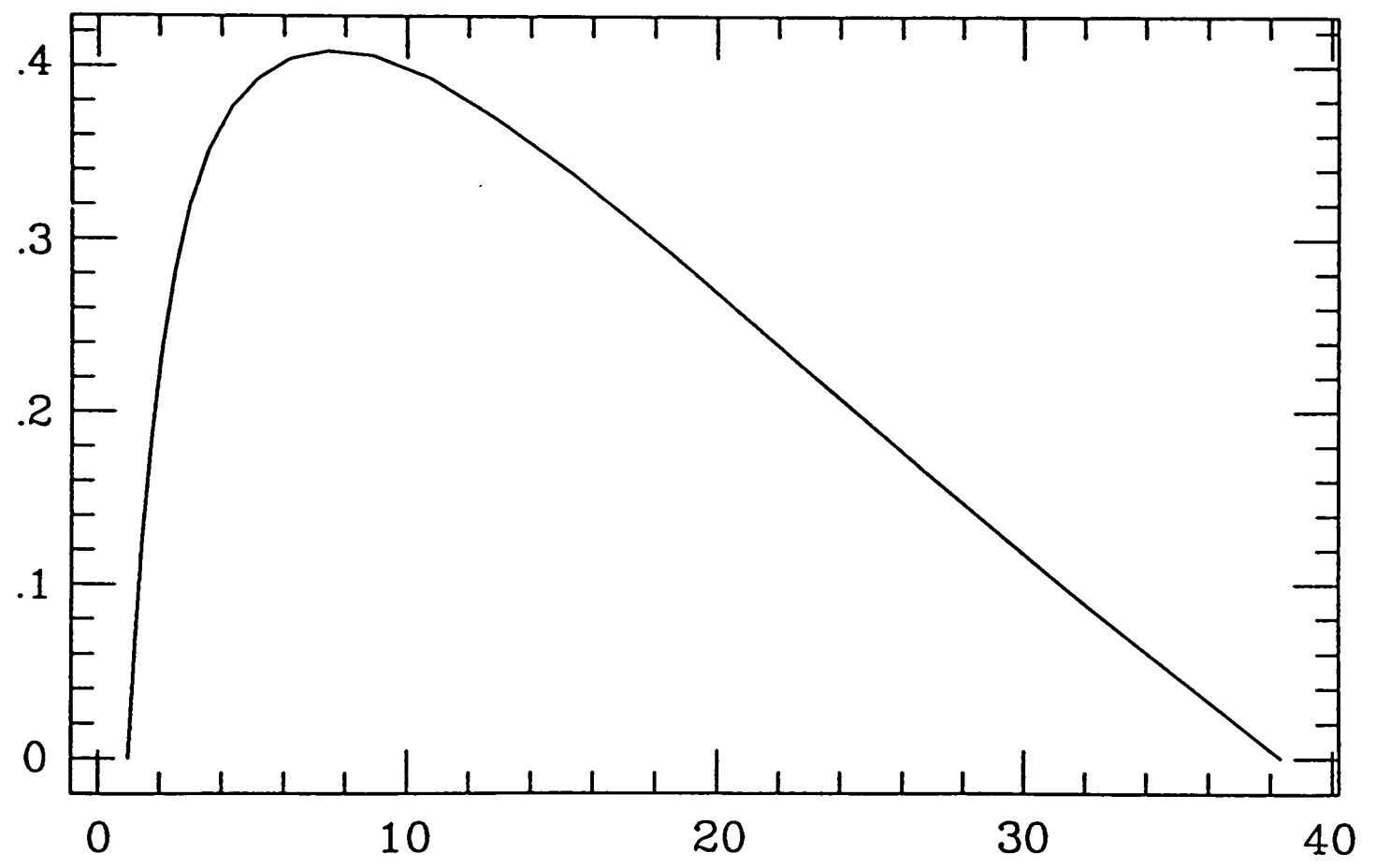

Figure 5.2. The temperature structure of a material between two concentric spheres: the mean temperature as a function of radius (top); the temperature dispersion as a function of radius (bottom). The step length is 0.2 times the radius at any point. Temperatures are in terms of the temperature difference between the plates.

the structure of the field line passing through that point. If the gas is in local pressure equilibrium then density inhomogeneities are necessarily present in the flow. The dynamics of such inhomogeneities must then be taken into account. This is too complicated to be considered here but has been considered by Nulsen (1986) and Thomas (1988).

The multiphase nature of the intracluster medium can affect attempts to use the Sunyav-Zel'dovich effect to measure the Hubble constant—the Hubble constant will be underestimated (see Silk & White 1978; McHardy *et al.* 1989).

5.1.6 STOCHASTIC MAGNETIC FIELDS

A potentially serious problem arises with the degree of isolation of field lines from one another. The magnetic field is assumed to be stochastic by treating it as a random walk. Such a complicated system as a magnetic field in a cluster would be expected to be stochastic in any case. It then follows that initially neighbouring field lines follow divergent paths and soon become well separated. This leads to intermingling of field lines of different temperatures (on small scales) and allows electrons to diffuse across the mean field, even in the absence of collisions. Stochastic diffusion of the field lines must be taken into account in a complete discussion of the effect of a magnetic field on thermal conductivity. For an application to cosmic ray diffusion see Jokipii & Parker (1969) and for diffusion across mean fields in fusion devices see Rechester & Rosenbluth (1978).

Magnetic field stochasticity leads to transfer of electrons across the field, reducing the isolation of field lines from one another and blurring the classification of field lines of Section 5.1.1. As long as the conductivity perpendicular to the field is much less than the parallel conductivity the field lines will still be effectively isolated. The important quantity is the length scale D_{st} on which the stochastic

divergence takes place—if this is short then the electrons will be well mixed, if long then the field lines retain their identity and the random walk description applies.

In clusters of galaxies we might expect a mean component not to be present, so that the entire field is stochastic. In this case the stochastic diffusion length is equal to the scale length of the field, $D_{st} \sim L_c$, and typically $\lambda_e \sim D_{st} \sim L_c$. Particles follow the stochastic diverging field lines until a collision occurs, and then are randomized and start off again on a different divergent path. Because $\lambda_e \sim D_{st}$ the particles only travel one divergence length between collisions, and in this distance two particles on originally neighbouring field lines will have only diverged by a few r_g. Relative to a mythical reference field line a particle will follow a random walk with step length a few r_g. A typical field line will be of length $N \sim 10^4$ steps so that the random walk perpendicular to the field will cause a separation of only $\sqrt{N} \sim 10^2$ steps, or only a few hundred r_g. Notice that the particles diffuse much more slowly across the mean field than do the field lines. With N being moderate the transverse thermal conductivity is still very much less than the conductivity parallel to the field, although much enhanced over the classical value. I conclude that magnetic field stochasticity is not important in the present context.

With field lines diverging exponentially stochastic effects rapidly become important if the field has structure on small scales. This could be important in multiphase models where the intracluster medium consists of many small blobs of gas—conductivity on scales of a few pc will not be completely suppressed if the field has structure on the scale of the blobs.

5.2 Instabilities and Filamentation

The description of the evolution of small perturbations (Chapter 2) needs revision in the light of the description of the intracluster medium developed here. Previ-

ous analyses considered linear perturbations around a smooth (i.e. homogeneous on small scales, although stratified) background equilibrium state. This is obviously inappropriate in the present case where the background state is highly inhomogeneous. The gas is intrinsically nonlinear on small scales. The work in Chapter 3 was concerned with long wavelength modes for which linear theory may be more appropriate.

Thomas (1988) and Nulsen (1986; 1988) have considered the evolution of inhomogeneous flows, but did not consider the magnetic field in the current context. Due to density variations some gas will cool more rapidly than its surroundings but thermal conductivity is effective along the field lines and will exert a stabilising influence. There is a critical wavelength below which perturbations are conductively stabilised which is approximately (Pallister 1987)

$$\lambda_{crit} \sim f^{1/2} T_7^{3/2} n_{-3}^{-1} \quad \text{Mpc.} \tag{5.18}$$

Here f is a constant customarily introduced to allow for a reduction in thermal conductivity and $T_7 = T/10^7$ K.

Along field lines $f = 1$ if conductivity is not suppressed (by magnetic mirroring or electron scattering off waves) so small scale perturbations are conductively damped. The scale length is measured along the field line, so that the gas in the centre of a cluster can cool because the total length along a tangled field line to hot gas can be longer than λ_{crit}.

Three perturbation scales are important. The first is the scale length of the field, as field lines walk between areas of different physical conditions on this scale. The second is the size of the cluster because this determines the scale of the background, and the third is the critical wavelength defined in equation (5.18). If thermal conductivity is fully effective along field lines then small scale perturbations are stabilised. Occasionally, however, magnetic fields have conspired to so reduce

the heat flux that the perturbation can grow. Only if the magnetic field sufficiently reduces the heat flux into an element of gas can that element of gas be unstable. The magnetic field has a twofold effect, determining the spectrum of density inhomogeneities (these should not be regarded as perturbations—they are a necessary part of an atmosphere threaded by a tangled magnetic field) and the local stability of the gas. It does these two tasks independently: there need be no correlation between density and stability.

We are therefore led to the hypothesis that the instabilities leading to the observed filaments are suppressed except at specific places where the magnetic field geometry especially restricts the flow of heat. These will be locations where, although thermal conductivity may be fully effective, the gas is not well connected to the rest of the intracluster medium. Specific field geometries ("islands" or tori) are involved. Alternatively, local suppression of thermal conductivity (e.g. by a magnetic mirror) restricts the flow of heat.

This hypothesis has several attractive features. It naturally explains the observed sizes of the filaments, by relating them to the magnetic field structure. Filament sizes should be similar to the scale length of the magnetic field. Magnetic fields have scale lengths of order 10 kpc (Chapter 4) which is indeed of order the filament size. This model does not require any deviation from the known properties of thermal conductivity in the intracluster medium, and introduces no free parameters. The major disadvantage is that very little is known about the magnetic field structure.

The evolution and propagation of waves in an inhomogeneous medium, such as that predicted by this Chapter, was discussed further in Chapter 3.

5.3 Conclusions

Cooling flows contain material at a wide range of temperatures. This is surprising in view of the ability of thermal conductivity at the classical (Spitzer 1962) value to erase all such temperature inhomogeneities on timescales much shorter than a Hubble time. In order to avoid this problem, it has been common practice to assume that tangled magnetic fields reduce thermal conductivity, due to the almost complete suppression of thermal conductivity in directions perpendicular to the field.

In this Chapter I have considered the effect of a magnetic field on the flow of heat through the intracluster medium. The heat flux is reduced from the value that would be expected from the macroscopic temperature gradient because the heat is forced to travel along circuitous paths. The macroscopic temperature gradient is caused by differing amounts of hot and cold field lines at any radius. A multiphase intracluster medium is an inevitable consequence of a tangled magnetic field being present in a cluster. Models of the intracluster medium should take into account (i) the large scale reduction in heat flux, (ii) the inhomogeneities caused by the magnetic field, and (iii) the fact that thermal conductivity is effective on small scales.

The model suffers from three deficiencies (i) the imposition of the two bounding plates, (ii) the inaccurate description of the magnetic field, and (iii) the lack of dynamical considerations. These do not detract from the qualitative description of the process whereby thermal transport is reduced in clusters of galaxies. A more quantitative explanation would need a much better understanding of the precise state of magnetic fields within clusters of galaxies than we have at present.

The reduction mechanism is restricted to scales much larger than the scale length of the field. Observed optical filament systems have scale sizes very similar

to the magnetic field. It was argued that a tangled magnetic field would contain regions where the local field geometry is such that a degree of isolation from the cluster at large is obtained. One expects thermal instability to develop in such disconnected regions. This naturally explains the observed filament sizes without any necessity for fine tuning the thermal conductivity suppression factor.

In the next Chapter I create genuine magnetic fields rather than random walks, but further work needs to be done on the dynamical aspects of this problem, and on the detailed evolution of unstable material.

Chapter 6. Magnetic field models

In the preceding Chapter magnetic field lines were represented as random walks. Magnetic fields aren't like this, so in this Chapter real (but not necessarily realistic) magnetic fields will be studied to see how they compare with the idealized random walk model.

6.1 Setting up the magnetic field

For the purposes of this Chapter a magnetic field is a vector field $\mathbf{B}$ which satisfies

$$\nabla.\mathbf{B} = 0. \tag{6.1}$$

This is the only constraint that will be imposed. Considerations of the field's origin, evolution and interaction with its surroundings will be ignored.

As a consequence of being divergence free, the field can also be described by a vector potential $\mathbf{A}$ in terms of which

$$\mathbf{B} = \nabla \wedge \mathbf{A}. \tag{6.2}$$

The quantities $\mathbf{B}$ and $\mathbf{A}$ may be decomposed into their Fourier components (the summation being an integral in the continuous case),

$$\begin{aligned} \mathbf{B}(\mathbf{x}) &= \sum_{\mathbf{k}} \tilde{\mathbf{B}}(\mathbf{k}) e^{i\mathbf{k}.\mathbf{x}} \\ \mathbf{A}(\mathbf{x}) &= \sum_{\mathbf{k}} \tilde{\mathbf{A}}(\mathbf{k}) e^{i\mathbf{k}.\mathbf{x}}. \end{aligned} \tag{6.3}$$

For (6.1) to be satisfied $\tilde{\mathbf{B}}$ must satisfy

$$\mathbf{k}.\tilde{\mathbf{B}} = 0, \tag{6.4}$$

while relation (6.2) between $\mathbf{B}$ and $\mathbf{A}$ implies that

$$\tilde{\mathbf{B}}(\mathbf{k}) = i\mathbf{k} \wedge \tilde{\mathbf{A}}(\mathbf{k}), \tag{6.5}$$

and the constraint that both $\mathbf{B}$ and $\mathbf{A}$ be real demands that

$$\begin{aligned} \tilde{\mathbf{B}}^*(\mathbf{k}) &= \tilde{\mathbf{B}}(-\mathbf{k}) \\ \tilde{\mathbf{A}}^*(\mathbf{k}) &= \tilde{\mathbf{A}}(-\mathbf{k}) \end{aligned} \tag{6.6}$$

I have elected to choose the Fourier components of $\mathbf{A}$, as this avoids the complication of ensuring that equation (6.4) is obeyed—choosing $\tilde{\mathbf{A}}(\mathbf{k})$ rather than $\tilde{\mathbf{B}}(\mathbf{k})$ means that this condition is automatically satisfied. The quantities $\tilde{\mathbf{B}}(\mathbf{k})$ are then derived using equation (6.5). As only two of the three components of $\tilde{\mathbf{B}}$ are independent only two of the three components of $\tilde{\mathbf{A}}$ are used, and the other set to zero. (This could be achieved by making a gauge transformation in any case.)

The $\tilde{\mathbf{A}}$ are chosen according to the prescription

$$P(A_i) = \frac{1}{\sqrt{2\pi}\sigma(k)} \exp\left(\frac{-A_i^2}{2\sigma^2(k)}\right), \tag{6.7}$$

where A_i represents either the real or imaginary part of a component of $\tilde{\mathbf{A}}$. It is convenient to change to polar coordinates and look at the amplitude and phase of A

$$P(A,\phi)\, dA\, d\phi = \frac{A}{\sigma^2} \exp\left(\frac{-A^2}{2\sigma^2}\right) dA\, \frac{d\phi}{2\pi}. \tag{6.8}$$

Therefore ϕ is uniformly distributed between 0 and 2π and A is drawn from a Rayleigh distribution.

6.2 Implementation

A programme to implement the above has been written. For each $\mathbf{k}$ there are four quantities to be assigned values: the real and imaginary parts of two components

of $\tilde{\mathbf{A}}$ (in this case the x and z components are used). For each component of $\tilde{\mathbf{A}}$ two random numbers x_1 and x_2 are chosen using a linear congruential random number generator initialised with a seed ISEED and shuffled using the routine RAN0 of Press *et al.* (1986). Different values of ISEED lead to different realizations of the field. The amplitude A and phase ϕ are then chosen as

$$\begin{aligned} A &= \sqrt{-2\sigma^2 \ln(1-x_1)} \\ \phi &= 2\pi x_2. \end{aligned} \tag{6.9}$$

The real and imaginary components of $\tilde{\mathbf{A}}$ are then $A\cos\phi$ and $A\sin\phi$ respectively. The field $\tilde{\mathbf{B}}$ is calculated as $\mathbf{k}\wedge\tilde{\mathbf{A}}$. At the same time $\tilde{\mathbf{B}}(-\mathbf{k})$ is also calculated with no extra effort.

The spectrum used for $\tilde{\mathbf{A}}$ was $\sigma^2(k) = k^{-2}\exp(-k^2/2k_0^2)$. A pure power law is scale invariant and so the gaussian factor is present to give a scale in the problem. This choice was made for simplicity. Other power law spectra were tried, and the resultant field lines didn't seem to be too dependent on the power law index. The cutoff used to give a physical scale was $k_0 = \sqrt{5}$. The cutoff scale is then $1/\sqrt{5}$ of the size of the grid.

Once the values of $\tilde{\mathbf{B}}$ have been placed in arrays according to the prescription of Press *et al.* (1986), their routine FOURN is used for each of the three (one for each component of the field) Fourier transforms.

To check the procedure two tests have been made.

(i) The average strengths of the real and imaginary components of the field were calculated. The strength of the imaginary part was found to be very much less ($\sim 10^{-7}$) than the real part, as it should be.

(ii) The field is statistically homogeneous. Therefore the field strength should not vary with position. The average field strength was calculated as a function of distance from the origin, and no systematic trends were found.

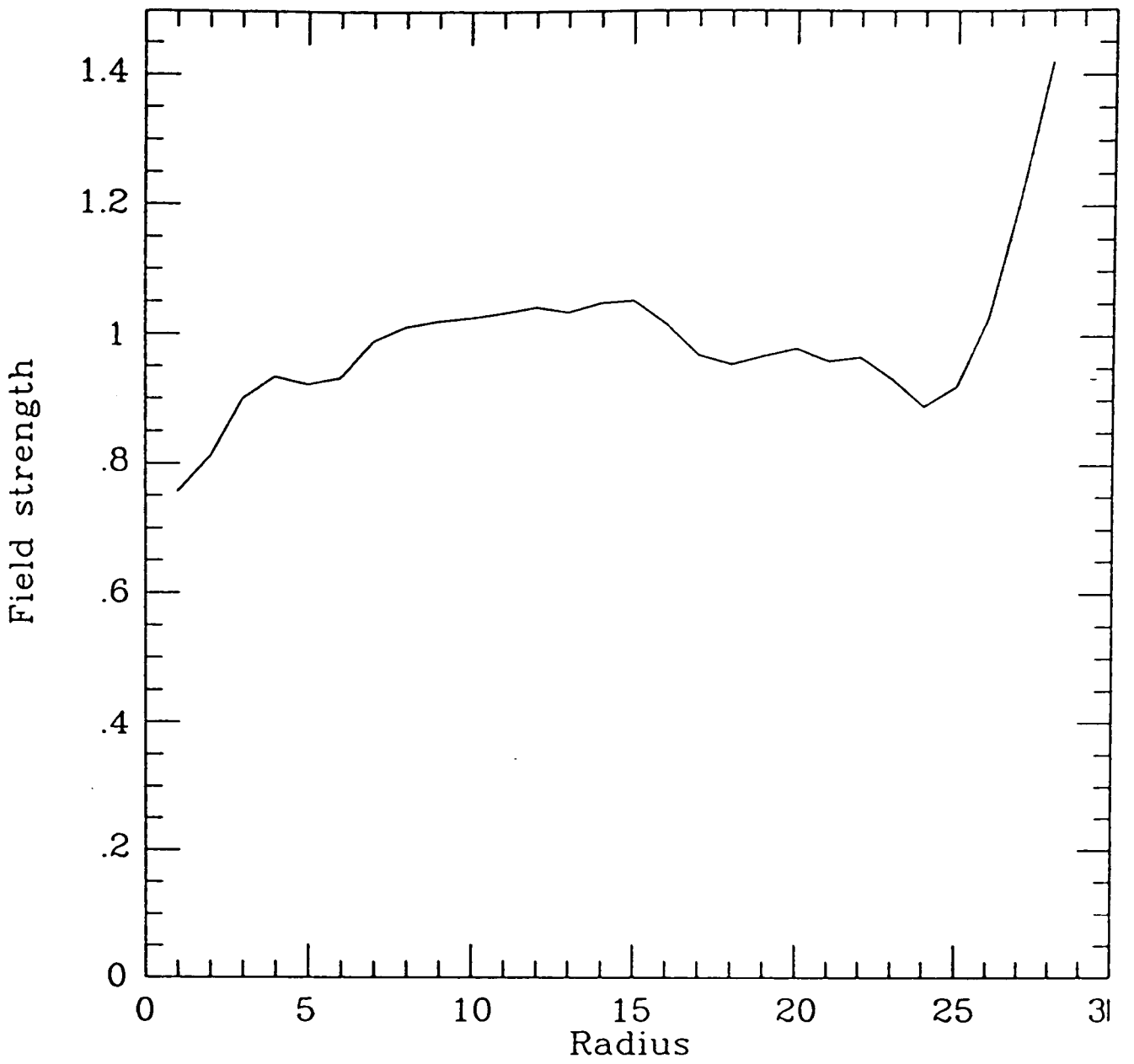

Figure 6.1. Magnetic field strength as a function of radius for a typical magnetic field. The imaginary component of the field is also plotted and is indistinguishable from the horizontal axis. Deviations at large and small radii are due to only a small number of grid points being used to calculate the average field strength in these cases.

Fig. 6.1 shows the field strength as a function of radius. The use of these tests showed that early versions of the program contained a few bugs, which were found to be errors in setting up the arrays for the Fourier transform routine.

Using a VAXstation 2000, a 32^3 grid can be used; setting up the field takes $\sim$ 1 cpu-minute. A 64^3 grid is feasible on such a machine but leads to the machine taking an excessive number of page faults. All of the results shown in this Chapter were derived using a 32^3 grid.

Having manufactured a realization of a magnetic field (albeit periodic and of small dynamic range), we can then proceed to analyse its properties. Those discussed in subsequent Sections are individual field lines, ensembles of field lines

(as used in Chapter 5), and synthesised Rotation Measure maps.

6.3 Magnetic field lines

Given a magnetic field we can then integrate the local **B** to construct field lines: these are (neglecting such things as curvature drift) the paths followed by electron guiding centres.

As a three dimensional vector field, **B** is difficult to visualize, and almost impossible to display. I therefore use field lines as a tracer of the magnetic field structure.

6.3.1 METHOD

The field line is a function **x** of a parameter t,

$$\mathbf{x}(t) = \int^{t} \mathrm{B}[\mathrm{x}(t')]\, dt'. \tag{6.10}$$

[Compare with $\mathbf{r}(t) = \int \mathbf{v}(\mathbf{r})\, dt'$.]

An initial point $\mathbf{x_0}$ is chosen. The field line is then integrated until either

(i) The number of points on the field line exceeds the size of the array to hold them.

(ii) A boundary is reached. Most of the individual field lines shown were stopped when they reached the boundaries of the grid. For comparison with the random walk models of Chapter 5 field lines were allowed to wrap around to the other side of the grid in certain directions, and only stopped on the remaining boundaries.

The field is interpolated from the grid using linear interpolation. The integration scheme used is second order Runge-Kutta, of the form

$$\begin{aligned} x' &= x_n + \frac{\Delta t}{2}\dot{x}_n, \\ x'' &= x_n + \Delta t \dot{x}'_n, \\ x_{n+1} = x'' &= +\frac{\Delta t}{2}(\dot{x}_n - 2\dot{x}' + \dot{x}''). \end{aligned} \tag{6.11}$$

In this case the stepsize was chosen to be inversely proportional to the field strength, so that all steps are approximately the same length, which is a small fraction (0.2 was found to be sufficient) of the grid spacing. The stepsize was adjusted and the step recomputed if the field strength grew by more than 25% during the step.

After reaching the 'end', I return to the initial point and integrate the field line the other way, to give a full field line.

6.3.2 TYPICAL FIELD LINES

The first point of interest is the general form of the field lines. Are they regular or irregular? Are they closed or open? Do they wander over the entire volume or are they restricted to a small region? I confine myself to showing a small sample of field lines that were found.

The figures are arranged so that the field line is shown viewed from along the three coordinate axes. At bottom right is the x-z view, above it the x-y view, and to the left of that is the y-z view. The square unless otherwise defined is the entire grid. At the top is shown the variation of magnetic field strength along the field line, as a function of the step number. (This tends to smooth out some of the variation in B as the step size is shortened where the field gradient is large.) The value of ISEED used to define the magnetic field and the starting coordinates of the field line are also shown.

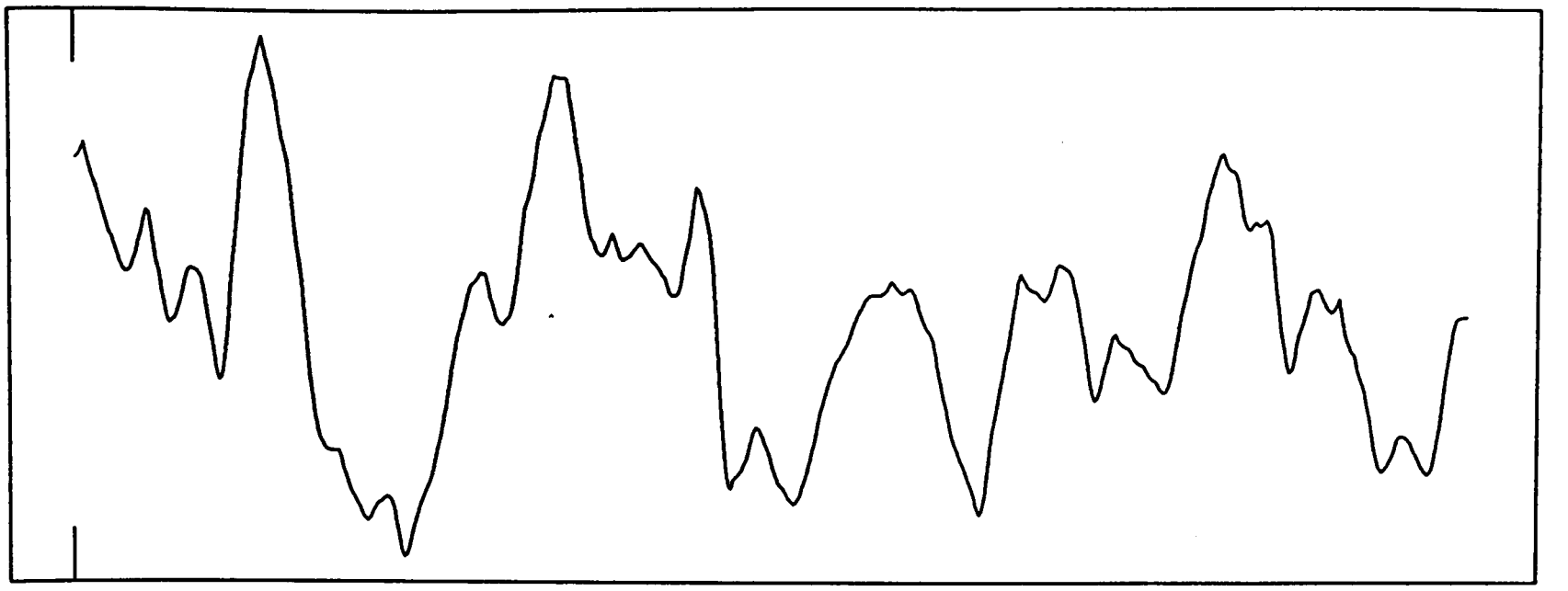

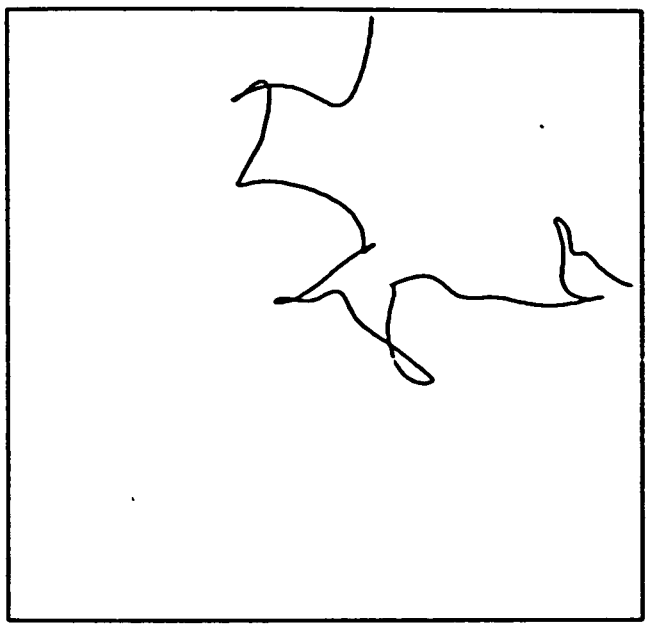

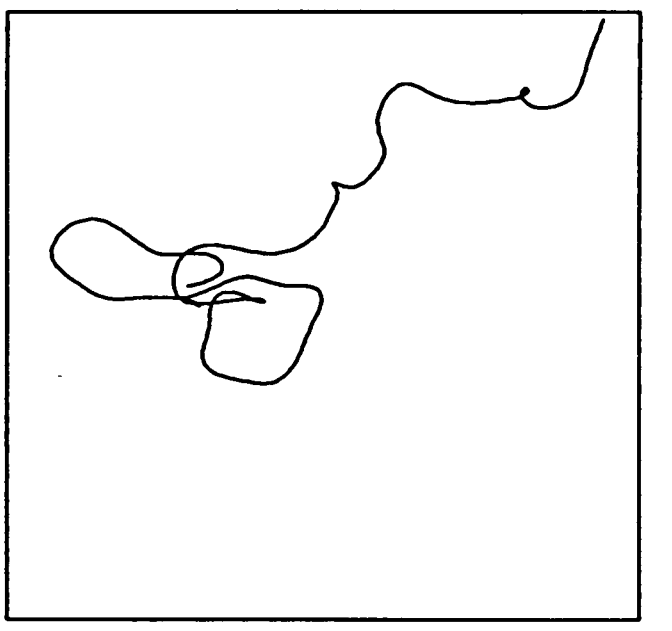

#43218765

Start (10,14,20)

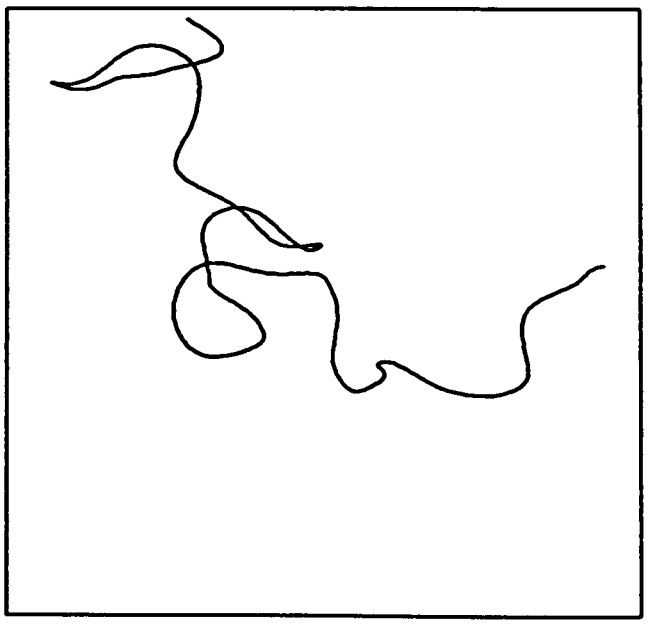

Figure 6.2. A typical field line.

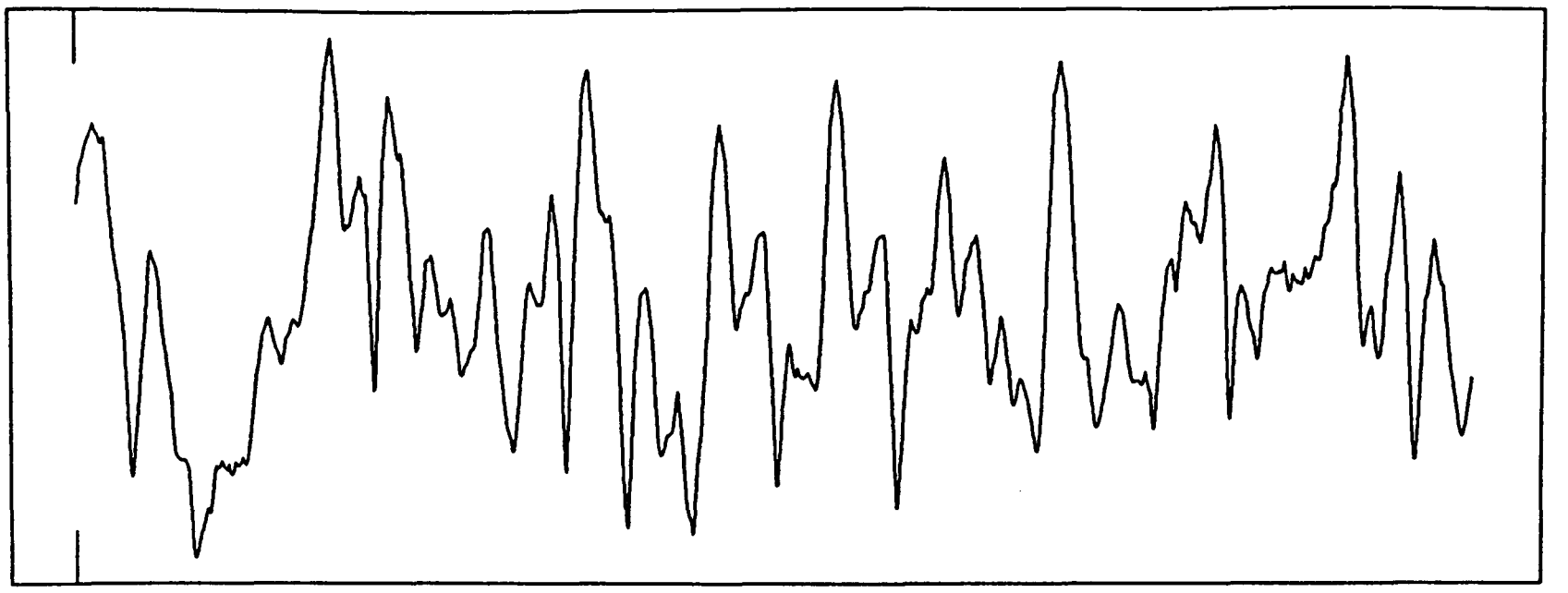

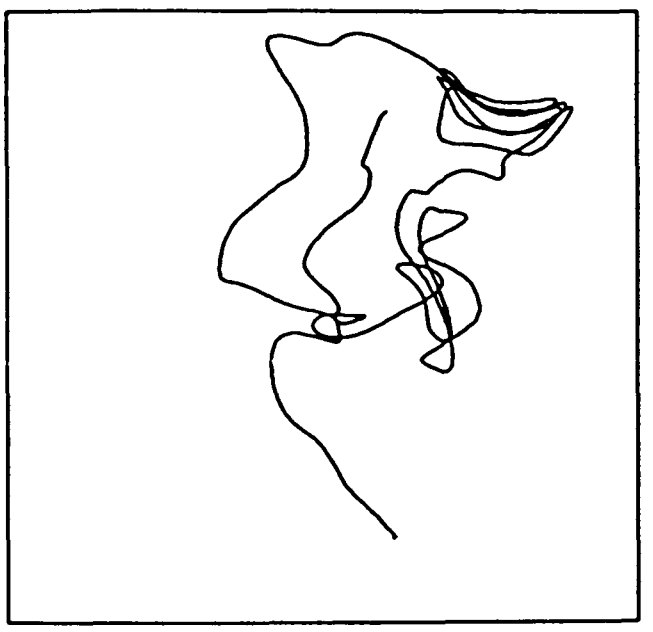

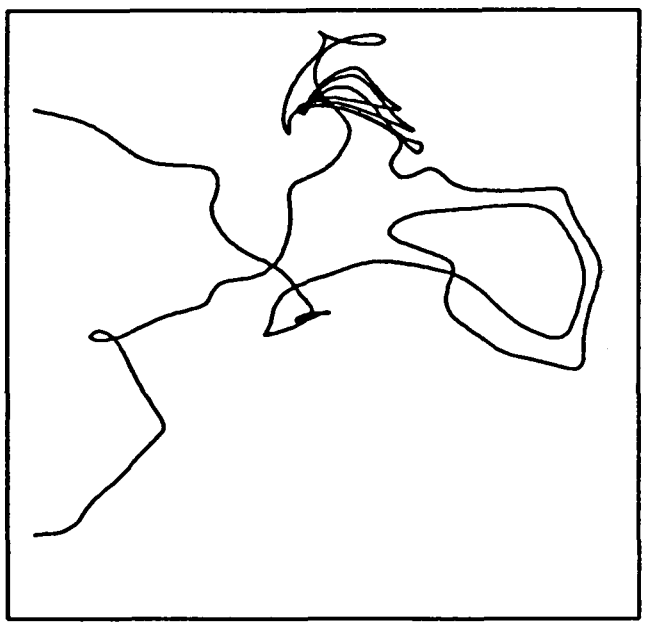

#4673419

Start (16,16,16)

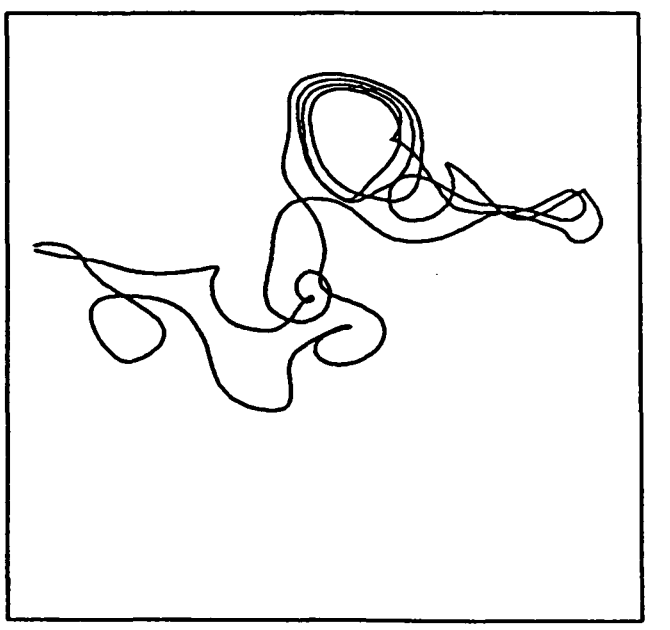

Figure 6.3. A complicated field line.

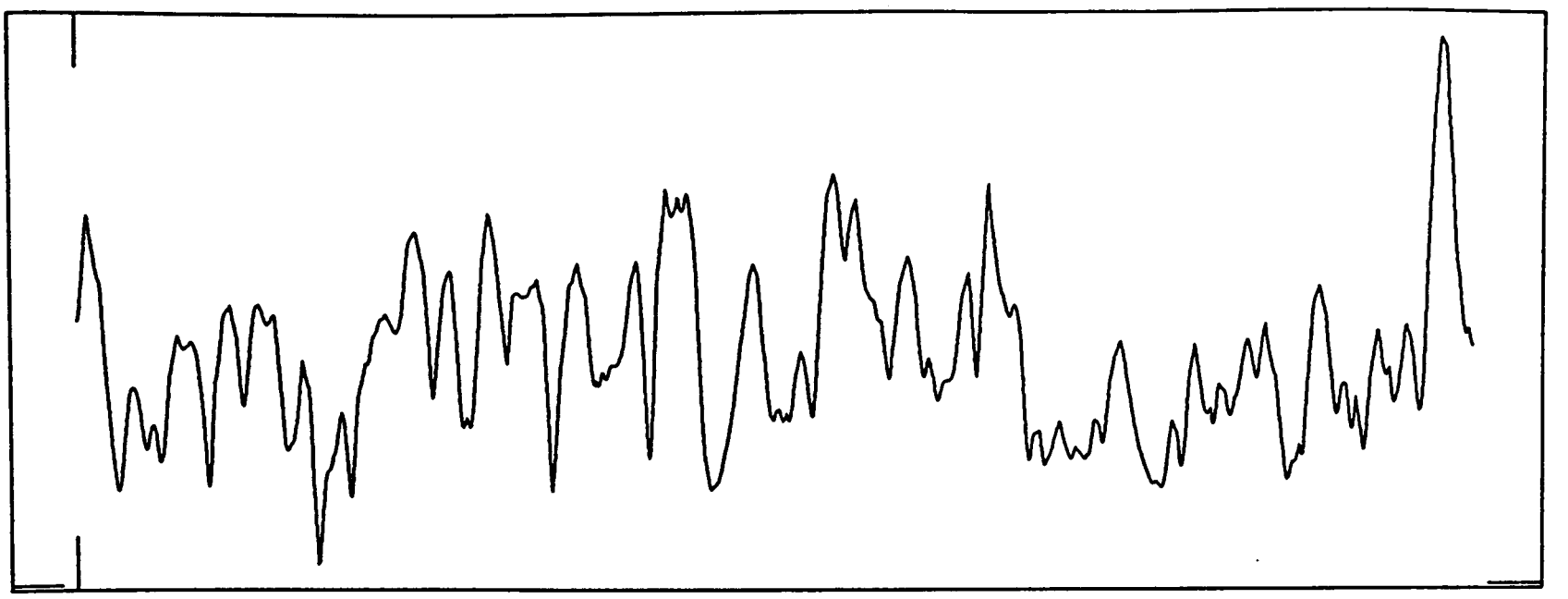

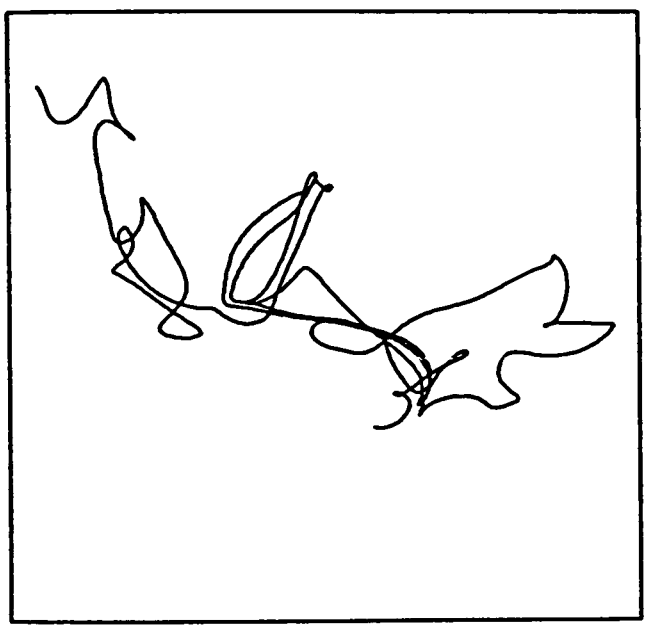

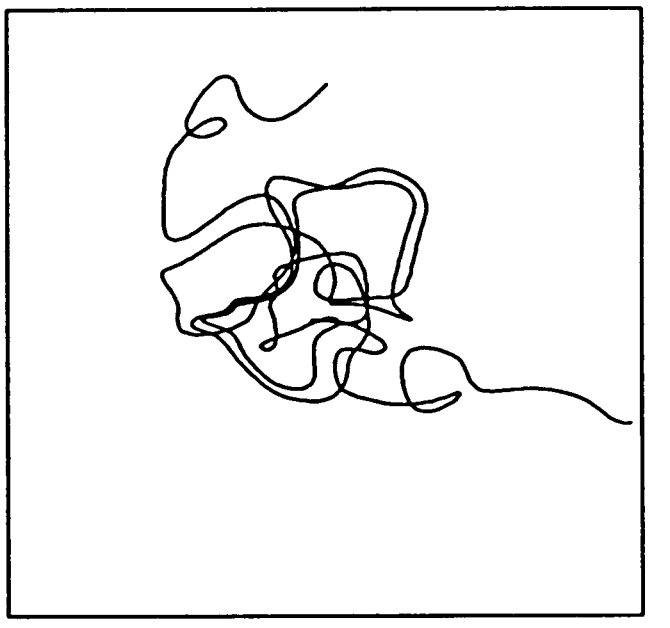

#4673419

Start (15.5,15.5,15.5)

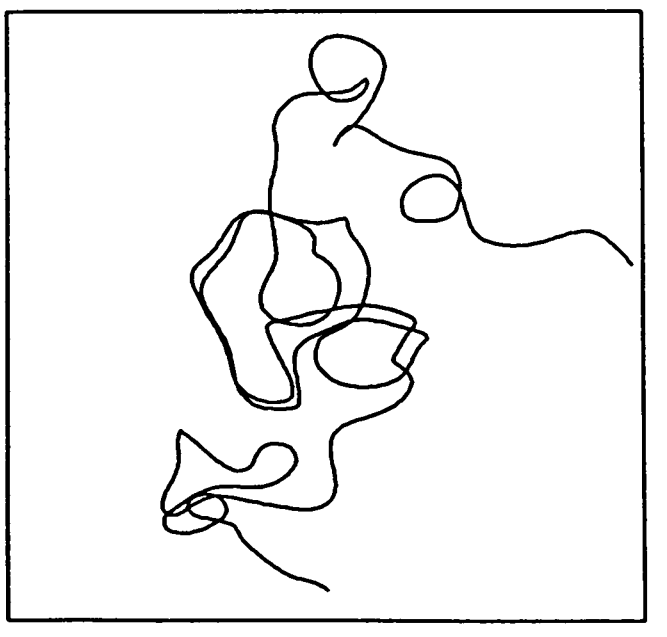

Figure 6.4. A neighbouring field line to that shown in the previous figure. Note that the structures are quite different. Neighbouring field lines do not stay close together.

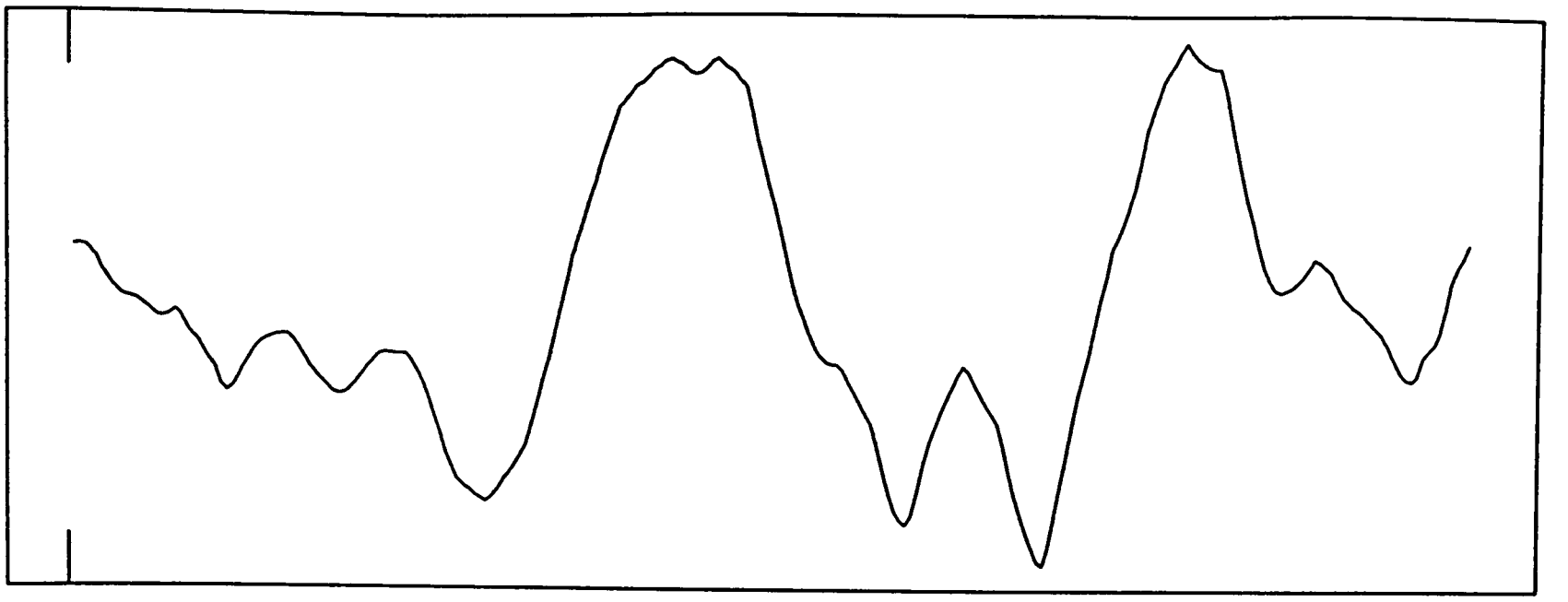

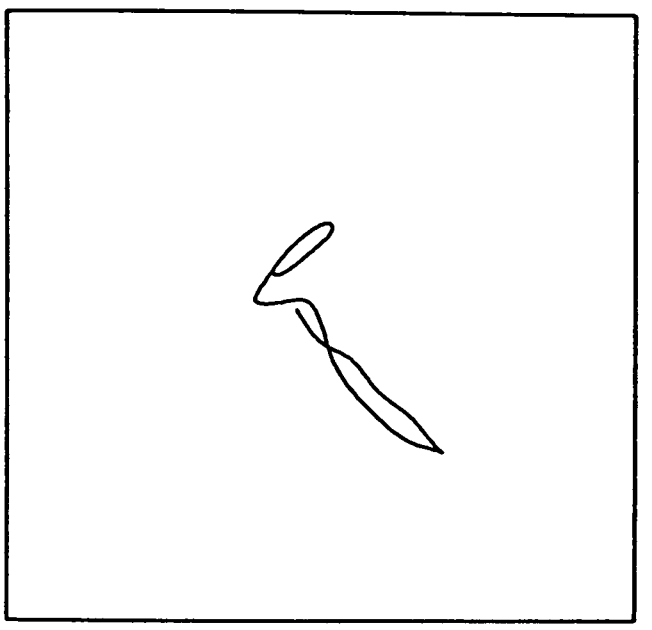

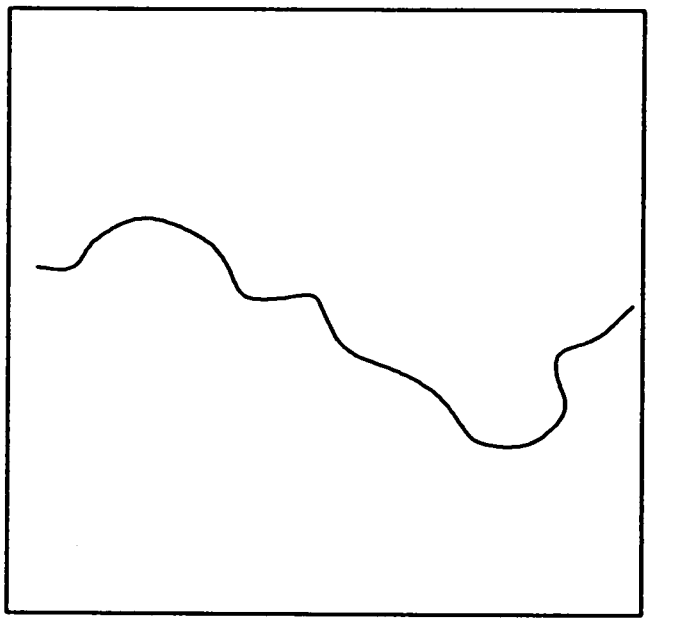

#91426347

Start (16,16,16)

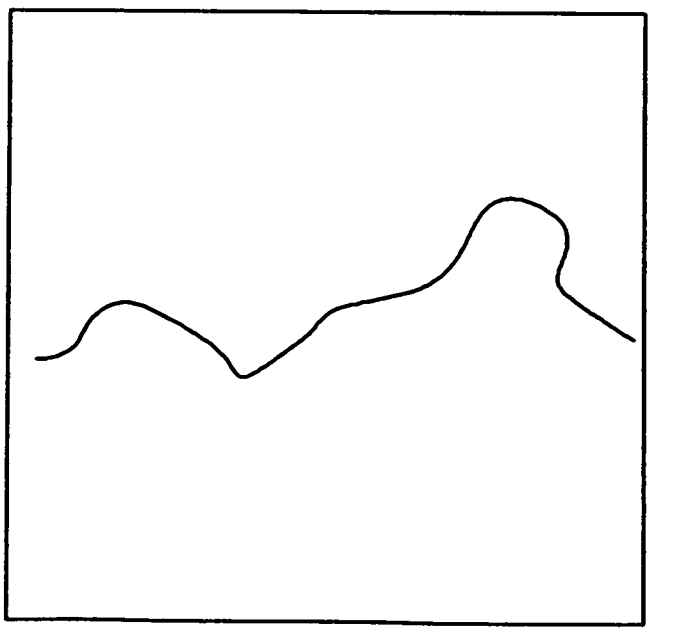

Figure 6.5. An example to show that not all field lines are horrendously tangled.

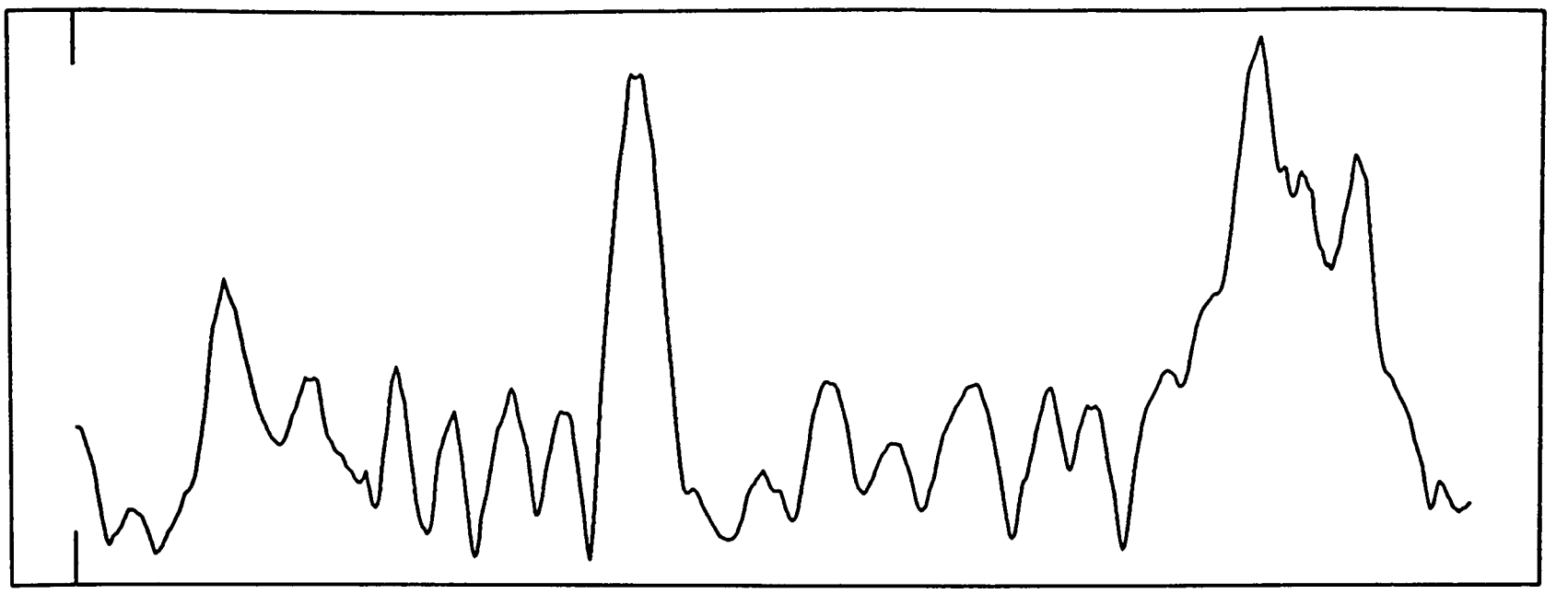

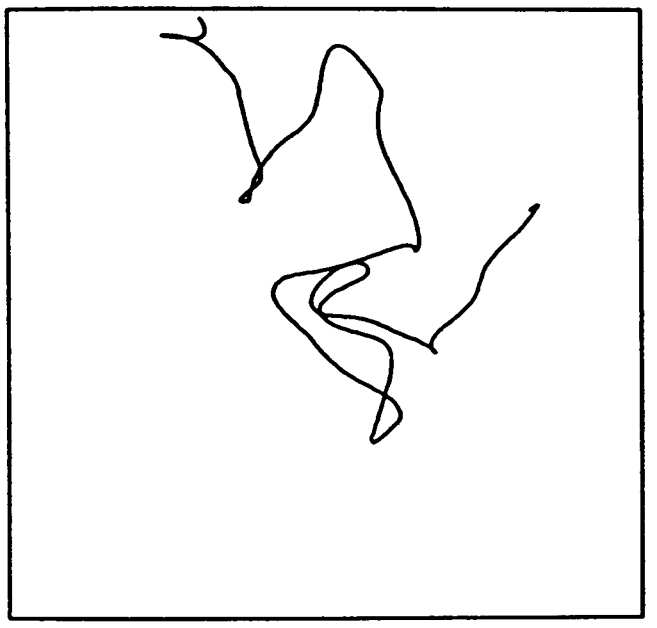

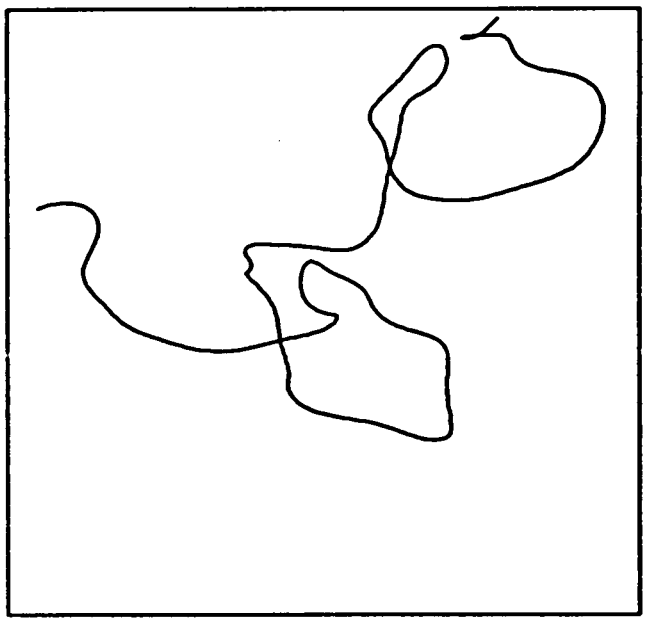

#13572468

Start (16,16,16)

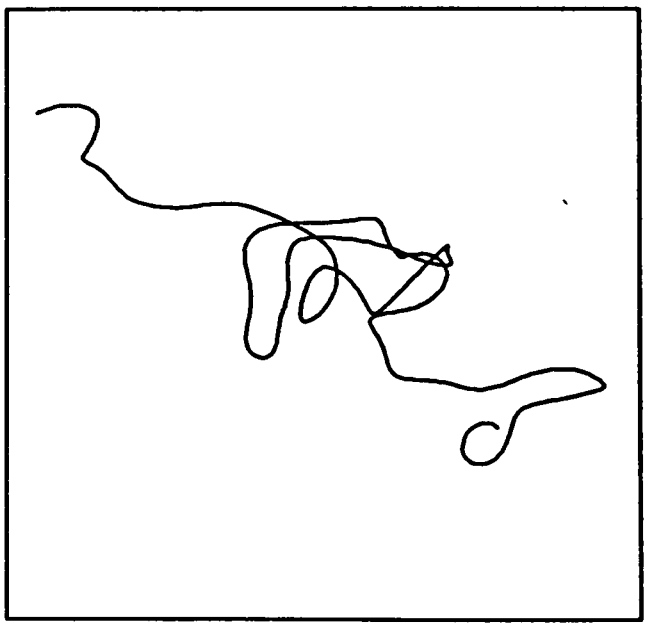

Figure 6.6. Another typical field line.

As can be seen, most field lines wander apparently randomly throughout the box. In addition, the field strength varies considerably along the field lines. Therefore, although neglected in Chapter 5 (and Tribble 1989b) the effects of magnetic mirroring on heat flow are likely to be severe.

6.4 An ensemble of field lines

In order to compare the results of using a real field rather than random walks to describe the field, a large sample of field lines is needed. In Chapter 5 a large sample of field lines were constructed as random walks. So exactly the same program can be followed with real field lines, in order to check whether the results for random walks are a good indicator for real field lines. If this is so then the results for the random walk case can be trusted. This is a great advantage—random walk models are a lot easier to build and impose a lesser load on computing facilities. In addition, random walk models can be constructed with a number of steps that is prohibitive when constructing a real field on a grid.

6.4.1 CONSTRUCTION OF THE SAMPLE

In Chapter 5 an idealized problem with bounding plates was considered. In the present case we allow the field lines to walk freely in the x and y directions but impose boundaries in the z direction. Because the grid goes from 1 to 32 and the field lines are stopped when they come within 0.5 of the edge of the grid the boundaries are at $z = 1.5$ and $z = 31.5$.

For a particular value of z, a selection of points gridded in x and y was taken. These were then integrated until they either reached the boundary in the z direction or the field line reached a maximum length (set by the array size).

6.4.2 PROBABILITY OF REACHING PLATES

We can classify field lines by which plate(s) the ends are attached to, as in Chapter 5. It is easy to work which class a given field line belongs to, so the relative proportions of field lines of the different classes can be found as a function of z, and compared to the random walk model.

As can be seen from Fig. 6.7 the classification of field lines follows the random walk model reasonably well. There is a slight discrepancy near to the plates. This is due to the fact that we are comparing a continuous function with the predictions of the random walk model which is discretised on a step length. As the step length is a few times the grid spacing we should expect the probabilities to flatten off as we approach the plates, as is seen.

The good agreement between the real field lines and the predictions of the random walk model is encouraging.

6.5 Rotation Measure maps

Having constructed a magnetic field it is then easy to calculate the rotation measure. I assume that the electron density is uniform, and the RM can be calculated by using the formula

$$RM(i,j) \propto \sum_i B_z(i,j,k). \tag{6.12}$$

The x direction is used for numerical efficiency.

I show an example of an RM map synthesised in this way in Fig. 6.8. Much more work remains to be done on relating the synthesised RM maps to the observations.

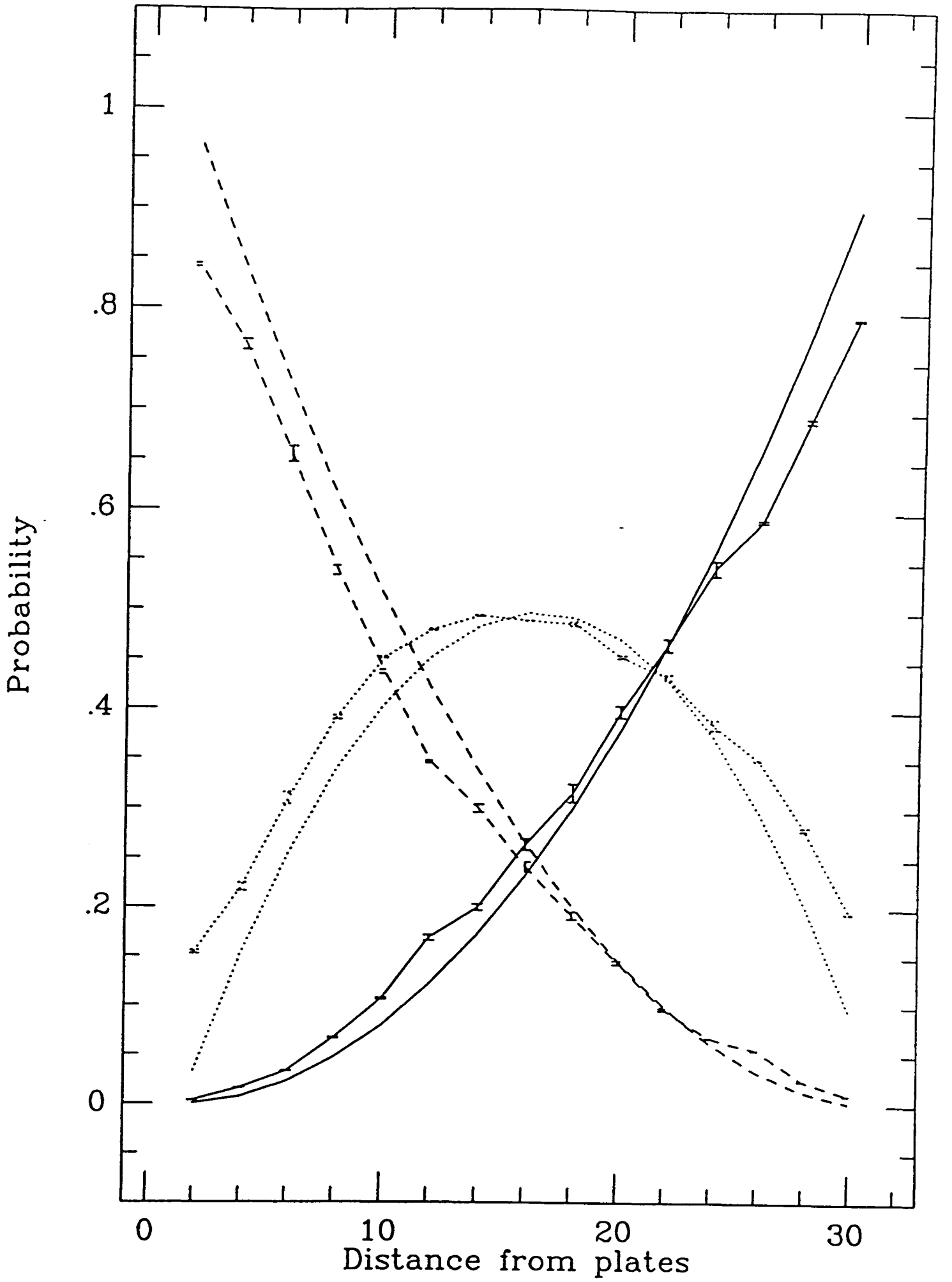

Figure 6.7. The proportions of field lines of different classes, as a function of distance from the plates, averaged over seven different realizations of the magnetic field. Error bars are calculated from the dispersion of the different realizations at that point.

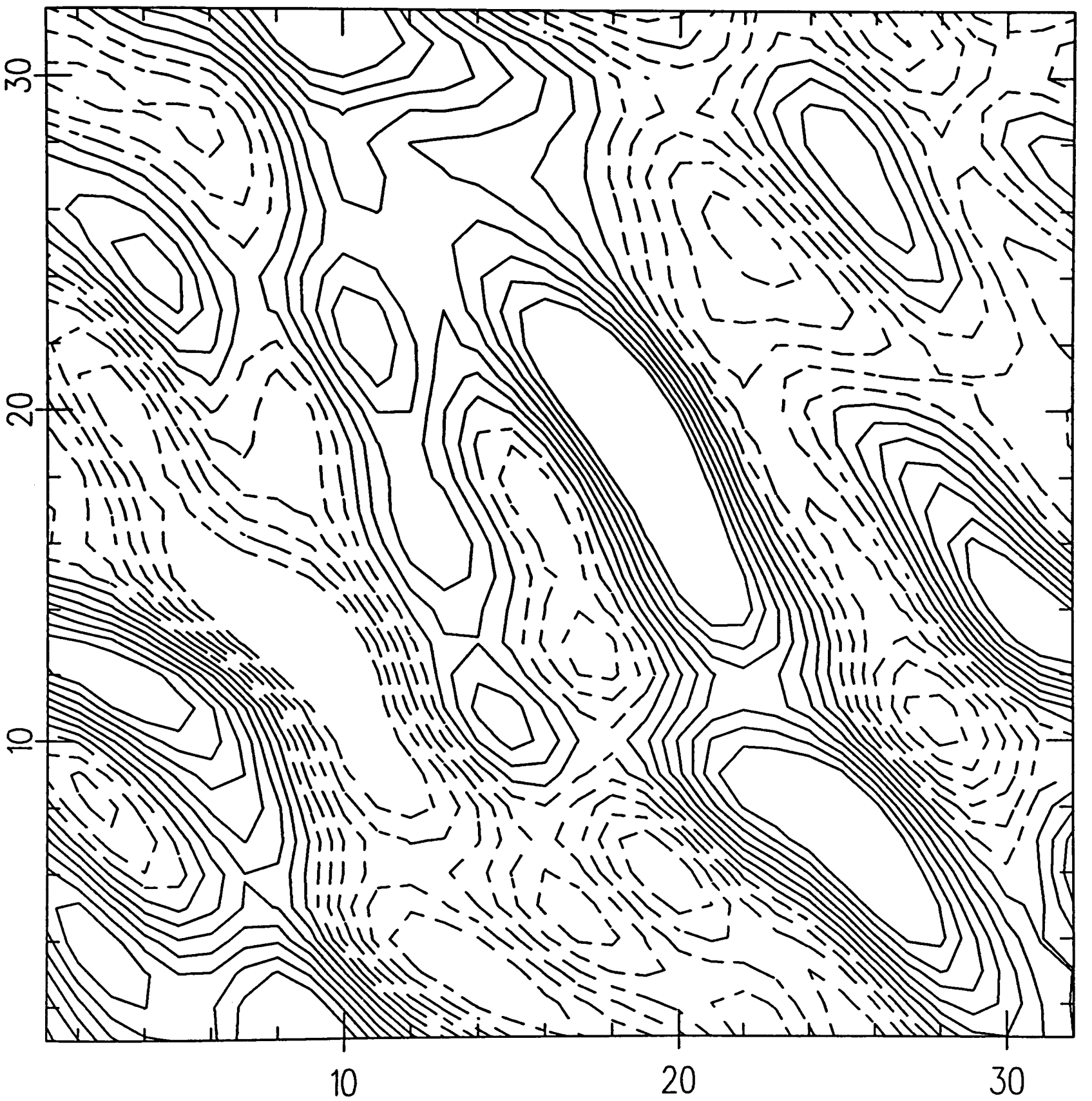

Figure 6.8. A typical synthesised RM map. The realization number is given at the top of the plot.

6.6 Discussion

In this chapter I have presented the first results of a study of real magnetic field lines. Much remains to be done.

The comparison with the results of Chapter 5 will be extended to examine how the heat flux scales with the step size and the size of the grid. In addition the temperature structure of the material between th plates will be calculated. The input power spectrum will be varied and the effect of this on the results noted.

Further work will be done on the relationship between the magnetic field power spectrum and the properties of the observed RM maps. The aim here is to see how much information about the initial magnetic field power spectrum remains in the RM distribution. This should help to give an estimate of the accuracy of the technique used in Chapter 4 to derive the magnetic field properties of cluster gas in Cygnus A.

The final aim is to incorporate magnetic fields in dynamic models of cooling flows. This will allow the accurate study of the evolution of an inhomogeneous intracluster medium.

Chapter 7. Summary

It is now time to collect the threads of argument running through this thesis and weave them together into a coherent whole. This is an opportunity to review progress and to see what remains to be done.

Since Mathews & Bregman (1978) proposed that the observed optical filaments in clusters formed from thermally unstable gas, much effort has been expended on studying the evolution of perturbations of the hot gas. Two recent developments have altered this picture. Malagoli, Rosner & Bodo (1987) pointed out that an overdense parcel of gas would oscillate about a mean position in the cluster, reducing the growth rate. Much more sophisticated Lagrangian analyses followed (Balbus 1988; Tribble 1989a; Balbus & Soker 1989a) which came to a different conclusion—cluster gas is much more thermally stable than was previously thought. Physically, this is because not only does the gas oscillate about a mean position, but the mean position can (and will) itself move. The correct measure of stability is relative to the moving mean position. Optical filaments do not come from thermally unstable material and their origin must be sought elsewhere. It has also become obvious that the stability (or otherwise) of a stratified atmosphere is a much more difficult problem than is usually appreciated.

The structure of the oscillation modes can be described simply. At large radii or high frequencies all waves are sound waves. Internal gravity waves are found at small radii and low frequencies. For intermediate radii and frequencies a damping zone is found. A given mode (of fixed frequency) is of different character at different places in the cluster.

The time dependent gravitational potential from oscillating central galaxies (such as cD's), and central binary galaxies, excites waves in cluster gas. The power involved is only a small fraction of the X-ray luminosity of a cluster and doesn't

constitute a large drain on the energy resources of the exciting galaxy or galaxies. Due to their small propagation velocities, g-waves near the centres of clusters can still be excited to nonlinear amplitudes. Optical filaments might arise from the evolution of these nonlinear structures. Even if nonlinear g-waves are not responsible for the filaments directly, any filaments that are formed will be pushed around by the gas, leading to the observed large spread in filament velocities.

I studied the excitation of sound waves in the simplest approximation. Excitation of g-waves should be resonant because the g-wave frequency and galaxy oscillation frequencies are very similar. This is a much more complicated problem than the one I have considered. My simple calculation shows that the amplitudes of the excited waves are large and that wave excitation deserves further study.

The general conclusion following from this work is that intracluster gas is subject to a barrage of waves of all kinds. Conductive damping of these waves is effective for short wavelengths (a few kpc) and is ineffective for long wavelength oscillations which will propagate to large radii. This damping is a heat source for the gas. Energy is preferentially deposited in hot gas, leading to instability.

Having studied waves in cluster gas, I then went on to look at magnetic fields in clusters. I presented strong evidence that magnetic fields of strengths a few μG coherent on length scales $\sim 10\,\mathrm{kpc}$ were common in clusters.

Resolved observations of the rotation measure of Cygnus A show a variation of magnetic field properties with radius in the cluster that is broadly consistent with flux freezing in a cooling flow. Magnetized gaseous halos like that around Cygnus A explain the depolarization asymmetry found in double radio sources.

The presence of a weak tangled magnetic field was then shown to have important consequences for the thermal structure of cluster gas. Heat can only flow easily along the field. Because the field lines do not follow direct routes between hot and

cold gas, global heat flow is reduced. Because the field is tangled and conductivity is effectively zero perpendicular to the field, neighbouring field lines will have different temperature. Thus the reduction of large scale heat flow and the gas being inhomogeneous are inevitable consequences of a tangled magnetic field.

Random walks were used to describe field lines. This was shown to be a reasonable approximation by constructing realizations of a magnetic field and studying the properties of the field lines.

Much more remains to be done on both the study of oscillations and magnetic fields in clusters. I have shown that both play an important rôle in the structure and evolution in clusters. Further study (both have been somewhat neglected in the past) will amply repay the effort invested.

More accurate calculations of wave excitation by galaxies, and by infalling groups, will lead to a better understanding of the velocity fields in cluster gas. Of particular interest is the excitation of g-waves by a cD galaxy. The infall of a group and the assimilation of a subcluster are also important sources of wave energy due to the large mass involved.

Further studies of the evolution of waves of nonlinear amplitudes will show whether this process can lead to the observed optical filaments.

Much of interest remains to be done on the study of real magnetic fields. The characterization of the field lines (by some sort of fractal dimension) and the relation to Hamiltonian dynamics are two obvious areas for future work.

The effects of tangled magnetic fields on the gas should be studied with more realistic fields, and the evolution of an inhomogeneous intracluster medium should be further investigated. This will take us one step closer to a complete description of the state of the intracluster medium.

References

Abell, G.O., 1958. *Astrophys. J. Suppl.,* **3**, 211.

Andreasyan, R.R., 1986. *Astrophysics,* **24**, 213.

Arnaud, K.A., Fabian, A.C., Eales, S.A., Jones, C., & Forman, W., 1984. *Mon. Not. R. astr. Soc.,* **211**, 981.

Balbus, S.A., 1986. *Astrophys. J.,* **303**, L79.

Balbus, S.A., 1988. *Astrophys. J.,* **328**, 395.

Balbus, S.A., & Soker, N., 1989a. *Astrophys. J.,* **341**, 611.

Balbus, S.A., & Soker, N., 1989b. Preprint.

Barthel, P.D., 1989. *Astrophys. J.,* **336**, 606.

Batchelor, G.K., 1953. *The theory of homogeneous turbulence.* Cambridge University Press, Cambridge.

Bautz, L.P., & Morgan, W.W., 1970. *Astrophys. J.,* **162**, L149.

Bertschinger, E., & Meiksin, A., 1986. *Astrophys. J.,* **306**, L1.

Bicknell, G.V., Cameron, R.A, & Gingold, R.A., 1989. Preprint.

Binney, J.J., 1988. In: *Cooling Flows in Clusters and Galaxies,* p.225, ed. Fabian, A.C., Kluwer, Dordrecht.

Binney, J.J., & Cowie, L.L., 1981. *Astrophys. J.,* **247**, 464.

Bower, R.G., Ellis, R.S., & Efstathiou, G., 1988. *Mon. Not. R. astr. Soc.,* **234**, 725.

Bregman, J.N., & David, L.P., 1988. *Astrophys. J.,* **326**, 639.

Bregman, J.N., & David, L.P., 1989. *Astrophys. J.,* **341**, 49.

Burn, B.J., 1966. *Mon. Not. R. astr. Soc.,* **133**, 67.

Byram, E.T., Chubb, T.A., & Friedman, H., 1966. *Science,* **152**, 66.

Canizares, C.R., Markert, T.H., & Donahue, M.E., 1988. In: *Cooling Flows in Clusters and Galaxies,* p.63, ed. Fabian, A.C., Kluwer, Dordrecht.

Carilli, C.L., Perley, R.A., & Dreher, J.W., 1988. *Astrophys. J.,* **334**, L73.

Cavaliere, A., Gursky, H., & Tucker, W.H., 1971. *Nature,* **231**, 437.

Cioffi, D.F., & Jones, T.W., 1980. *Astron. J.,* **85**, 368.

Cowie, L.L., Fabian, A.C., & Nulsen, P.E.J., 1980. *Mon. Not. R. astr. Soc.,* **191**, 399.

Cowie, L., Hu, E., Jenkins, E., & York, D., 1983. *Astrophys. J.,* **272**, 29.

Cowie, L.L., & McKee, C.F., 1977. *Astrophys. J.,* **211**, 135.

Cox, D.R., & Miller, H.D., 1965. *The Theory of Stochastic Processes,* Methuen London.

Cox, J.P., 1980. *Theory of Stellar Pulsation,* Princeton: Princeton University Press.

Crawford, C.S., & Fabian, A.C., 1989. *Mon. Not. R. astr. Soc.,* **239**, 219.

Dennison, B., 1980. *Astrophys. J.,* **239**, L93.

Dreher, J.W., Carilli, C.L., & Perley, R.A., 1987. *Astrophys. J.,* **316**, 611.

Fabian, A.C., Nulsen, P.E.J., & Arnaud, K.A., 1984. *Mon. Not. R. astr. Soc.,* **208**, 179.

Fabian, A.C., Nulsen, P.E.J., & Canizares, C.R., 1984. *Nature,* **310**, 733.

Feller, W., 1950. *An Introduction to Probability theory and its Applications, 3rd ed., Vol. I.* Wiley.

Field, G.B., 1965. *Astrophys. J.,* **142**, 531.

Fitchett, M.J., 1988. In: *Large Scale Structure and Its Relation o Clusters of Galaxies*, Minnesota Astrophysics Lecture Series.

Forman, W., & Jones, C., 1982. *Ann. Rev. Astr. Astrophys.*, **20**, 547.

Forman, W., Jones, C., Cominsky, L., Julien, P., Murray, S., Peters, G., Tananbaum, H., & Giacconi, R., 1978. *Astrophys. J. Suppl.*, **38**, 357.

Forman, W., Jones, C., & Tucker, W., 1985. *Astrophys. J.*, **293**, 102.

Gardner, F.F., & Whiteoak, J.B., 1966. *Ann. Rev. Astr. Astrophys.*, **4**, 245.

Garrington, S.T., 1988. In: *Cooling Flows in Clusters and Galaxies*, p.209, ed. Fabian, A.C., Kluwer, Dordrecht.

Garrington, S.T., Leahy, J.P., Conway, R.G., & Laing, R.A., 1988. *Nature*, **331**, 147.

Geller, M.J., & Beers, T.C., 1982. *Publs astr. Soc. Pacific.*, **94**, 421.

Giacconi, R., Murray, S., Gursky, H., Kellogg, E., Schreier, E., & Tananbaum, H., 1972. *Astrophys. J.*, **178**, 281.

Giacconi, R., Murray, S., Gursky, H., Kellogg, E., Schreier, E., Matilsky, T., Koch, D., & Tananbaum, H., 1974. *Astrophys. J. Suppl.*, **27**, 37.

Giacconi, R., *et al.* 1979. *Astrophys. J.*, **230**, 540.

Gradshteyn, I.S., & Ryzhik, I.M., 1980. *Tables of Integrals, Series and Products*, Academic Press, New York.

Gull, S.F., & Northover, K.J., 1973. *Nature*, **244**, 80.

Haas, F.A., & Thyagaraja, A., 1986. *Phys. Reports*, **143**, 241.

Hanisch, R.J., 1987. In: *Radio Continuum Processes in Clusters of Galaxies*, NRAO Workshop No. 16. p.191.

Heckman, T.M., 1981. *Astrophys. J.*, **250**, L59.

Heckman, T.M., Baum, S.A., van Breugel, W.J.M., & McCarthy, P., 1989. *Astrophys. J.*, **338**, 48.

Hill, J.M., Hintzen, P., Oegerle, W.R., Romanishin, W., Lesser, M.P., Eisenhamer, J.D., & Batuski, D.J., 1988. *Astrophys. J.*, **332**, L23.

Jackson, J.D., 1975. *Classical Electrodynamics,* Wiley, New York.

Jaffe, W., 1977. *Astrophys. J.*, **212**, 1.

Jaffe, W., 1980. *Astrophys. J.*, **241**, 925.

Jokipii, J.K., & Parker, E.N., 1969. *Astrophys. J.*, **155**, 777.

Jordan, C., Ayres, T.R., Brown, A., Linsky, J.L., & Simon, T., 1987. *Mon. Not. R. astr. Soc.*, **225**, 903.

Killeen, N.E.B., Bicknell, G.V., & Ekers, R.D., 1986. *Astrophys. J.*, **302**, 306.

Kim, K.-T., & Kronberg, P.P., 1989. Preprint.

Kim, K-T., Kronberg, P.P., Dewdney, P.E., & Landecker, T.L., 1987. In: *Radio Continuum Processes in Clusters of Galaxies,* NRAO Workshop No. 16. p.199.

Kim, K-T., Kronberg, P.P., Dewdney, P.E., & Landecker, T.L., 1989. Preprint.

Kronberg, P.P., & Simard-Normandin, M., 1976. *Nature,* **263**, 653.

Landau, L.D., & Lifshitz, E.M., 1959. *Fluid Mechanics,* Pergamon Press, Oxford.

Laing, R.A., 1981. *Mon. Not. R. astr. Soc.*, **193**, 439.

Laing, R.A., 1988. *Nature,* **331**, 149.

Laing, R.A., & Bridle, A.H., 1987. *Mon. Not. R. astr. Soc.*, **228**, 557.

Lawler, J.M., & Dennison, B., 1982. *Astrophys. J.*, **252**, 81.

Leahy, J.P., 1984. *Mon. Not. R. astr. Soc.*, **208**, 323.

Leahy, J.P., 1987. *Mon. Not. R. astr. Soc.,* **226**, 433.

Leahy, J.P., Jägers, W.J., & Pooley, G.G., 1986. *Astr. Astrophys.,* **156**, 234.

Leahy, J.P., Pooley, G.G., & Riley, J.M., 1986. *Mon. Not. R. astr. Soc.,* **222**, 753.

Lynds, R., 1970. *Astrophys. J.,* **159**, L151.

Lynden-Bell, D., & Ostriker, J.P., 1967. *Mon. Not. R. astr. Soc.,* **136**, 293.

Malagoli, A., Rosner, R., & Bodo, G., 1987. *Astrophys. J.,* **319**, 632.

Mathews, W.G., & Bregman, J.N., 1978. *Astrophys. J.,* **224**, 308.

Matthews, T.A., Morgan, W.W., & Schmidt, M., 1964. *Astrophys. J.,* **140**, 35.

McHardy, I.M., Stewart, G.C., Edge, A.C., Cooke, B.A., Yamashita, K., & Hatsukade, I., 1989. Preprint.

McKee, C.F., & Cowie, L.L., 1977. *Astrophys. J.,* **215**, 213.

Meiksin, A., 1988. In: *Cooling Flows in Clusters and Galaxies,* p.47, ed. Fabian, A.C., Kluwer, Dordrecht.

Miller, L., 1986. *Mon. Not. R. astr. Soc.,* **220**, 713.

Mitchell, R.J., & Mushotzky, R.F., 1980. *Astrophys. J.,* **236**, 730.

Mitchell, R.J., Culhane, J.L., Davison, P.J., & Ives, J.C., 1976. *Mon. Not. R. astr. Soc.,* **175**, 29p.

Mitchell, R.J., Dickens, R.J., Bell Burnell, S.J., & Culhane, J.L., 1979. *Mon. Not. R. astr. Soc.,* **189**, 329.

Mushotzky, R.F., 1984. *Phys. Scripta,* **T7**,157.

Mushotzky, R.F., 1985. In: *Proceedings of the Conference on Non-Thermal and Very High Temperature Phenomena in X-ray Astronomy.* ed. Perola, G., & Salvati, M.

Mushotzky, R.F., & Szymkowiak, A.E., 1988. In: *Cooling Flows in Clusters and Galaxies,* p.53, ed. Fabian, A.C., Kluwer, Dordrecht.

Mushotzky, R.F., Serlemitsos, P.J., Smith, B.W., Boldt, E.A., & Holt, S.S., 1978. *Astrophys. J.*, **225**, 21.

Nulsen, P.E.J., 1986. *Mon. Not. R. astr. Soc.*, **221**, 377.

Nulsen, P.E.J., 1988. In: *Cooling Flows in Clusters and Galaxies,* p.175, ed. Fabian, A.C., Kluwer, Dordrecht.

O'Dea, C.P., & Owen, F.N., 1986. *Astrophys. J.*, **301**, 841.

O'Dea, C.P., & Owen, F.N., 1987. *Astrophys. J.*, **316**, 95.

Pallister, I.C., 1987. *D.Phil. Thesis,* Oxford University.

Patnaik, A.R., Malkan, M.A., & Salter, C.J., 1986. *Mon. Not. R. astr. Soc.*, **220**, 351.

Pedelty, J.A., Rudnick, L., McCarthy, P.J., & Spinrad, H., 1989. *Astron. J.*, **97**, 647.

Perley, R.A., 1989. In: *IAU Symposium 140: Galactic and Extragalactic Magnetic Fields.*

Perley, R.A., Bridle, A.H., & Willis, A.G., 1984. *Astrophys. J. Suppl.*, **54**, 291.

Press, W.H., Flannery, B.P., Teukolsky, S.A., & Vetterling, W.T., 1986. *Numerical Recipes: The Art of Scientific Computing*, Cambridge: Cambridge University Press.

Quintana, H., & Lawrie, D.G., 1982. *Astron. J.*, **87**, 1.

Radhakrishnan, V., 1989. *Q. Jl R. astr. Soc.*, **30**, 181.

Raymond, J.C., Cox, D.P., & Smith, B.W., 1976. *Astrophys. J.*, **204**, 290.

Rechester, A.B., & Rosenbluth, M.N., 1978. *Phys. Rev. Lett.*, **40**, 38.

Rephaeli, Y., & Gruber, D.E., 1988. *Astrophys. J.*, **333**, 133.

Rephaeli, Y., & Wandel, A., 1985. *Mon. Not. R. astr. Soc.*, **215**, 453.

Roland, J., 1981. *Astr. Astrophys.*, **93**, 407.

Rood, H.J., & Sastry, G.N., 1972. *Astron. J.*, **77**, 451.

Ruzmaikin, A.A., & Sokoloff, D.D., 1979. *Astr. Astrophys.*, **78**, 1.

Saikia, D.J., & Salter, C.J., 1988. *Ann. Rev. Astr. Astrophys.*, **26**, 93.

Sarazin, C.L., 1986. *Rev. Mod. Phys.*, **58**, 1.

Sarazin, C.L., 1987. In: *Radio Continuum Processes in Clusters of Galaxies,* NRAO Workshop No. 16. p.23.

Shapiro, S.L., & Teukolsky, S.A., 1983. *Black Holes, White dwarfs and Neutron Stars,* New York: Wiley-Interscience.

Sharples, R.M., Ellis, R.S., & Gray, P.M., 1988. *Mon. Not. R. astr. Soc.*, **231**, 479.

Silk, J., Djorgovski, S., Wyse, R.F., & Bruzual, A.G., 1986. *Astrophys. J.*, **307**, 415.

Silk, J., & White, S.D.M., 1978. *Astrophys. J.*, **226**, L103.

Simard-Normandin, M. & Kronberg, P.P., 1980. *Astrophys. J.*, **242**, 74.

Simonetti, J.H. & Cordes, J.M., 1986. *Astrophys. J.*, **310**, 160.

Simonetti, J.H., Cordes, J.M., & Spangler, S.R., 1984. *Astrophys. J.*, **284**, 126.

Soker, N., & Sarazin, C.L., 1988. In: *Cooling Flows in Clusters and Galaxies,* p.367, ed. Fabian, A.C., Kluwer, Dordrecht.

Spitzer, L., Jr., 1962. *Physics of Fully Ionized Gases,* New York: Interscience.

Stewart, G.C., Canizares, C.R., Fabian, A.C., & Nulsen, P.E.J., 1984. *Astrophys. J.*, **278**, 536.

Struble, M.F., & Rood, H.J., 1982. *Astron. J.*, **87**, 7.

Struble, M.F., & Rood, H.J., 1984. *Astron. J.*, **89**, 1487.

Takahara, M., & Takahara, F., 1979. *Prog. Theoretical Phys.*, **62**, 1253.

Thomas, P.A., 1988. In: *Cooling Flows in Clusters and Galaxies*, p.361, ed. Fabian, A.C., Kluwer, Dordrecht.

Thomas, P.A., Fabian, A.C., Arnaud, K.A., Forman, W., & Jones, C., 1986. *Mon. Not. R. astr. Soc.*, **222**, 655.

Thomas, P.A., Fabian, A.C., & Nulsen, P.E.J., 1987. *Mon. Not. R. astr. Soc.*, **228**, 973.

Tribble, P.C., 1989a. *Mon. Not. R. astr. Soc.*, **238**, 1.

Tribble, P.C., 1989b. *Mon. Not. R. astr. Soc.*, **238**, 1247.

Tucker, W.H., & Rosner, R., 1983. *Astrophys. J.*, **267**, 547.

Vallée, J.P., Macleod, J.M., & Broten, N.W., 1986. *Astr. Astrophys.*, **156**, 386.

Vallée, J.P., 1989. *Astrophys. Sp. Sci.*, **152**, 9.

Vestrand, W.T., 1982. *Astron. J.*, **87**, 1266.

White, R.E. III, & Sarazin, C.L., 1987. *Astrophys. J.*, **318**, 612.

De Young, D.S., Hogg, D.E., & Wilkes, C.T., 1979. *Astrophys. J.*, **228**, 43.

Zwicky, F., Herzog, E., Wild, P., Karpowicz, M., & Kowal, C.T., 1961-1968. *Catalogue of Galaxies and Clusters of Galaxies*, Vols. 1-6. Caltech: Pasadena.

Appendix 2: Self-Adjoint nature of the Oscillation Equations

Considering equation (2.36), assume a time dependence of the form $e^{-i\omega t}$, and consider the overlap between two different wavefunctions by forming the quantity

$$
\begin{aligned}
&(\omega^2-(\omega'^*)^2)\int \boldsymbol{\xi}.\boldsymbol{\xi}'^*\rho\, d^3\mathbf{r} \\
&\quad=\int\{-\boldsymbol{\xi}'^*.\nabla\{\boldsymbol{\xi}.\nabla P+\gamma P\nabla.\boldsymbol{\xi}\}+\boldsymbol{\xi}.\nabla\{\boldsymbol{\xi}'^*.\nabla P+\gamma P\nabla.\boldsymbol{\xi}'^*\} \\
&\qquad+\frac{\boldsymbol{\xi}'^*.\nabla P\,\nabla.(\rho\boldsymbol{\xi})}{\rho}-\frac{\boldsymbol{\xi}.\nabla P\,\nabla.(\rho\boldsymbol{\xi}'^*)}{\rho} \\
&\qquad+\rho\boldsymbol{\xi}'^*.\nabla\delta\Phi-\rho\boldsymbol{\xi}.\nabla\delta\Phi'^*\}\,d^3\mathbf{r} \\
&\quad=\int\{\nabla.\boldsymbol{\xi}'^*(\boldsymbol{\xi}.\nabla P+\gamma P\nabla.\boldsymbol{\xi})-\nabla.\boldsymbol{\xi}(\boldsymbol{\xi}'^*.\nabla P+\gamma P\nabla.\boldsymbol{\xi}'^*) \\
&\qquad+\frac{\boldsymbol{\xi}'^*.\nabla P\,\boldsymbol{\xi}.\nabla\rho}{\rho}-\frac{\boldsymbol{\xi}.\nabla P\,\boldsymbol{\xi}'^*.\nabla\rho}{\rho} \\
&\qquad+\boldsymbol{\xi}'^*.\nabla P\,\nabla.\boldsymbol{\xi}-\boldsymbol{\xi}.\nabla P\,\nabla.\boldsymbol{\xi}'^*\}\,d^3\mathbf{r} \\
&\qquad-G\int\left\{\boldsymbol{\xi}'^*.\nabla_{\mathbf{r}}\int\rho(\mathbf{r}')\boldsymbol{\xi}(\mathbf{r}').\nabla_{\mathbf{r}'}\frac{1}{|\mathbf{r}-\mathbf{r}'|}\,d^3\mathbf{r}'\right. \\
&\qquad\left.-\boldsymbol{\xi}.\nabla_{\mathbf{r}}\int\rho(\mathbf{r}')\boldsymbol{\xi}'^*(\mathbf{r}').\nabla_{\mathbf{r}'}\frac{1}{|\mathbf{r}-\mathbf{r}'|}\,d^3\mathbf{r}'\right\}\rho\,d^3\mathbf{r} \\
&\quad=\int\left\{\frac{\boldsymbol{\xi}'^*.\nabla P\,\boldsymbol{\xi}.\nabla\rho}{\rho}-\frac{\boldsymbol{\xi}.\nabla P\,\boldsymbol{\xi}'^*.\nabla\rho}{\rho}\right\}d^3\mathbf{r} \\
&\qquad-G\iint\left\{\rho(\mathbf{r})\xi_i'^*(\mathbf{r})\rho(\mathbf{r}')\xi_j(\mathbf{r}')\nabla_{\mathbf{r}_i}\nabla_{\mathbf{r}'_j}\frac{1}{|\mathbf{r}-\mathbf{r}'|}-(\mathbf{r}\leftrightarrow\mathbf{r}')\right\}d^3\mathbf{r}\,d^3\mathbf{r}' \\
&\quad=\int(\xi_r'^*\xi_r-\xi_r\xi_r'^*)\,\nabla_r P\,\nabla_r\rho\frac{1}{\rho}\,d^3\mathbf{r} \\
&\quad=0.
\end{aligned}
$$

Here divergence terms have been turned into surface terms that vanish at infinity, and the background is assumed to be spherically symmetric. The gravitational term is zero because the integrands are symmetric in $\mathbf{r}$ and $\mathbf{r}'$.

This shows that the eigenfunctions corresponding to different eigenvalues are orthogonal, and that the eigenvalues themselves are real. This establishes the self-adjoint nature of the nonradial system of equations, although they are not of Sturm-Liouville form.

Appendix 3: Evaluation of Emission Integrals

In Chapter 3 we need to evaluate integrals of the form

$$I = \int_0^\pi d\theta' \sin^p \theta' \cos^q \theta' \exp(-i\alpha \cos\theta \cos\theta') J_\nu(\alpha \sin\theta \sin\theta'), \qquad (A3.1)$$

Where $\alpha = kr'$.

The exponential and Bessel function are expanded as power series:

$$e^x = \sum_{n=0}^{\infty} \frac{x^n}{n!}, \qquad (A3.2)$$

$$J_\nu(x) = \sum_{m=0}^{\infty} \frac{(-1)^m}{m!(m+\nu)!} \left(\frac{x}{2}\right)^{2m+\nu}. \qquad (A3.3)$$

Therefore,

$$I = \int_0^\pi d\theta' \sin^p \theta' \cos^q \theta' \times \sum_{n=0}^{\infty} \sum_{m=0}^{\infty} \frac{(-i\alpha \cos\theta \cos\theta')^n}{n!} \frac{(-1)^m}{m!(m+\nu)!} \left(\frac{\alpha \sin\theta \sin\theta'}{2}\right)^{2m+\nu}. \qquad (A3.4)$$

We can now do the integral, using the result

$$\int_0^{\pi/2} \cos^r \theta \sin^s \theta \, d\theta = \frac{1}{2} \frac{\Gamma([r+1]/2)\Gamma([s+1]/2)}{\Gamma([r+s+2]/2)}, \qquad (A3.5)$$

to get

$$I = \sum_{n=0}^{\infty} \sum_{m=0}^{\infty} \frac{(-i\alpha \cos\theta)^n}{n!} \frac{(-1)^m}{m!(m+\nu)!} \left(\frac{\alpha \sin\theta}{2}\right)^{2m+\nu} \times \frac{\Gamma([q+n+1]/2)\Gamma([p+\nu+2m+1]/2)}{\Gamma([q+n+p+\nu+2m+2]/2)}, \qquad (A3.6)$$

with the summation restricted to $n+q$ even. I now evaluate this for the cases of interest.

A3.1 Oscillating central galaxy: dipole field

In this case we have $p = 1$, $q = 1$, and $\nu = 0$. The summation is over odd values of n only, so we can replace a restricted sum over n by a full sum over $2n + 1$, leaving

$$I = \sum_{n=0}^{\infty}\sum_{m=0}^{\infty} \frac{(-i\alpha\cos\theta)^{2n+1}}{(2n+1)!}\frac{(-1)^m}{m!m!}\left(\frac{\alpha\sin\theta}{2}\right)^{2m}\frac{\Gamma(n+3/2)\Gamma(m+1)}{\Gamma(n+m+5/2)}$$
$$= \sum_{n=0}^{\infty}\sum_{m=0}^{\infty} \frac{-i(\alpha\cos\theta)^{2n+1}}{(2n+1)!}\frac{(-1)^{n+m}}{m!}\left(\frac{\alpha\sin\theta}{2}\right)^{2m}\frac{\Gamma(n+3/2)}{\Gamma(n+m+5/2)}. \quad (A3.7)$$

The relation

$$\Gamma(2x) = \frac{2^{2x-1}}{\sqrt{\pi}}\Gamma(x)\Gamma(x+1/2) \quad (A3.8)$$

can be used to simplify the remaining gamma functions, leaving

$$I = \sum_{n=0}^{\infty}\sum_{m=0}^{\infty} \frac{-4i(\alpha\cos\theta)^{2n+1}}{(2n+1)!}\frac{(-1)^{n+m}}{m!}(\alpha\sin\theta)^{2m}\frac{\Gamma(2n+2)\Gamma(m+n+2)}{\Gamma(n+1)\Gamma(2n+2m+4)}$$
$$= -4i\cos\theta\sum_{n=0}^{\infty}\sum_{m=0}^{\infty}\alpha^{2(n+m)+1}\frac{(\cos^2\theta)^n(\sin^2\theta)^m}{n!m!}(-1)^{n+m}\frac{\Gamma(m+n+2)}{\Gamma(2[n+m]+4)}. \quad (A3.9)$$

We now change the order of the summation. We sum over m (or n) at constant $N = n + m$, and then sum over N. The sum over m is then just the binomial expansion of $\cos^2\theta + \sin^2\theta$. So

$$I = -4i\cos\theta\sum_{N=0}^{\infty}(-1)^N\alpha^{2N+1}\frac{(N+1)!}{N!(2N+3)!}. \quad (A3.10)$$

This can be compared with the power series for the spherical Bessel functions

$$j_\mu(x) = 2^\mu\sum_{N=0}^{\infty}\frac{(-1)^N(N+\mu)!}{(2N+2\mu+1)!N!}x^{2N+\mu}, \quad (A3.11)$$

and is observed to agree for $\mu = 1$. Therefore

$$I = -2i\cos\theta j_1(\alpha). \quad (A3.12)$$

A3.2 Oscillating central galaxy: quadrupole field

The quadrupole field has an angular dependence $P_2(\cos\theta') = \cos^2\theta' - (1/2)\sin^2\theta'$. There are therefore two integrals, one with $p = 3$, $q = 0$, the other with $p = 1$, $q = 2$, and both with $\nu = 0$. Therefore the sum is over even n only, and we can replace this by a sum over $2n$,

$$I = \sum_{n=0}^{\infty}\sum_{m=0}^{\infty} \frac{(-i\alpha\cos\theta)^{2n}}{(2n)!}\frac{(-1)^m}{m!m!}\left(\frac{\alpha\sin\theta}{2}\right)^{2m} \times \left[\frac{\Gamma([2n+3]/2)\Gamma([2m+2]/2)}{\Gamma([2n+2m+5]/2)} - \frac{\Gamma([2n+1]/2)\Gamma([2m+4]/2)}{2\Gamma([2n+2m+5]/2)}\right]. \quad (A3.13)$$

This simplifies to

$$I = \sum_{n=0}^{\infty}\sum_{m=0}^{\infty} \frac{(\cos^2\theta)^n(\sin^2\theta)^m}{(2n)!}\frac{(-1)^{n+m}\alpha^{2(n+m)}}{2^{2m}m!m!\Gamma([2n+2m+5]/2)} \times \left[\Gamma(n+3/2)\Gamma(m+1) - \frac{1}{2}\Gamma(n+1/2)\Gamma(m+2)\right]. \quad (A3.14)$$

The doubling formula, equation (A3.8), can be used to simplify the gamma functions, leaving

$$I = \sum_{n=0}^{\infty}\sum_{m=0}^{\infty}(\cos^2\theta)^n(\sin^2\theta)^m \frac{(-1)^{n+m}\alpha^{2(n+m)}8(n+m+1)!}{(2n+2m+3)!} \times \left[\frac{n}{n!m!} - \frac{m}{2m!n!}\right], \quad (A3.15)$$

which is, changing the order of summation

$$I = 8\sum_{N=1}^{\infty}\frac{(-1)^N\alpha^{2N}(N+1)!}{(2N+3)!}\left[\frac{\cos^2\theta - (1/2)\sin^2\theta}{(N-1)!}\right] = -2P_2(\cos\theta)j_2(\alpha). \quad (A3.16)$$

A3.3 Binary Galaxy

Here we have $p = 3$, $q = 0$, and $\nu = 2$. We again replace a restricted sum over even values of n by a full sum over $2n$

$$I = \sum_{n=0}^{\infty}\sum_{m=0}^{\infty} \frac{(-i\alpha\cos\theta)^{2n}}{(2n)!}\frac{(-1)^m}{m!(m+2)!}\left(\frac{\alpha\sin\theta}{2}\right)^{2m+2}\frac{\Gamma(n+1/2)\Gamma(m+3)}{\Gamma(n+m+3+1/2)}$$
$$= \sum_{n=0}^{\infty}\sum_{m=0}^{\infty} \frac{(\alpha\cos\theta)^{2n}}{(2n)!}\frac{(-1)^{m+n}}{m!}\left(\frac{\alpha\sin\theta}{2}\right)^{2m+2}\frac{\Gamma(n+1/2)}{\Gamma(n+m+3+1/2)}. \quad (A3.17)$$

We can again use equation (A3.8) to eliminate $(2n)!$ and simplify the gamma functions, leading to

$$I = \sum_{n=0}^{\infty}\sum_{m=0}^{\infty} \frac{(-1)^{m+n}}{2^{2n+2m+2}}\alpha^{2n+2m+2}\sin^2\theta\frac{(\cos^2\theta)^n(\sin^2\theta)^m}{m!n!}\frac{2^{2n+2m+5}\Gamma(n+m+3)}{\Gamma(2[n+m+3])}$$
$$= 8\sin^2\theta\sum_{n=0}^{\infty}\sum_{m=0}^{\infty}(-1)^{m+n}\alpha^{2n+2m+2}\frac{(\cos^2\theta)^n(\sin^2\theta)^m}{m!n!}\frac{(n+m+2)!}{(2n+2m+5)!}. \quad (A3.18)$$

Again changing the order of summation,

$$I = 8\sin^2\theta\sum_{N=0}^{\infty}(-1)^N\alpha^{2N+2}\frac{(N+2)!}{N!(2N+5)!}$$
$$= 2\sin^2\theta j_2(\alpha). \quad (A3.19)$$

Appendix 5A: The Correlated Random Walk

Consider the situation in which the probability of making a step in a particular direction depends on the direction of the previous step. This can be expressed either by the conditional probabilities

$$\begin{aligned} \mathrm{P}(+\mid +) &= \alpha \qquad \mathrm{P}(+\mid -) = \beta \\ \mathrm{P}(-\mid +) &= \beta \qquad \mathrm{P}(-\mid -) = \alpha \end{aligned} \tag{5.13}$$

or by the correlation coefficient between two successive steps

$$\langle \Delta_i \Delta_{i+1} \rangle = c. \tag{A5.1}$$

Although only successive steps are correlated this induces a correlation of c^n between displacements n steps apart. These two ways of expressing the correlation are related by

$$\alpha = \frac{1+c}{2} \quad ; \quad \beta = \frac{1-c}{2}. \tag{A5.2}$$

We may consider the limit as $c \to 1$ and the step length s vanishes. Then

$$c^n \to e^{-L/L_c}$$

where

$$L = ns \quad \text{(constant)}; \qquad L_c = \frac{s}{1-c}.$$

The probability of winning (losing) starting from point k when the preceding step was up ($\uparrow$) is written as $P_k^{\uparrow}$ ($Q_k^{\uparrow}$). Then the following recurrence relations hold

$$\begin{aligned} P_k^{\uparrow} &= \alpha P_{k+1}^{\uparrow} + \beta P_{k-1}^{\downarrow} \\ P_k^{\downarrow} &= \beta P_{k+1}^{\uparrow} + \alpha P_{k-1}^{\downarrow} \\ Q_k^{\uparrow} &= \alpha Q_{k+1}^{\uparrow} + \beta Q_{k-1}^{\downarrow} \\ Q_k^{\downarrow} &= \beta Q_{k+1}^{\uparrow} + \alpha Q_{k-1}^{\downarrow}. \end{aligned} \tag{A5.3}$$

Symmetry dictates that $P_k^{\uparrow}$ is equal to $Q_{a-k}^{\downarrow}$, so that only P_k need be calculated. The boundary conditions on P_k are

$$P_0^{\downarrow} = 0 \quad ; \quad P_a^{\uparrow} = 1. \tag{A5.4}$$

There is no meaning to the expressions $P_0^{\uparrow}$ and $P_a^{\downarrow}$ since these involve points outside the sample space. It is easily verified that the solution to these equations is

$$\begin{aligned} P_k^{\uparrow} &= \frac{k\beta + (\alpha - \beta)}{a\beta + (\alpha - \beta)} \\ P_k^{\downarrow} &= \frac{k\beta}{a\beta + (\alpha - \beta)} \end{aligned} \tag{A5.5}$$

which reduces to the simple random walk result when α and β are identical.

We are interested in calculating the probabilities of winning at the nth step. Recurrence relations can again be given

$$\begin{aligned} P_{k,n}^{\uparrow} &= \alpha P_{k+1,n-1}^{\uparrow} + \beta P_{k-1,n-1}^{\downarrow} \\ P_{k,n}^{\downarrow} &= \beta P_{k+1,n-1}^{\uparrow} + \alpha P_{k-1,n-1}^{\downarrow}. \end{aligned} \tag{A5.6}$$

Generating functions $\mathbf{P}$ are defined by

$$\mathbf{P}_k^{\uparrow}(x) = \sum_n P_{k,n}^{\uparrow} x^n \tag{A5.7}$$

and similarly for $\mathbf{P}_k^{\downarrow}$. Multiplying the recurrence relations (A5.6) by x^n and summing over all n leads to recurrence relations for the generating functions $\mathbf{P}$

$$\begin{aligned} \mathbf{P}_k^{\uparrow}(x) &= x[\alpha \mathbf{P}_{k+1}^{\uparrow}(x) + \beta \mathbf{P}_{k-1}^{\downarrow}(x)] \\ \mathbf{P}_k^{\downarrow}(x) &= x[\beta \mathbf{P}_{k+1}^{\uparrow}(x) + \alpha \mathbf{P}_{k-1}^{\downarrow}(x)] \end{aligned} \tag{A5.8}$$

with the boundary conditions

$$\mathbf{P}_a^{\uparrow}(x) = 1 \quad ; \quad \mathbf{P}_0^{\downarrow} = 0. \tag{A5.9}$$

We may eliminate either $\mathbf{P}^{\uparrow}$ or $\mathbf{P}^{\downarrow}$ to give

$$\alpha x \mathbf{P}_{k+2}^{\uparrow}(x) - [1 + (\alpha - \beta)x^2]\mathbf{P}_{k+1}^{\uparrow}(x) + \alpha x \mathbf{P}_k^{\uparrow}(x) = 0 \tag{A5.10}$$

with an identical equation for $\mathbf{P}^{\downarrow}$. To solve this equation we look for a solution of the form $\mathbf{P}_k \sim w^k$, where w satisfies

$$\alpha x w^2(x) - [1 + (\alpha - \beta)x^2]w(x) + \alpha x = 0 \qquad (A5.11)$$

which has two solutions

$$w_{\pm}(x) = \frac{[1 + (\alpha - \beta)x^2] \pm \sqrt{[1 + (\alpha - \beta)x^2]^2 - 4\alpha^2 x^2}}{2\alpha x}. \qquad (A5.12)$$

The general solution is

$$\begin{aligned} \mathbf{P}_k^{\uparrow}(x) &= A' w_+^k(x) + B' w_-^k(x) \\ \mathbf{P}_k^{\downarrow}(x) &= C' w_+^k(x) + D' w_-^k(x). \end{aligned} \qquad (A5.13)$$

The coefficients are determined by using the recurrence relations and the boundary conditions. Before doing this it is convenient to change variables from x to ϕ where

$$w_{\pm} = e^{\pm i\phi} \quad ; \quad \cos\phi \equiv \frac{[1 + (\alpha - \beta)x^2]}{2\alpha x} \qquad (A5.14)$$

so that

$$\begin{aligned} \mathbf{P}_k^{\uparrow} &= A \sin k\phi + B \cos k\phi \\ \mathbf{P}_k^{\downarrow} &= C \sin k\phi + D \cos k\phi. \end{aligned} \qquad (A5.15)$$

The boundary conditions lead to the two conditions

$$A \sin a\phi + B \cos a\phi = 1 \quad ; \quad D = 0. \qquad (A5.16)$$

Taking the ratio between the two equations (A5.8) leads to a quadratic form in $\cos k\phi$ and $\sin k\phi$ which is zero. Therefore the coefficients are zero independent of k and this leads to the two conditions (where I have already put $D = 0$)

$$A^2 + B^2 = C^2 \qquad (A5.17)$$

$$\beta A \sin\phi + \beta B \cos\phi - \alpha C \sin\phi = 0. \qquad (A5.18)$$

From equation (A5.17) we may write $A = C\cos\delta$, $B = C\sin\delta$. Equation (A5.18) gives

$$\delta = \sin^{-1}\left(\frac{\alpha}{\beta}\sin\phi\right) - \phi \qquad (A5.19)$$

and using the boundary condition gives the generating functions as

$$\mathbf{P}_k^{\uparrow} = \frac{\sin\left[\sin^{-1}\left(\frac{\alpha}{\beta}\sin\phi\right) + (k-1)\phi\right]}{\sin\left[\sin^{-1}\left(\frac{\alpha}{\beta}\sin\phi\right) + (a-1)\phi\right]} \qquad (A5.20)$$

$$\mathbf{P}_k^{\downarrow} = \frac{1}{\sin\left[\sin^{-1}\left(\frac{\alpha}{\beta}\sin\phi\right) + (a-1)\phi\right]}. \qquad (A5.21)$$

It is easily verified that this leads to the correct probabilities in the limit $\phi \to 0$ and $\alpha \to \beta$.

Appendix 5B: Calculation of Temperature Properties

To generate the temperature distributions shown in the Figures in Chapter 5, a sample of random half-walks was constructed. These start from halfway between the plates (in terms of steps, for a variable step size) and equal numbers of half-walks reach each plate. This allows a much larger sample of full walks to be constructed from pairs of half walks. The temperature at the join is given a value $T_{1/2}$, and the mean and standard deviation of this are easily calculated.

The temperature varies linearly (from either 0 to $T_{1/2}$ or from $T_{1/2}$ to 1) along the half walks. The properties of the temperature distribution at a point are calculated from the distribution of temperatures on the random walks that pass through that point in terms of $T_{1/2}$. The distribution of temperatures $T_{1/2}$ is then included.

For Figure 5.2 a spherical system is modelled by increasing the step length with radius, so that the step length at radius r is a certain fraction of r (0.2 in this case). Two or three dimensional models can be constructed by allowing the walk to be parallel to the plates. The effect of this was found to be negligible.